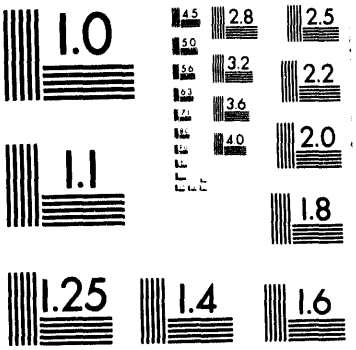
1.0
1.1
1.25
1.4
1.6
1.8
2.0
2.2
2.5
2.8
3.2
3.6
4.0
4.5
5.0
5.6
6.3
7.1

1 of 2

LBL-34884
UC-404

Nuclear Magnetic Relaxation Studies of Semiconductor Nanocrystals and Solids

Joseph Robert Sachleben

Department of Chemistry
University of California

and

Materials Sciences Division
Lawrence Berkeley Laboratory
University of California
Berkeley, California 94720

September 1993

This work was supported by the Director, Office of Energy Research, Office of Basic Energy Sciences, Materials Sciences Division of the U.S. Department of Energy, under Contract No. DE-AC03-76SF00098.

Nuclear Magnetic Relaxation Studies of Semiconductor Nanocrystals and Solids

by

Joseph Robert Sachleben

Abstract

Nuclear Magnetic Relaxation Studies of Semiconductor Nanocrystals and Solids

by

Joseph Robert Sachleben

Doctor of Philosophy in Chemistry

University of California at Berkeley

Professor Alex Pines, Chair

Semiconductor nanocrystals, small biomolecules, and ^{13}C enriched solids have been studied by analyzing the relaxation properties of their nuclear magnetic resonance (NMR) spectra. More specifically, for the first time, details of the structure of the surface of semiconductor nanocrystals was obtained. The surface structure was deduced from high resolution ^{1}H and ^{13}C liquid state spectra of the thiophenol ligands on the surface of the nanocrystals, which were assigned using standard 2-dimensional liquid state techniques. Intensity calibrated ^{1}H NMR spectra were recorded as a function of nanocrystal radius, and the surface coverage by thiophenol was found to be low, varying from 5.6% and 26% as the nanocrystal radius changed from 11.8 to 19.2 Å. The longitudinal and transverse relaxation times of the ^{1}H and ^{13}C resonances of the thiophenol ligands show that the spectra are homogeneously broadened and that the broadening increases as the nanocrystal radius becomes smaller. This suggests that the thiophenol ligands are rotating with respect to the nanocrystal surface and that the correlation time of this motion increases with decreasing radius. The internal motion is estimated to be quite slow with a correlation time greater than 10^{-8} sec^{-1}. The temperature dependence of the ^{1}H transverse relaxation times was anomalous. These relaxation times decreased with increasing temperature. In addition, the surface thiophenol ligands are shown to react to form a dithiophenol when the nanocrystals were simultaneously subjected to O_2 and ultraviolet light.

We present a method for measuring ^{14}N-^{1}H J-couplings in small biomolecules by measuring the rate of scalar relaxation of the second kind. These couplings are related to molecular conformation. By measuring the ^{14}N longitudinal relaxation time and the difference in the ^{1}H transverse and longitudinal relaxation rates, the ^{14}N-^{1}H J-couplings can be determined. The method is demonstrated on pyridine and the small peptide oxytocin. To measure the relaxation times in crowded spectra with overlapping peaks in 1D, we present new selective 2D T_1 and T_2 experiments. The results show that the technique is viable; however, relaxation effects due to chemical shift anisotropy and modulation by strong coupling interfere with the technique.

Finally, we demonstrate the possibility of carbon-carbon cross relaxation in ^{13}C enriched solids. ^{13}C magic angle spinning exchange experiments performed on polycrystalline samples of $^{13}C_2$ Zinc Acetate and $^{13}C_3$ L-Alanine show correlations between the resolved carbon sites in the molecule which grow at a rate proportional to the distance between the carbons. This occurred even though spin diffusion through the protons was quenched by high powder. Normal mechanisms for cross relaxation are inefficient in rigid solids because the fluctuations of the intercarbon vectors have a very low amplitude and a very high frequency on the NMR scale. For this reason, the cross relaxation is explained by a dynamic mixing of the eigenstates caused by the motions of the nearby protons. Additionally, the quenching of normal H cross relaxation leaves open the possibility to observe higher order effects and we have observed the presence of two spin dipolar order between the ^{13}C nuclei, which is explained by a third order perturbation theory.

Table of Contents

Acknowledgments

My years at Berkeley would not have been possible without the support of Professor Alexander Pines. His enthusiasm is contagious and his intelligence and creativity inspiring. It has been an honor to work for him for the past five years.

I also need to thank the members of the Pines' laboratory not only for their companionship over the years but also for the stimulating atmosphere they create. I especially would like to thank Joe Zwanziger, Ulli Werner, Zbigniev Oleniczak, Antoine Llor, Phillip Grandinetti, and Margaret Eastman for taking me under wing and teaching me about NMR. In between our regular runs to get Indian food, E. Wrenn Wooten was crucial to the nanocrystal studies. Lyndon Emsley has been a constant help over the last two years of my graduate life. He arrived at a crucial time in the nanocrystal studies, pushed me towards learning new areas, and, with the help of Marinella and Stefano Caldareli, actually helped me get a social life. Rebecca Taylor is thanked for "bothering" me and for working with me and the human calculator Eyal Barash on the solid-state cadmium project.

This thesis would not have been in its present form without the patient help of Professor Paul Alivisatos. He has always challenged me with new ideas and the hard questions about the nanocrystal data that we have acquired. His graduate students also helped to keep me thinking. In particular, Vicki Colvin is thanked not only for working on the science with me, but for also being a constant companion over the years.

Finally, and most importantly, I must thank my father, bother, and my darling Nicky for their support over all these years.

Chapter I: Introduction: Quantum Mechanics and NMR

Section 1.1: Introduction

Nuclear Magnetic Resonance (NMR) Spectroscopy has successfully addressed numerous chemical problems since its invention five decades ago. These successes have been due to the detailed chemical information the experiment provides and the flexibility of the technique that allows the researcher to develop clever methods of extracting this information. The information provided by the technique ranges from gross structural correlations between the resonance frequency of the nucleus and its position in the molecule under study to detailed structural and motional information about the system. In this thesis, we will present relaxation studies that will provide us with detailed structural and motional data about semiconductor nanocrystals, biomolecules, and ^{13}C enriched solids.

However, in order to understand these relaxation measurements, a knowledge of quantum mechanics is necessary. Especially important is understanding how to simplify the quantum mechanical equations so that intuition is developed and results are quickly obtained. Conversely, it is also important to understand when these simplifications are correctly applied so that one does not obtain incorrect results. This chapter will deal with methods of obtaining approximate solutions to the quantum mechanical problems that describe NMR. To begin this discussion, we must introduce quantum mechanics in terms of the density matrix.

Section 1.2: Quantum Mechanics and the Density Matrix

In quantum mechanics, the state of the system is describable by either a state vector (wavefunction) or a density matrix. The state vector provides information about the system by assuming the existence of a quantum mechanical ensemble of identically prepared systems. I will assume in this thesis that the reader is familiar with quantum mechanics in terms of state vectors. Such a description is convenient when one is dealing with single particles such as a single electron or a single atom, but it becomes burdensome when one needs to deal with a real macroscopic sample. In such a sample, a statistical mechanical ensemble is needed along with the quantum ensemble to describe the system because the macroscopic sample can be thought of made up of an ensemble of quantum systems. The density matrix most naturally describes such a system.

The density matrix is defined as

$$\rho = \sum_i P_i |\Psi_i><\Psi_i|, \qquad \text{(eq. 1.2.1)}$$

where $|\Psi_i>$ is the wavefunction for the i^{th} quantum mechanical system in the sample, P_i is the probability that the i^{th} quantum mechanical system occurs in the sample, and the summation is over the statistical mechanical ensemble that describes the sample. As an example, for a gas at low pressures and high temperatures (an ideal gas), $|\Psi_i>$ refers to the state of the i^{th} atom and P_i is the probability an atom has that state in the gas. All observable properties are related to the density matrix by

$$<Q> = \mathrm{Tr}(\rho Q), \qquad \text{(eq. 1.2.2)}$$

where Tr indicates the trace, and <Q> is the expectation value of the observable operator Q[1].

In two cases it is easy to compute the density matrix of the system under study. The first is the density matrix of a pure state, which means that only one quantum mechanical system occurs in the sample. Then, the density matrix is

$$\rho = |\Psi><\Psi| . \qquad \text{(eq. 1.2.3)}$$

If the wavefunction is written as a linear combination of a complete set of eigenvectors,

$$|\Psi> = \sum_i a_i |\varphi_i>, \qquad \text{(eq. 1.2.4)}$$

the density matrix is,

$$\rho = \sum_i \sum_j a_i b_j |\varphi_i><\varphi_j|$$

$$= \sum_i \sum_j c_{ij} |\varphi_i><\varphi_j|, \qquad \text{(eq. 1.2.5)}$$

where a_i, b_j, and c_{ij} are complex numbers. So if the wavefunction of the system is known, the density matrix can be simply and superfluously found. The diagonal matrix elements of the density matrix, c_{ii}, are referred to as the populations while the off-diagonal matrix elements, c_{ij}, are the coherences. If the $|\varphi_i>$ are eigenvectors of the Hamiltonian, the diagonal elements refer to the populations of the energy levels and the off-diagonal terms provide information about the phase relationship of those members of the system that are in superposition states. In a pure state, this phase relationship is perfect, and the quantum states add without cancellation.

The second easy calculable case is that for a system at equilibrium, where, with the density matrix written in the eigenbasis of the Hamiltonian, we know that the off-

diagonal matrix elements are zero, because at equilibrium there is no phase relationship between the superposition states (the random phase assumption which is a definition of equilibrium[2]). This random phase assumption is equivalent, as we will show later, to saying that at equilibrium the macroscopic state of the system is time independent. The diagonal elements are the populations of the energy levels which are given by the Boltzman distribution. Thus, all the c_{ij} are determined by

$$c_{ij} = \begin{cases} 0 & \text{if } i \neq j \\ e^{-\beta E_i}/Z & \text{if } i = j \end{cases}, \qquad \text{(eq. 1.2.6)}$$

where Z is the partition function, which is given by

$$Z = Tr(e^{-\beta H}). \qquad \text{(eq. 1.2.7)}$$

The density matrix for an equilibrium state is more succinctly written in terms of operators[1,3-5] as

$$\rho = e^{-\beta \mathrm{H}}/Z. \qquad \text{(eq. 1.2.8)}$$

These formulae for the equilibrium density matrix tell us that to find the density matrix we need to diagonalize the Hamiltonian and then determine the exponential operator in equation 1.2.8. In many cases, the Hamiltonian only needs to be approximately diagonalized leading to a good approximation of the equilibrium density matrix.

It is common in high-field NMR to approximate the density matrix by keeping only the largest part of the Hamiltonian. In a large magnetic field, the interaction between the nuclei and the magnetic field dominates all others. This allows us to approximate the

Hamiltonian (note that this is a semiclassical Hamiltonian, because we are only dealing with the spin degrees of freedom), in frequency units, as

$$H = -\omega_o I_z, \qquad \text{(eq. 1.2.9)}$$

where I_z is the operator for the z component of the nuclear angular momentum, and ω_o is the Larmor frequency, which is given by

$$\omega_o = \gamma B_o. \qquad \text{(eq. 1.2.10)}$$

In this last equation, γ is the gyromagnetic ratio of the nucleus, and B_o is the external magnetic field strength. We can substitute equation 1.2.9 into equation 1.2.8 in order to approximate the density matrix as

$$\rho = e^{\beta\omega_o I_z}/Z. \qquad \text{(eq. 1.2.10)}$$

However, under normal experimental conditions $1/\beta$=kT>>ω_o (the high temperature approximation), which allows us to approximate the density matrix by expanding the exponential to first order as

$$\rho \approx (1 + \beta\omega_o I_z)/Z. \qquad \text{(eq. 1.2.11)}$$

This approximation also allows us to evaluate the partition function, Z, in equation 1.2.11 by recognizing that every diagonal element of the exponential operator is almost 1, which makes the partition function equal to the number of nuclear states,

$$Z \approx 2I + 1. \qquad \text{(eq. 1.2.12)}$$

Combining equations 1.2.11 and 1.2.12 and neglecting the physically unimportant term proportional to the identity operator, we get

$$\rho \approx \frac{\omega_o}{kT(2I+1)} I_z \,. \qquad \text{(eq. 1.2.13)}$$

Thus, a sample of spins at equilibrium in a large magnetic field has a density matrix proportional to the z component of nuclear angular momentum, which is equivalent to saying that at equilibrium, the spins tend to align with the large external magnetic field., as we would expect[3].

Now that we can find the density matrix in a few simple situations, we need to discover how the density matrix evolves with time. The time-dependence of the density matrix is determined by the Liouville-von Neumann equation,

$$\frac{\partial \rho}{\partial t} = -i[H,\rho] \,. \qquad \text{(eq. 1.2.14)}$$

This equation can be formally integrated to give ρ as a function of time[1,3,5,6];

$$\rho(t) = e^{-iHt}\rho(0)e^{+iHt} \,. \qquad \text{(eq. 1.2.15)}$$

In order to produce equation 1.2.15, I had to assume that the Hamiltonian is not a function of time. In general, this assumption is reasonable, because I can always make the Hamiltonian time-independent. Practically, however, it is many times inconvenient to consider a time independent Hamiltonian, and it then becomes necessary to find a solution to equation 1.2.14. Many times, equation 1.2.14 is easier to deal with by making the rotating frame transformation. Assume

$$H(t) = H_0 + H_1(t), \qquad \text{(eq. 1.2.16)}$$

where H_0 is the Zeeman interaction and $H_1(t)$ is a smaller internal interaction, for example the dipole-dipole interaction, chemical shift interaction, quadrupole interaction, ect. If we make the transformation $\rho^* = e^{iH_0t}\rho e^{-iH_0t}$ and $H_1^* = e^{iH_0t}H_1 e^{-iH_0t}$, equation 1.2.14 becomes

$$\frac{\partial \rho^*}{\partial t} = -i[H_1^*, \rho^*]. \qquad \text{(eq. 1.2.17)}$$

This transformation will allow us to concentrate on the weaker internal interactions without the interference of the fast Zeeman oscillations. At short times, this equation can be integrated by successive approximations[7] as follows:

$$\int_0^t \frac{\partial \rho^*(t')}{\partial t'} dt' = -i\int_0^t [H_1^*(t'), \rho^*(t')]dt' \qquad \text{(eq. 1.2.18)}$$

$$\rho^*(t) = \rho^*(0) - i\int_0^t [H_1^*(t'), \rho^*(t')]dt' \qquad \text{(eq. 1.2.19)}$$

We now assume that the time change is small enough that $\rho^*(t) \approx \rho^*(t')$, which allows us substitute the right side of equation 1.2.17 into itself for $\rho^*(t')$. Iterating in such a fashion twice, and only keeping terms up to second order, we find that

$$\rho^*(t) = \rho^*(0) - i\int_0^t [H_1^*(t'), \rho^*(0)]dt' - \int_0^t \int_0^{t'} [H_1^*(t'), [H_1^*(t''), \rho^*(0)]]dt''dt' . \qquad \text{(eq. 1.2.20)}$$

As we have just shown, short time approximations to the Liouville-van Neumann equation can be found. Unfortunately, long time solutions are much more difficult to

produce. The normal solution to this problem in the NMR community is to make an effective, time-independent Hamiltonian that correctly describes the long time behavior of the density matrix. Once we find this time-independent Hamiltonian, we simply need to evaluate equation 1.2.15. Thus, the question of how to calculate the long time behavior of the density matrix is effectively the same as the question of how to correctly calculate an effective Hamiltonian, and when to appropriately apply this Hamiltonian.

Section 1.3: Average Hamiltonian Theory

Since its introduction to the NMR community in 1968[8,9], Average Hamiltonian Theory has been a popular method of calculating effective Hamiltonia. It has been used to describe the effects of multiple pulse sequences, composite pulses, spins experiencing constant wave (cw) radio-frequency (rf) irradiation, and many other important problems. The basic idea in average Hamiltonian theory is to replace the true propagator

$$U = Te^{-iHt}, \qquad \text{(eq. 1.3.1)}$$

where T is the Dyson time ordering operator, with an effective propagator

$$U_{eff} = e^{-i\overline{H}t_c} \qquad \text{(eq. 1.3.2)}$$

which is governed by the average Hamiltonian, $\overline{H}$, over the period t_c. Average Hamiltonian Theory is a method for calculating this average Hamiltonian. The average Hamiltonian will depend on the initial and final times, unless the original Hamiltonian is periodic and observation is performed stroboscopically with the period of the Hamiltonian.

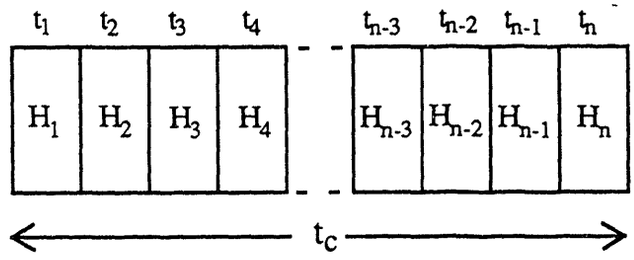

FIG. 1.3.1: Above is a graphical representation of a Hamiltonian that changes discretely n times. H_k is the k^{th} Hamiltonian which lasts for a time t_k. The total time which this time-dependent Hamiltonian acts on the system is t_c. In the limit that the t_ks become infinitesimal, the Hamiltonian become continuously time-dependent for the time t_c.

There are two limiting cases for the time dependence of the Hamiltonian: discrete and continuous time dependence. We will begin by finding the average Hamiltonian for a Hamiltonian that has a discrete time dependence, which means that the Hamiltonian stays constant for a time period, t_i, at which time it suddenly changes to a new Hamiltonian (see figure 1.3.1). In the case where the Hamiltonian discretely changes n times, the propagator is a product of propagators for each time period,

$$U = U_n U_{n-1} \ldots U_2 U_1$$

$$= e^{-iH_n t_n} e^{-iH_{n-1} t_{n-1}} \ldots e^{-iH_2 t_2} e^{-iH_1 t_1}, \qquad \text{(eq. 1.3.3)}$$

where U_i , H_i, and t_i and refer to the propagator, the Hamiltonian, and the length of duration of the i^{th} period. This product of exponential operators can be expressed as a single operator by use of the Baker-Campbell-Hausdorff relation,

$$e^A e^B = \exp\{A + B + \tfrac{1}{2}[B,A] + \tfrac{1}{12}([B,[B,A]] + [A,[A,B]] + \ldots\}, \qquad \text{(eq. 1.3.4)}$$

to find that the average Hamiltonian that guides the evolution over the entire period,

$$t_c = t_1 + t_2 + \ldots + t_{n-1} + t_n. \qquad \text{(eq. 1.3.5)}$$

This average Hamiltonian is

$$\overline{H} = \overline{H}^{(0)} + \overline{H}^{(1)} + \overline{H}^{(2)} + \ldots , \qquad \text{(eq. 1.3.6)}$$

where

$$\overline{H}^{(0)} = \tfrac{1}{t_c}\{H_1 t_1 + H_2 t_2 + \ldots + H_{n-1} t_{n-1} + H_n t_n\}, \qquad \text{(eq. 1.3.7)}$$

$$\overline{H}^{(1)} = -\tfrac{i}{2t_c}\{[H_2 t_2, H_1 t_1] + \text{all other commutators}\}, \qquad \text{(eq. 1.3.8)}$$

and

$$\overline{H}^{(2)} = -\tfrac{1}{6t_c}\{[H_3 t_3, [H_2 t_2, H_1 t_1]] + [H_1 t_1, [H_2 t_2, H_3 t_3]]$$

$$+ \tfrac{1}{2}[H_2 t_2, [H_2 t_2, H_1 t_1]] + \tfrac{1}{2}[H_1 t_1, [H_1 t_1, H_2 t_2]] + \ldots\}. \qquad \text{(eq. 1.3.9)}$$

This series can be truncated as long as $\|H^2\|^{\frac{1}{2}} t_c < 1$, in which case the higher order terms clearly go to zero.

This convergence criterion would initially seem to indicate that Average Hamiltonian Theory is a short time approximation, but it is also applicable to periodic Hamiltonians where the cycle time and the strength of the perturbing Hamiltonian is small enough that $\|H^2\|^{\frac{1}{2}} t_c < 1$. A periodic Hamiltonian is one that returns to itself every t_c, or, mathematically,

$$H(t) = H(t + nt_c). \qquad \text{(eq. 1.3.10)}$$

Under these conditions, the average Hamiltonian over a cycle can be calculated. This Hamiltonian dictates the evolution of the density matrix over the same cycle time, thus implying that measurement of any observable must be performed stroboscopically and synchronously with this time. This rigid requirement of stroboscopic observation has led to some misuses of Average Hamiltonian Theory, as we will present later.

If the Hamiltonian is cyclic and continuously time dependent, Average Hamiltonian Theory is still applicable, but we substitute the continuous analogs of equations 1.2.7-1.2.9 into equation 1.2.6. These new definitions of $\overline{H}^{(0)}$ through $\overline{H}^{(2)}$ are

$$\overline{H}^{(0)} = \frac{1}{t_c}\int_0^{t_c} H(t_1)dt_1, \qquad \text{(eq. 1.3.11)}$$

$$\overline{H}^{(1)} = -\frac{i}{2t_c}\int_0^{t_c}\int_0^{t_2} [H(t_2),H(t_1)]dt_1dt_2, \qquad \text{(eq. 1.3.12)}$$

and

$$\overline{H}^{(2)} = -\frac{1}{6t_c}\int_0^{t_c}\int_0^{t_3}\int_0^{t_2} \{[H(t_3),[H(t_2),H(t_1)]]$$

$$+[H(t_1),[H(t_2),H(t_3)]]\}dt_1dt_2dt_3. \qquad \text{(eq. 1.3.13)}$$

These equations are found by making all the times in equations 1.3.7-1.3.9 small so that the sums are replaced by integrals.

As an example of the use of Average Hamiltonian Theory, we will calculate the average Hamiltonian to first order for a single quadrupolar spin (I>1/2) in a large magnetic field. In this calculation, we will assume familiarity with spherical tensors[1,10,11]. The total Hamiltonian for this system, H, is

$$H = H_Z + H_Q, \qquad \text{(eq. 1.3.15)}$$

where

$$H_Z = -\omega_0 I_z \qquad \text{(eq. 1.3.16)}$$

and

$$H_Q = C^Q \sum_{m=-2}^{2} (-1)^m R^Q_{2,-m} T^Q_{2,m}. \qquad \text{(eq. 1.3.17)}$$

Transforming equation 1.2.17 into the Zeeman interaction representation by

$$\tilde{H}_Q = U H_Q U^{-1}, \qquad \text{(eq. 1.3.18)}$$

where

$$U = e^{i\omega_0 t I_z}, \qquad \text{(eq. 1.3.19)}$$

removes the static Zeeman interaction and makes the quadrupole interaction time-dependent for a density matrix in the same interaction representation. This can be proven by substitution into the Liouville-von Neumann Equation (equation 1.2.14). In this interaction representation, our Hamiltonian is now time-dependent, and we can apply average Hamiltonian Theory by substituting $\tilde{H}_Q$ into equations 1.3.11-1.3.12. First, we need to explicitly write down $\tilde{H}_Q$:

$$\tilde{H}_Q = C^Q \sum_{m=-2}^{2} (-1)^m R^Q_{2,-m} e^{i\omega_0 t I_z} T^Q_{2,m} e^{-i\omega_0 t I_z}$$

$$= C^{Q} \sum_{m=-2}^{2} (-1)^{m} R^{Q}_{2,-m} T^{Q}_{2,m} e^{-im\omega_0 t}, \qquad \text{(eq. 1.3.20)}$$

where we have used the identity[12]

$$e^{A} B e^{-A} = B + [A,B] + \tfrac{1}{2!}[A,[A,B]] + \tfrac{1}{3!}[A,[A,[A,B]]] + \ldots \qquad \text{(eq. 1.3.21)}$$

and the commutation relation between I_Z and the spherical tensors[1,10,11],

$$[I_Z, T_{l,m}] = m T_{l,m}. \qquad \text{(eq. 1.3.22)}$$

Notice that we have Fourier analyzed the time dependence of the quadrupolar Hamiltonian by using spherical tensors. Substituting equation 1.3.20 into 1.3.11, and using the orthogonality relationship between Fourier components[13],

$$\int_0^{2\pi/\omega_0} e^{in\omega_0 t} e^{im\omega_0 t} dt = \begin{cases} \frac{2\pi}{\omega_0} \text{ if } n = -m \\ 0 \text{ otherwise} \end{cases}, \qquad \text{(eq. 1.3.23)}$$

we find the zeroth order average hamiltonian to be

$$\overline{H}^{(0)} = C^{Q} R^{Q}_{2,0} T^{Q}_{2,0}. \qquad \text{(eq. 1.3.24)}$$

Next, we need to find the first order average Hamiltonian by evaluating equation 1.3.12 after the substitution of 1.3.20,

$$\overline{H}^{(1)} = (\tfrac{C^{Q}}{2t_c})^2 \sum_{n=-2}^{2} \sum_{m=-2}^{2} (-1)^{m+n} R^{Q}_{2,-n} R^{Q}_{2,-m} [T^{Q}_{2,n}, T^{Q}_{2,m}] \int_0^{t_c} \int_0^{t_2} e^{-in\omega_0 t_2} e^{-im\omega_0 t_1} dt_1 dt_2. \qquad \text{(eq. 1.3.25)}$$

This can be done by first carrying out the integrations, to find that

$$\int_0^{t_c}\int_0^{t_2} e^{-in\omega_0 t_2} e^{-im\omega_0 t_1} dt_1 dt_2 = \frac{t_c}{\omega_0}\{\pi\delta_{m,0}\delta_{n,0} + \frac{i}{n}(\delta_{m,-n} - \delta_{m,0}) + \frac{i}{m}\delta_{n,0}\}. \quad \text{(eq. 1.3.26)}$$

We then substitute this into equation 1.3.25, to find

$$\overline{H}^{(1)} = -i\frac{{C_Q}^2}{2\omega_0}\{R^Q_{2,0}R^Q_{2,0}[T^Q_{2,0},T^Q_{2,0}]$$

$$+i\sum_{\substack{m=-2\\ m\neq 0}}^{2}\frac{1}{m}R^Q_{2,m}R^Q_{2,-m}[T^Q_{2,m},T^Q_{2,-m}] + 2i\sum_{\substack{m=-2\\ m\neq 0}}^{2}\frac{(-1)^m}{m}R^Q_{2,0}R^Q_{2,-m}[T^Q_{2,0},T^Q_{2,m}]\}. \quad \text{(eq. 1.3.27)}$$

The commutators are evaluated by expanding the product of spherical tensors[14]:

$$u_{j,m}v_{j',m'} = \sum_{J=|j-j'|}^{J=j+j'}\frac{1}{N_J} < j,j',m,m'|J,M > U_{J,M}, \quad \text{(eq. 1.3.28)}$$

where N_J is a normalization constant, $< j,j',m,m'|J,M >$ is a Clebsch-Gordan coefficient, and $u_{J,M}$, $v_{J,M}$, and $U_{J,M}$ are spherical tensors. This expansion of the product of spherical tensors then implies that the commutators in equation 1.3.27 can be written as

$$[T_{2,m},T_{2,m'}] = \sum_{J=0}^{J=4}\frac{1}{N_J}\{< 2,2,m,m'|J,M > - < 2,2,m',m|J,M >\}T_{J,M} \quad \text{(eq. 1.3.29)}$$

The symmetry relation of the Clebsch-Gordan coefficients[10],

$$< j,j',m,m'|J,M >= (-1)^{j+j'-J} < j',j,m',m|J,M >, \quad \text{(eq. 1.3.30)}$$

immediately implies that the J=0,2,and 4 do not occur in the expansion of the commutator, and equation 1.3.29 becomes

$$[T_{2,m},T_{2,m'}]=\tfrac{2}{N_3}<2,2,m,m'|3,M>T_{3,M}-\tfrac{2}{N_1}<2,2,m,m'|1,M>T_{1,M}. \qquad \text{(eq. 1.3.31)}$$

In table 1.3.1, we tabulate the commutators needed to evaluate equation 1.3.27 and we after using these commutators, we find that the first order correction to the average Hamiltonian is

$$\overline{H}^{(1)}=\tfrac{C_Q^2}{2\omega_0}\{\sqrt{\tfrac{2}{5}}[\tfrac{1}{N_3}(4R^Q_{2,1}R^Q_{2,-1}+R^Q_{2,2}R^Q_{2,-2})T^Q_{3,0}-\tfrac{2}{N_1}(R^Q_{2,1}R^Q_{2,-1}-R^Q_{2,2}R^Q_{2,-2})T^Q_{1,0}]$$

$$-\tfrac{\sqrt{2}}{N_3}[R^Q_{2,0}R^Q_{2,2}T^Q_{3,-2}+R^Q_{2,0}R^Q_{2,-2}T^Q_{3,2}]$$

$$-\tfrac{4}{N_3}\sqrt{\tfrac{1}{5}}[R^Q_{2,0}R^Q_{2,1}T^Q_{3,-1}+R^Q_{2,0}R^Q_{2,-1}T^Q_{3,1}]$$

$$-\tfrac{2}{N_1}\sqrt{\tfrac{6}{5}}[R^Q_{2,0}R^Q_{2,1}T^Q_{1,-1}+R^Q_{2,0}R^Q_{2,-1}T^Q_{1,1}]\}. \quad \text{(eq. 1.3.32)}$$

Now that we have found the Average Hamiltonian, we can calculate the time-dependence

m	X	$[T_{2,m},X]$
0	$T_{2,0}$	0
0	$T_{2,\pm1}$	$\mp\tfrac{2}{N_3}\sqrt{\tfrac{1}{5}}T_{3,\pm1}\pm\tfrac{1}{N_1}\sqrt{\tfrac{6}{5}}T_{1,\pm1}$
0	$T_{2,\pm2}$	$\mp\tfrac{\sqrt{2}}{N_3}T_{3,\pm2}$
1	$T_{2,-1}$	$\tfrac{2}{N_3}\sqrt{\tfrac{2}{5}}T_{3,0}-\tfrac{1}{N_1}\sqrt{\tfrac{2}{5}}T_{1,0}$
2	$T_{2,-2}$	$\tfrac{1}{N_3}\sqrt{\tfrac{2}{5}}T_{3,0}+\tfrac{2}{N_1}\sqrt{\tfrac{2}{5}}T_{1,0}$

Table 1.3.1: Commutators of second rank irreducible tensors.

of the density matrix of a quadrupolar nucleus. Notice, however, that Average Hamiltonian in this case is not so simple to use because it is not diagonal in the Zeeman basis. In the following sections, we will deal with equation 1.3.32 and its consequences.

Section 1.4: Problems with Average Hamiltonian Theory

In the previous section, we calculated the average Hamiltonian to first order for a quadrupolar nucleus in a large magnetic field. We found that the first order correction contained terms that are off-diagonal in the Zeeman basis. Unfortunately, these off-diagonal terms imply that techniques like Double Rotation(DOR) and Dynamic Angle Spinning(DAS), which narrows the solid-state quadrupolar resonance of odd 1/2 integer quadrupolar nuclei, should not work[15-17]. The common explanation for this is that equation 1.3.32 must be reaverage with respect to the large zeroth order average Hamiltonian to produce the correct average Hamiltonian. When this is done, all the off-diagonal terms are lost, and equation 1.3.32 becomes

$$\overline{H}^{(1)} = \frac{C_Q^2}{2\omega_0}\{\sqrt{\frac{2}{5}}[\frac{1}{N_3}(4R^Q_{2,1}R^Q_{2,-1} + R^Q_{2,2}R^Q_{2,-2})T^Q_{3,0} - \frac{2}{N_1}(R^Q_{2,1}R^Q_{2,-1} - R^Q_{2,2}R^Q_{2,-2})T^Q_{1,0}]. \quad \text{(eq. 1.4.1)}$$

Even though this last step is nonintuitive, it gives the correct equation for the first order average Hamiltonian of a quadrupolar spin in a large magnetic field.

However, this extra needed step gives rise to two predictions in a gedanken experiment. Assume that the sample of quadrupolar nuclei rotate fast enough about the magic angle to average out the zeroth order term. In this case, two predictions are made depending on whether the off-diagonal terms are kept of discarded. At variance with this ambiguity, static perturbation theory only predicts the result without the off-diagonal terms.[18] We have performed a set of simulations for the NMR transition of a single-crystal sample, containing equivalent uncoupled quadrupolar nuclei of spin 3/2, and

spinning about the magic angle at various rotation rates.[19] The spectra in figure 1.4.1 were calculated using three different methods: a full diagonalization procedure (referred to as "exact"), using the average hamiltonian result presented in the previous section, and using the static perturbation result, which is the same as the average Hamiltonian result with the off-diagonal terms dropped (a sum of equations 1.3.24 and 1.4.1). The results clearly show the failure of Average Hamiltonian Theory to provide even an approximate description of the system when the spinning speed becomes comparable to the

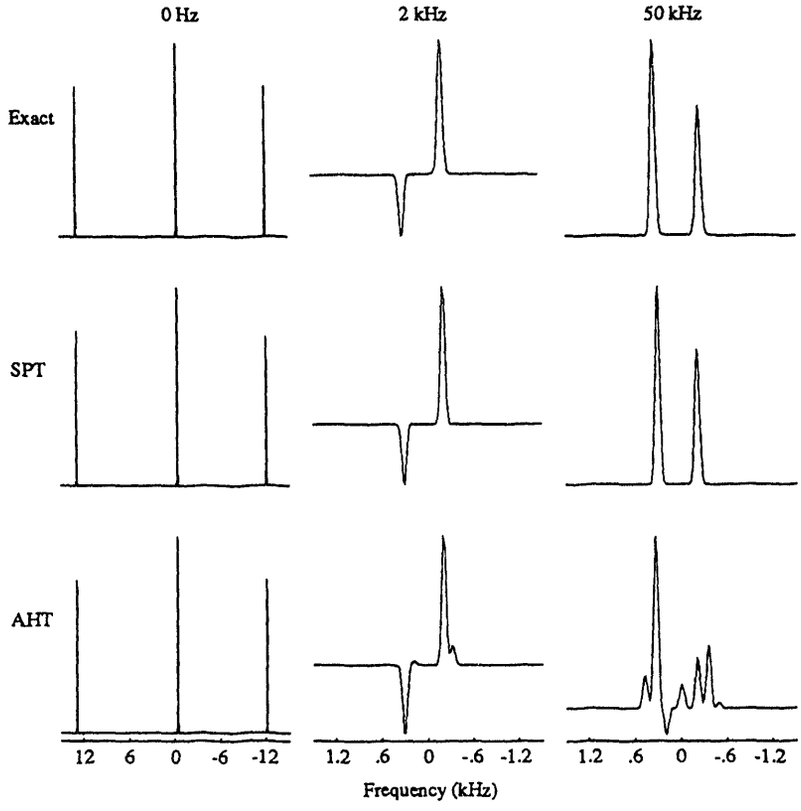

FIG. 1.4.1: Exact, Static Perturbation Theory, and Average Hamiltonian Theory simulations of the NMR transitions of a single-crystal sample, containing equivalent uncoupled quadrupolar nuclei of spin 3/2, and spinning around the magic angle at three different speeds. The spinning speeds (ν_R=0, 2, and 50 kHz), are selected to fall in the ranges 0-ν^2_Q/ν_Z, ν^2_Q/ν_Z-ν_Q, and ν_Q-ν_Z, showing three different behaviors of the Average Hamiltonian Theory result. The Static Perturbation Theory simulations were performed in the laboratory frame using a nontilted diagonal Hamiltonian containing the Zeeman interaction and the quadrupolar interaction truncated to second order. The simulation was performed by Philip Grandinetti.

quadrupolar coupling, while Static Perturbation Theory is in good agreement throughout the range of experimental parameters.

In the next few sections of this thesis, we will give a general and coherent framework for treating the effects of higher-order terms in perturbation expansions of common problems that arise in NMR. Although this may be done by dynamic methods (i.e., by going to the rotating frame and using Average Hamiltonian Theory), it is simpler to use static diagonalization methods, since the Hamiltonian is time independent. The usual perturbation expansions for the diagonalization are formulated in terms of matrix elements.[1] We will reformulate these in terms of operators decomposed into irreducible tensors. Two different methods, Static Perturbation Theory and Van Vleck transformation, will be given. Two methods are introduced, because Static Perturbation Theory is useful for systems with a finite number of energy levels and the Van Vleck transformation is adapted to highly degenerate (e.g., dipolar broadened) systems. With these two computational techniques, we will generate effective Hamiltonians and interaction frames that are suitable for analyzing averaging experiments. We will also discuss the proper conditions under which Average Hamiltonian Theory can be applied and the difficulties involved in extending this approach to include sample motion.

Section 1.5: Static Perturbation Theory in Terms of Irreducible Tensors

In its usual formulation, Static Perturbation Theory[1] provides an expansion for the eigenvalues and eigenstates of a perturbed operator (which in our case will be the spin Hamiltonian possibly including the radio frequency magnetic field). The results to second order in the nondegenerate case are summarized by the following formulae:

$$H = H^{(0)} + H^{(1)}, \qquad \text{(eq. 1.5.1)}$$

$$H|\nu_j\rangle = E_j|\nu_j\rangle, \qquad H^{(0)}|j\rangle = E_j^{(0)}|j\rangle, \tag{eq. 1.5.2}$$

$$E_j = E_j^{(0)} + E_j^{(1)} + E_j^{(2)}+\ldots, \qquad |\nu_j\rangle = |j\rangle + |\nu_j^{(1)}\rangle + \ldots, \tag{eq. 1.5.3}$$

$$E_j^{(1)} = \langle j|H^{(1)}|j\rangle, \tag{eq. 1.5.4}$$

$$E_j^{(2)} = \sum_{k\neq j} \frac{\langle j|H^{(1)}|k\rangle\langle k|H^{(1)}|j\rangle}{E_j^{(0)} - E_k^{(0)}}, \tag{eq. 1.5.5}$$

$$|\nu_j^{(1)}\rangle = \sum_{k\neq j} \frac{\langle k|H^{(1)}|j\rangle}{E_j^{(0)} - E_k^{(0)}}|k\rangle. \tag{eq. 1.5.6}$$

These formulae for the matrix elements can be rewritten in terms of operators as follows:

$$H = VDV^{-1}, \tag{eq. 1.5.7}$$

$$D = H^{(0)} + D^{(1)} + D^{(2)}+\ldots, \qquad V = 1 + V^{(1)}+\ldots, \tag{eq. 1.5.8}$$

$$D^{(1)} = \sum_j |j\rangle E_j^{(1)} \langle j| \tag{eq. 1.5.9}$$

$$D^{(2)} = \sum_j |j\rangle E_j^{(2)} \langle j|, \qquad V^{(1)} = \sum_j |\nu_j^{(1)}\rangle\langle j|, \tag{eq. 1.5.10}$$

where D and $D^{(n)}$ are diagonal operators and V is a unitary transformation. These equations give the operators in terms of matrix elements and, in general, there is no convenient way of simplifying them. However, in the case of NMR, the Zeeman interaction $H^{(0)}$ is a linear combination of I_z angular momentum operators, and $H^{(1)}$ is the superposition of the various local interactions which have simple expressions in irreducible tensor form. The matrix element $\langle k|H^{(1)}|j\rangle$ in equations 1.5.1 to 1.5.6 can

be simplified by using the Wigner-Eckart Theorem[1,10,11] and the selection rules that it implies to find pure irreducible tensor expansions for the D and V matrices.

We will demonstrate this procedure with the case of a quadrupolar nucleus in a large magnetic field, the same system with which we demonstrated the Average Hamiltonian Theory calculation. Again we have

$$H^{(0)} = -\omega_0 I_z \qquad \text{(eq. 1.5.11)}$$

and

$$H^{(1)} = C^{Q} \sum_{m=-2}^{2} (-1)^m R^{Q}_{2,-m} T^{Q}_{2,m}. \qquad \text{(eq. 1.5.12)}$$

To find the first order correction to the effective Hamiltonian, we need to substitute equation 1.5.12 into 1.5.4 and find

$$E_j^{(1)} = C_Q (-1)^m R^{Q}_{2,-m} < j|T^{Q}_{2,m}|j >. \qquad \text{(eq. 1.5.13)}$$

The Wigner-Eckart Theorem implies the general selection rule for irreducible tensors,

$$< k|T_{2,m}|j >= \delta_{k,j+m} < j+m|T_{2,m}|j >, \qquad \text{(eq. 1.5.14)}$$

which immediately implies that only the m=0 irreducible tensor contributes to this term. Placing the $E_j^{(1)}$ into equation 1.5.10, we find that

$$D^{(1)} = C_Q R^{Q}_{2,0} T^{Q}_{2,0}, \qquad \text{(eq. 1.5.15)}$$

as we had found with Average Hamiltonian Theory. Next we find $D^{(2)}$ by substitution into equation 1.5.5 which will ultimately be used in equation 1.5.10, to find

$$E_j^{(2)} = \frac{c_Q^2}{\omega_0} \sum_{m,m'} (-1)^{m+m'} R_{2,-m}^Q R_{2,-m'}^Q \sum_{j \neq k} \frac{< j|T_{2,m}^Q|k >< k|T_{2,m'}^Q|j >}{k-j}. \qquad \text{(eq. 1.5.16)}$$

The selection rule (equation 1.5.14) restricts the summation over k in equation 1.5.16 to those terms where k=j+m' and k=j-m. This restriction then implies that the sum over m and m' is restricted to m+m'=0 giving

$$E_j^{(2)} = -\frac{c_Q^2}{\omega_0} \sum_{m \neq 0} \frac{R_{2,-m}^Q R_{2,m}^Q}{m} < j|T_{2,m}^Q|j-m >< j-m|T_{2,-m}^Q|j >. \qquad \text{(eq. 1.5.17)}$$

This equation can be further simplified by using a rearrangement of the closure relationship,

$$|j-m >< j-m| = 1 - \sum_{k \neq j-m} |k >< k|, \qquad \text{(eq. 1.5.18)}$$

to find

$$D^{(2)} = -\frac{c_Q^2}{\omega_0} \sum_{m \neq 0} \frac{R_{2,-m}^Q R_{2,m}^Q T_{2,m}^Q T_{2,-m}^Q}{m}, \qquad \text{(eq. 1.5.19)}$$

which we can write in terms of commutators as

$$D^{(2)} = \frac{c_Q^2}{\omega_0} \sum_{m>0} \frac{R_{2,m}^Q R_{2,-m}^Q [T_{2,-m}^Q, T_{2,m}^Q]}{m}. \qquad \text{(eq. 1.5.20)}$$

If commutators are replaced by their values in table 1.3.1, we find that this equation is equivalent to that found in equation 1.4.1. Thus, by using static perturbation theory, we naturally arrive at the correct form for the Hamiltonian correct to second order without

the confusing and wrong ideas of a second averaging with respect to the first order interaction.

Finally, we will calculate the first order tilting matrix, $V^{(1)}$, for this example. We substitute equation 1.5.12 into 1.5.6 and use both the selection rule and the rearranged closure relation to find

$$|v_j^{(1)}\rangle = -\frac{c_Q}{\omega_0}\sum_{m\neq 0}(-1)^m R^Q_{2,-m}T^Q_{2,m}|j\rangle. \qquad \text{(eq. 1.5.21)}$$

Thus the tilting matrix becomes

$$V^{(1)} = -\frac{c_Q}{\omega_0}\sum_{m\neq 0}(-1)^m R^Q_{2,-m}T^Q_{2,m}. \qquad \text{(eq. 1.5.22)}$$

In this section, we have shown how to correctly calculate effective Hamiltonians up to second order for non-degenerate systems. This Static Perturbation method can be used for degenerate systems, as long as the number of energy levels remains small. However, for highly degenerate systems, this technique is intractable and alternate methods must be used. We present a method based on the Van Vleck transformation[20] and apply it to the case of homogeneous dipolar broadening in a solid[19].

Section 1.6: Van Vleck Transformation in Terms of Irreducible Tensor Operators

The Van Vleck transformation, which was first applied by Van Vleck to molecular spectroscopy calculations,[20] is a perturbative method used to block diagonalize an operator having groups of degenerate eigenvalues. Block diagonalization means that no off-diagonal elements connect states of different unperturbed eigenvalues. However,

no restrictions are set inside each eigenspace, which may be highly degenerate. In an operator formalism this is defined by

$$H = H^{(0)} + H^{(1)} = WDW^{-1}, \qquad \text{(eq. 1.6.1)}$$

$$[H^{(0)}, D] = 0, \qquad \text{(eq. 1.6.2)}$$

$$WW^{-1} = 1, \qquad \text{(eq. 1.6.3)}$$

where here we denote the tilting matrix by W to indicate that it does not completely diagonalize the Hamiltonian. As in Static Perturbation Theory, the perturbation expansion can be written in operator form. The expansion of D is identical to equation 1.5. 9, and it is convenient to expand W as

$$W = e^{iS^{(1)}} e^{iS^{(2)}} e^{iS^{(3)}} \ldots, \qquad \text{(eq. 1.6.4)}$$

where the $S^{(n)}$ are Hermitian operators whose magnitudes decrease as $(|H^{(1)}|/|H^{(0)}|)^n$. This expansion is at variance with previous treatments,[20,21] but it simplifies later calculations. Keeping terms up to the second order, equation 1.6.1 is expanded as

$$H^{(0)} + D^{(1)} + D^{(2)} + \ldots$$

$$= \{1 - iS^{(2)} + \ldots\}[1 - iS^{(1)} + (iS^{(1)})^2 / 2 \ldots]$$

$$\times (H^{(0)} + H^{(1)})[1 + iS^{(1)} + (iS^{(1)})^2 / 2 \ldots]$$

$$\times \{1 + iS^{(2)} + \ldots\}, \qquad \text{(eq. 1.6.5)}$$

which upon collecting terms of the same order becomes

$$D^{(1)} = H^{(1)} + [H^{(0)}, iS^{(1)}], \qquad \text{(eq. 1.6.6)}$$

$$D^{(2)} = [H^{(1)}, iS^{(1)}] + \tfrac{1}{2}[[H^{(0)}, iS^{(1)}], iS^{(1)}] + [H^{(0)}, iS^{(2)}] \qquad \text{(eq. 1.6.7)}$$

These operator equations do not define the $D^{(n)}$ and $S^{(n)}$ in a unique way. Aside from the trivial case of adding $H^{(0)}$ to $S^{(1)}$, which is equivalent to multiplication of the eigenstates by a phase factor, another operator that commutes with $H^{(0)}$ may be added to $S^{(1)}$ to generate another solution. There is no easy way to solve equations 1.6.6 and 1.6.7 in general. Van Vleck gave the initial solution for the $D^{(n)}$ and $S^{(n)}$ terms of matrix elements, from which it is eventually possible to yield the expansions for D and W in terms of irreducible tensors.[20] However, in some special cases, it is possible to directly generate an irreducible tensor solution to equations 1.6.1 to 1.6.3.

For the case of homogeneous dipolar couplings, the Hamiltonian is divided as

$$H^{(0)} = H_Z = -\omega_0 \sum_i I_Z^i = -\omega_0 I_Z, \qquad \text{(eq. 1.6.8)}$$

$$H^{(1)} = H_D = \sum_{i<j} H_D^{(ij)}$$

$$= \sum_{i<j} C_D^{(ij)} \sum_m (-1)^m R_{2,-m}^{(ij)} T_{2,m}^{(ij)} = \sum_m H_m, \qquad \text{(eq. 1.6.9)}$$

where i and j label the spin sites, and the $R_{2,-m}^{(ij)}$ and $T_{2,m}^{(ij)}$ are the usual lattice and spin parts of the dipolar coupling. The decomposition of H_D into H_m,, which was introduced by Jeener,[22] is equivalent to the usual dipolar alphabet formalism,[7] and can also be used

to represent the quadrupolar interaction treated in sections 1.3 and 1.5 of this thesis. The H_m have two useful properties, which are the keys to solving equations 1.6.6 and 1.6.7 in terms of irreducible tensors:

$$[I_Z, H_m] = mH_m \qquad \text{(eq. 1.6.10)}$$

and

$$[I_Z, \prod_n H_{m_n}] = (\sum_n m_n)(\prod_n H_{m_n}). \qquad \text{(eq. 1.6.11)}$$

If we set $H^{(1)} = H_D = \sum_m H_m$ in equation 1.6.6, we see that the expression for $D^{(1)}$ has nonsecular contributions (m≠0) coming from $H^{(1)}$. Since $D^{(1)}$ commutes with $H^{(0)}$, as must all the $D^{(n)}$ by definition (equation 1.6.2), the commutator, $[H^{(0)}, iS^{(1)}]$, must cancel the nonsecular terms. Using this constraint, equation 1.6.8 and 1.6.10 can be combined to obtain a simple solution for $S^{(1)}$:

$$S^{(1)} = -\frac{i}{\omega_0} \sum_{m \neq 0} \frac{H_m}{m}, \qquad \text{(eq. 1.6.12)}$$

and thus,

$$D^{(1)} = H_0 \qquad \text{(eq. 1.6.13)}$$

which is the known first order correction. The solution for higher orders follows the same general procedure: the lower-order terms are inserted, the secular parts are assigned to $D^{(n)}$, and the $S^{(n)}$ is tailored to cancel the nonsecular parts by using equation 1.6.11 in the commutator $[H^{(0)}, iS^{(n)}]$. For instance, to find the second order expressions from equation 1.6.7, we first introduce $S^{(1)}$, given by equation 1.6.12, into the first two terms:

$$[H^{(1)},iS^{(1)}]+\tfrac{1}{2}[[H^{(0)},iS^{(1)}],iS^{(1)}]$$

$$=\tfrac{1}{2\omega_0}\left(\sum_{m\neq 0}\frac{[H_0,H_m]}{m}+\sum_{m\neq 0,n\neq 0}\frac{[H_n,H_m]}{m}\right), \qquad \text{(eq. 1.6.14)}$$

and we identify the secular terms as those with m+n=0. Thus

$$D^{(2)}=\tfrac{1}{\omega_0}\sum_{m>0}\frac{[H_{-m},H_m]}{m}, \qquad \text{(eq. 1.6.15)}$$

$$S^{(2)}=\tfrac{1}{2\omega_0^2}\left(\sum_{m\neq 0}\frac{[H_0,H_m]}{m^2}+\sum_{m\neq n,m\neq 0}\frac{[H_{-n},H_m]}{m(m-n)}\right). \qquad \text{(eq. 1.6.16)}$$

Higher-order corrections, though more complicated, can be computed in a similar way.

Expressions for the Van Vleck transformation expansion to second order have already been found,[22] but the tilting operator, $S^{(1)}$, was not given and the method could not be easily extended to higher orders. A method similar to the Van Vleck Transformation operator expansion was previously[23] used to compute $S^{(1)}$. For homogeneously coupled spin-1/2 nuclei the second-order term, $D^{(2)}$,analogous to equation 1.6.15, was shown to contain two different parts obtained when expanding the sums over the nuclear indices in the commutators.[22,23] The first part contains two spin contributions, of the $I_Z^{(i)}+I_Z^{(j)}$type, that only induce a shift of the transition and commute with $D^{(1)}=H_0$. The second part contains three spin contributions that do not shift the line and do not commute with H_0.

The Van Vleck Transformation method is not restricted to the dipolar case and can be applied, for instance, to the quadrupolar case treated previously. The prerequisite for efficient use of the Van Vleck Transformation is the possibility of expanding the

perturbation, $H^{(1)}$, into contributions which satisfy the commutation relation in equation 1.6.10. Indeed, the results of the two methods are identical for this case and, for higher-order contributions, the Van Vleck Transformation provides the results in a much simpler way. However, in other cases, this transformation may be cumbersome for second-order calculations (for instance, when different spins are involved) or not even tractable if we are interested in a full diagonalization of a degenerate Hamiltonian.

Section 1.7: Explanation of the Difficulties with Average Hamiltonian Theory

We will now discuss why Average Hamiltonian Theory gave incorrect results for the case of the quadrupolar nucleus in a large magnetic field taken to second order. We begin by describing in what sense AHT provides the "correct answer". As was shown in section 1.3, when using Average Hamiltonian Theory, one must first convert the Hamiltonian,

$$H = -\omega_0 I_Z + H_{pert}, \qquad \text{(eq. 1.7.1)}$$

into the rotating frame,

$$\tilde{H}(t) = e^{i\omega t I_Z} H_{pert} e^{-i\omega t I_Z} = \sum_m H_m e^{-im\omega_0 t} \qquad \text{(eq. 1.7.2)}$$

where it becomes time-dependent, and then average it with Average Hamiltonian Theory over the Larmor period, $t_c = 2\pi/\omega_0$, to obtain the effective Hamiltonian $\overline{H} = \overline{H}^{(0)} + \overline{H}^{(1)} + \overline{H}^{(2)} + \ldots$, to whatever order is necessary. To the first-order average Hamiltonian, one obtains[19,24],

$$\overline{H} = H_0 + \sum_{m>0} \frac{[H_{-m}, H_m]}{m\omega_0} - \sum_{m\neq 0} \frac{[H_0, H_m]}{m\omega_0} + \ldots \qquad \text{(eq. 1.7.3)}$$

The problem with the Average Hamiltonian Theory approach to truncation comes from the assumption that all the observable transitions are actually being observed. This assumption coupled with the stroboscopic nature of Average Hamiltonian Theory results in a folding of multiple quantum transitions into the single quantum spectrum. To

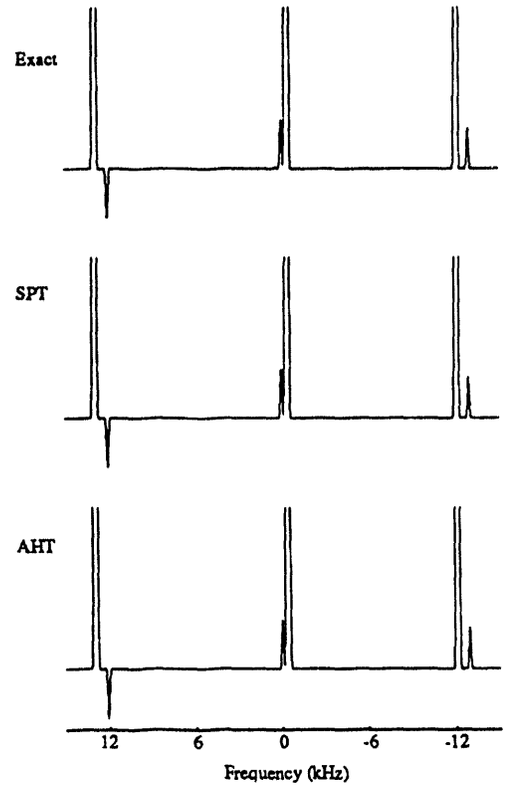

Fig. 1.7.1. Exact, Static Perturbation Theory (SPT), and Average Hamiltonian Theory (AHT) simulations of the NMR spectrum of a static single-crystal sample, containing equivalent uncoupled quadrupolar nuclei of spin 3/2. The SPT propagator was calculated as in figure 1.4.1 but using the tilting operator V expanded to first order. The dwell time in all three simulations is equal to the Larmor period. The vertical scale has been expanded 525 times full scale to show the small Zeeman "forbidden" transitions folded into the $\Delta m = \pm 1$ spectrum. The simulation was performed by Philip Grandinetti.

emphasize these points an additional set of exact, Static Perturbation Theory, and Average Hamiltonian Theory simulations sampled at multiples of the Larmor period was performed, and is shown in Fig. 1.7.1. In all three simulations the spectrum consists of three main Zeeman allowed transitions and three Zeeman forbidden transitions of much less intensity which arise from multiple-quantum transitions that are folded into the spectral window. Both Average Hamiltonian Theory and Static Perturbation Theory correctly reproduce all of the frequencies and amplitudes of the exact simulation.

However, while the Zeeman forbidden multiple quantum transitions can be unfolded in the exact and Static Perturbation Theory simulations simply by increasing the spectral window, this is not the case in the Average Hamiltonian Theory simulation which must be sampled at multiples of the Larmor period. The multiple quantum lines in the Average Hamiltonian Theory simulation cannot be unfolded with a dwell time shorter than the Larmor period, and in place of Average Hamiltonian Theory, Floquet Theory[25] is needed to separate the signal contributions from the different transition orders. Floquet Theory, as described by Maricq[26] requires the calculation of an additional time-dependent operator, $P(t)$, to yield the effective propagator in the rotating frame,

$$\tilde{U}_F(t) = P(t)e^{-i\bar{H}t}, \qquad \text{(eq. 1.7.4)}$$

which is valid at all times. When compared to the propagator obtained from Static Perturbation Theory or Van Vleck Transformation in the rotating frame,

$$\tilde{U}_{VVT}(t) = e^{-i\omega_0 t I_z} W e^{-iDt} W^\dagger = e^{-i\omega_0 t I_z} W e^{i\omega_0 t I_z} W^\dagger e^{-iWD^\circ W^\dagger t}, \qquad \text{(eq. 1.7.5)}$$

where

$$D^\circ = D + \omega I_z = D^{(1)} + D^{(2)} + \ldots, \qquad \text{(eq. 1.7.6)}$$

one can see the equivalence of these two approaches by setting $P(t) = e^{-i\omega t I_z} W e^{i\omega t I_z} W^\dagger$ and $\overline{H} = WD^\circ W^\dagger$. Note that under conditions of stroboscopic sampling at multiples of t_c, both propagators reduce to the Average Hamiltonian Theory propagator with the effective Hamiltonian given by equation 1.7.2, which is equivalent to a second-order expansion of $WD^\circ W^\dagger$,

$$\overline{H} = WD^\circ W^\dagger = D^{(1)} + D^{(2)} + i[D^{(1)}, S^{(1)}] + \ldots \qquad \text{(eq. 1.7.7)}$$

Thus, the truncated Hamiltonian obtained from Average Hamiltonian Theory is correct, but, of course, results in spectra that would never be observed in practice since the typical bandwidth of an NMR spectrometer is too small to allow signals over many megahertz to be aliased into the spectrum. It should be noted, however, that Static Perturbation Theory has an advantage over Floquet theory that the perturbation expansion of W in irreducible tensor form allows one to analytically separate the signal contributions from the different transition orders, thus avoiding the short dwell times needed to prevent aliasing of the multiple quantum transitions. When only Zeeman-allowed transitions are needed, W can be simply $\mathbf{1}$, and only the calculation of D is required. Floquet theory, however, requires the additional calculation of $P(t)$ even for Zeeman-allowed transitions.

In the last several sections, we have attempted to present a general and consistent framework for calculating the higher-order terms in the perturbation expansions used in NMR. We have shown that Average Hamiltonian theory must be carefully applied and that many times it is better to approach problems in NMR by using Static Perturbation Theory or the Van Vleck Transformation as we have illustrated in several examples. By exploiting the fact that the Zeeman interaction, a linear combination of I_Z operators, is the dominant interaction in NMR, irreducible-tensors expansions for the tilting matrix, V, and the effective Hamiltonian in the tilted frame, D, are obtained. Irreducible tensor

operators simplify these calculations since their commutation relationships with I_Z are simple and the matrix elements can be obtained using simple selection rules. Once V is known, one can work in a diagonal frame where operators are modified and consequently display unusual properties. Coherent averaging techniques, such as Average Hamiltonian Theory, can then be applied in this diagonal frame in the same manner as they are when no tilting is present. In addition, the perturbative expansion of V allows the NMR signal to be "filtered" according to Δm, thus avoiding aliasing problems when using small spectral widths and allowing certain sets of transitions to be singled out for study. We will use these ideas in the next couple of sections in order to determine the excitation Hamiltonians for both the simple $\Delta m = \pm 1$ case and the more complicated overtone case. We will be applying the tilting matrix in order to cast our equations in the diagonal frame and in this frame applying Average Hamiltonian Theory to zeroth order to find effective Hamiltonians for the duration of the pulse.

Section 1.8: Generation of an Effective Hamiltonian using Static Perturbation Theory or the Van Vleck Transformation

The description of the evolution and observation of a quantum mechanical system is greatly simplified by choosing a reference frame in which the Hamiltonian is the diagonal or block diagonal form. Furthermore, when applying coherent averaging procedures it is often necessary to introduce an interaction representation that, like a propagator, is more easily dealt with in a diagonal basis. Thus, if an exact diagonal form is available for the Hamiltonian, all the calculations can be carried out in the corresponding diagonal reference frame. However, if only approximate diagonalizations are available, it is important to know to what extent this affects the various operations to be carried out. As we shall see, for a given system, different levels of approximation may

be necessary depending on the kind of observation and irradiation procedures involved in the experiment.

The general procedure for producing an effective Hamiltonian is to write the desired equations in the diagonal frame, which is called the tilted frame, and then introduce the required perturbation expansions. If the Hamiltonian is diagonalized by a decomposition like that in equation 1.6.1, any operator A transforms to the tilted frame by the following operation:

$$A \rightarrow A^* = W^\dagger A W. \qquad \text{(eq. 1.8.1)}$$

In the particular case of the Hamiltonian, we have $H \rightarrow H^* = D$. In NMR, where the main contribution to the Hamiltonian is the Zeeman interaction, the analysis is simplified by two arguments. First, the transformation in equation 1.8.1 is simplified by a perturbation expansion of the operator W in terms of irreducible tensors. Second, the Hamiltonian, $H^* = D$, retains the general structure of the I_Z manifolds since it is reduced to the Zeeman interaction in zeroth order. This last statement is important because it implies that any NMR experiment can be analyzed with the same concepts and tools (rotating frames, averaging techniques, multiple quantum coherences, etc.) that are currently applied to the usual situations (where only first-order expansions without tilting are used). Thus, the system can be described by an effective Hamiltonian, given in the Zeeman eigenbasis by $H^* = D$. However, in this new representation, all the operators we usually deal with, such as the density matrix, and the radio frequency couplings, are modified by the tilting and may display some unusual properties.

Let us demonstrate this in the simple case of the observation of the free-induction decay. If the initial density matrix is $\rho(0)$ and the observable is I_X, the signal is given by

$$M(t) = Tr[e^{-iHt}\rho(0)e^{iHt}I_X]$$

$$= Tr[\rho^*(0)e^{iH^*t}I_X^*e^{-iH^*t}], \qquad \text{(eq. 1.8.2)}$$

and the second expression can be reinterpreted as the signal in a Zeeman eigenstate basis with a purely diagonal Hamiltonian, H^*, but with a modified initial density matrix and observable. The various possible transitions between levels of H^* define the frequency spectrum of $M(t)$, where the amplitudes are proportional to the matrix elements of I_X^*. Thus, the usual $\Delta m = \pm 1$ selection rule associated with the pure I_X operator does not apply in general.

However, in standard NMR experiments, the signal is observed with a tuned circuit that selects a band of frequencies around some definite Δm value. Although a general Fourier analysis of $M(t)$ is not easy, the perturbation expansion of the tilting operator, W, in irreducible tensor form provides a simple decomposition as a function of Δm. For instance, by expanding W of equation 1.6.4 to first order, and then I_X^* by using equation 1.8.1, $M(t)$ is

$$M(t) = Tr[\rho^*(0)e^{iH^*t}I_Xe^{-iH^*t}] + Tr[\rho^*(0)e^{iH^*t}[I_X, iS^{(1)}]e^{-iH^*t}], \qquad \text{(eq. 1.8.3)}$$

where the $S^{(1)}$ terms have been regrouped into a commutator. To zeroth order in W, the usual $\Delta m = \pm 1$ rule applies, and to a small error in the amplitudes, we can thus calculate the Zeeman spectrum using the untilted operators and the diagonal effective Hamiltonian, H^*, which can be approximated to any given order. This picture, in which H^* and W are not expanded to the same order, is well suited to NMR experiments, where the frequency resolution can be very high, but the amplitudes of the signals are seldom very accurate.

The addition of the time-dependent perturbation to the Hamiltonian can be handled in a similar manner provided the magnitude of the time-dependent perturbations small compared to the time-independent part of the Hamiltonian. We will first

demonstrate this for the case of rf irradiation near the Larmor frequency. In the tilted frame, the Hamiltonian for an rf field of magnitude $2\omega_{rf} = 2\gamma B_{rf}$ along the X-axis in this frame can be written as

$$H^*_{rf}(t) = 2\omega_{rf}\cos(\omega t)I^*_X$$

$$= \tfrac{\omega_{rf}}{2}(e^{i\omega t} + e^{-i\omega t})\left((I_+ + I_-) + \sum_{m\neq 0}\frac{[(I_+ + I_-), H_m]}{m\omega_0}\right), \qquad \text{(eq. 1.8.4)}$$

where the second expression was obtained by again expanding the tilting operator, W, to first order using equations 1.8.1, 1.6.4, and 1.6.12. As in the procedure used in the untilted Zeeman case,[7,26] the effect of the pulse is analyzed in a rotating frame, defined by the unitary transformation $e^{-i\omega t I_Z}$:

$$A^* \rightarrow A^\circ = e^{-i\omega t I_Z} W^\dagger A W e^{i\omega t I_Z}. \qquad \text{(eq. 1.8.5)}$$

This representation is the "rotating tilted frame," which should not be confused with the "tilted rotating frame" introduced in the analysis of multiple-pulse experiments.[12,27] The transformed density matrix $\rho^\circ(t)$ does not contain any high-frequency components, because it evolves under the Hamiltonian

$$H^\circ = H^* + \omega I_Z. \qquad \text{(eq. 1.8.6)}$$

Notice that since I_Z and H^* commute, H° is reduced to the offset and the local interactions. The effective rf Hamiltonian is obtained from the static parts of equation 1.8.4 after transforming to the tilted rotating frame and by using

$$e^{-i\omega t I_z} I_{\pm} e^{i\omega t I_z} = e^{\mp i\omega t} I_{\pm}, \qquad \text{(eq. 1.8.7)}$$

and

$$e^{-i\omega t I_z} H_m e^{i\omega t I_z} = e^{-im\omega t} H_m, \qquad \text{(eq. 1.8.8)}$$

By keeping the static parts of equation 1.8.4, we are averaging the Hamiltonian over a single Larmor period. This yields the effective rf Hamiltonian in the rotating tilted frame

$$H_{rf}^{\circ} = \omega_{rf}\left(I_X + \tfrac{1}{4\omega_0}\left(-[I_+, H_{-2}] + [I_-, H_2]\right)\right), \qquad \text{(eq. 1.8.9)}$$

which can be simplified by using the relation $[I_{\pm}, H_{\pm 2}] = 0$ to

$$H_{rf}^{\circ} = \omega_{rf}\left(I_X + \tfrac{1}{2\omega_0}\left([I_X, H_2 - H_{-2}]\right)\right). \qquad \text{(eq. 1.8.10)}$$

We have shown the basic formalism for using Static Perturbation Theory and the Van Vleck Transformation to produce an effective Hamiltonian. Even though the simple, illustrative example of a rf irradiation at the Larmor frequency has been shown, we want to apply this technique to a more interesting and less well understood problem: the excitation of the ^{14}N overtone.

Section 1.9: Excitation of the ^{14}N Overtone

The ^{14}N overtone is the weakly allowed transition between the +1 and -1 states of the spin 1 ^{14}N nucleus. Developing techniques for exciting and narrowing this transition is important for studying biomolecules and polymers in the solid state, because many of these materials contain nitrogen and ^{14}N is its most common isotope. Thus structural

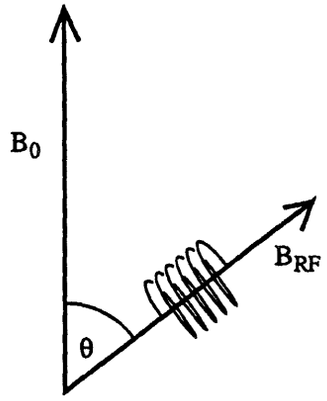

Fig. 1.9.1 the external magnetic field B_0. The laboratory z direction is defined along the external magnetic field, and the x direction is perpendicular to z and in the plane defined by the z axis and the direction of the rf magnetic field.

information could be obtained through the use of a naturally abundant nucleus that is almost ubiquitously present in these systems. Exciting the overtone removes the megahertz wide first order quadrupolar broadening of the normal ^{14}N $\Delta m = \pm 1$ transition. Thus, the overtone transition would have a second order powder pattern, as do the central transitions of odd half integer quadrupolar nuclei, which could then be narrowed by the DOR and DAS techniques[15-17] providing high-resolution ^{14}N spectra of biomolecules or polymers.

Such a transition is excited by applying an rf field oscillating at twice the ^{14}N Larmor frequency. Thus the Hamiltonian during the pulse is

$$H = H_Z + H_Q + H_{RF}, \qquad \text{(eq. 1.9.1)}$$

where

$$H_Z = -\omega_0 I_Z, \qquad \text{(eq. 1.9.2)}$$

$$H_Q = C_Q \sum_m (-1)^m R_{2,-m} T_{2,m}, \qquad \text{(eq. 1.9.3)}$$

and

$$H_{RF} = -\omega_{RF}\left(I_X \sin\theta + I_Z \cos\theta\right)\cos\left(2\omega_0 t\right). \qquad \text{(eq. 1.9.4)}$$

As can be seen in figure 1.9.1, θ is the angle between the large external field and the rf coil. Notice in equation 1.9.4, that the rf field is oscillating at twice the Larmor frequency.

As we did before, we must put this Hamiltonian in the rotating, tilted frame by using the transformation

$$H \rightarrow H^\circ = e^{-i\omega_0 t I_z} V^\dagger H V e^{i\omega_0 t I_z} - i e^{-i\omega_0 t I_z} V^\dagger \frac{\partial}{\partial t}\left(V e^{i\omega_0 t I_z}\right). \qquad \text{(eq. 1.9.5)}$$

Before, we used a slightly different rotating, tilted frame transformation, but they are essentially the same, because the extra term in equation 1.8.5 just cancels the Zeeman interaction, which we had already dropped in the earlier example. Using this transformation , we find

$$H^\circ = C_Q R_{2,0} T_{2,0} + \frac{C_Q^2}{\omega_0} \sum_{m>0} \frac{R_{2,m} R_{2,-m} [T_{2,-m}, T_{2,m}]}{m} + H_{RF}^\circ, \qquad \text{(eq. 1.9.6)}$$

where

$$H_{RF}^\circ = e^{-i\omega t I_z} V^\dagger H_{RF} V e^{i\omega t I_z}. \qquad \text{(eq. 1.9.7)}$$

Expanding the tilting operator, V, to first order and substituting for H_{RF} from equation 1.9.4 gives

$$H^{\circ}_{RF} = -\omega_{RF}\{e^{-i\omega t I_z}\left(\tfrac{1}{2}(I_+ + I_-)\sin\theta + I_Z\cos\theta\right)e^{i\omega t I_z}$$

$$+e^{-i\omega_0 t I_z}\left[\tfrac{1}{2}(I_+ + I_-)\sin\theta + I_Z\cos\theta, V^{(1)}\right]e^{i\omega_0 t I_z}\}\cos(2\omega_0 t). \qquad \text{(eq. 1.9.8)}$$

This equation is simplified by substituting for $V^{(1)}$ from equation 1.5.22 and then using equations 1.7.7 and 1.7.8 to find the static parts, which is effectively applying Average Hamiltonian Theory to zeroth order. We then find that

$$H^{\circ}_{RF} = -\frac{\omega_{RF}C_Q}{\omega_0}\left\{\left(R_{2,1}T_{2,-2} - R_{2,-1}T_{2,2}\right)\sin\theta + \left(R_{2,2}T_{2,-2} - R_{2,-2}T_{2,2}\right)\cos\theta\right\}. \qquad \text{(eq. 1.9.9)}$$

The Hamiltonian during the pulse is

$$H^{\circ} = C_Q R_{2,0}T_{2,0} + \frac{C_Q^2}{\omega_0}\sum_{m>0}\frac{R_{2,m}R_{2,-m}[T_{2,-m},T_{2,m}]}{m}$$

$$-\frac{\omega_{RF}C_Q}{\omega_0}\left\{\left(R_{2,1}T_{2,-2} - R_{2,-1}T_{2,2}\right)\sin\theta + \left(R_{2,2}T_{2,-2} - R_{2,-2}T_{2,2}\right)\cos\theta\right\}. \qquad \text{(eq. 1.9.10)}$$

The first order quadrupole shift, $C_Q R_{2,0}T_{2,0}$ does not directly effect the +1 to -1 transition, and will be dropped from any further consideration. The second order quadrupole shift, $\frac{C_Q^2}{\omega_0}\sum_{m>0}\frac{R_{2,m}R_{2,-m}[T_{2,-m},T_{2,m}]}{m}$, does effect the overtone, but we will assume that the rf field strength is large enough that it can be neglected. Unfortunately, to neglect the nutation due to the second order quadrupole interaction means that the rf-field strength must be much greater than the quadrupole coupling constant. This approximation is an unrealistic in most cases, however, we will see the general behavior of the overtone by this simplified treatment.

Some aspects of the Hamiltonian during the pulse can be made more intuitive by writing this Hamiltonian in terms of fictitious spin-1/2 operators.[28-32] Using the identity for a spin-1 that

$$T_{2,\pm 2} = I_X^{1-3} \pm iI_Y^{1-3}, \qquad \text{(eq. 1.9.11)}$$

where 1-3 indicates a coherence between the +1 and -1 states of the spin-1 nucleus. Substituting these identities into equation 1.9.9 gives

$$H^\circ = -\frac{\omega_{RF} C_Q}{\omega_0}\{\left[\left(R_{2,2} + R_{2,-2}\right)\cos\theta + \left(R_{2,1} - R_{2,-1}\right)\sin\theta\right]I_X^{1-3}$$

$$-i\left[\left(R_{2,2} - R_{2,-2}\right)\cos\theta + \left(R_{2,1} + R_{2,-1}\right)\sin\theta\right]I_Y^{1-3}\}. \qquad \text{(eq. 1.9.12)}$$

Notice that this Hamiltonian can be rewritten as

$$H^\circ = -\frac{\omega_{RF} C_Q}{\omega_0} A\left\{\cos\phi I_X^{1-3} - \sin\phi I_Y^{1-3}\right\}, \qquad \text{(eq. 1.9.13)}$$

where

$$A = \sqrt{\left[\left(R_{2,2} + R_{2,-2}\right)\cos\theta + \left(R_{2,1} - R_{2,-1}\right)\sin\theta\right]^2 - \left[\left(R_{2,2} - R_{2,-2}\right)\cos\theta + \left(R_{2,1} + R_{2,-1}\right)\sin\theta\right]^2}, \qquad \text{(eq. 1.9.14)}$$

$$\cos\phi = \frac{\left(R_{2,2} + R_{2,-2}\right)\cos\theta + \left(R_{2,1} - R_{2,-1}\right)\sin\theta}{\sqrt{\left[\left(R_{2,2} + R_{2,-2}\right)\cos\theta + \left(R_{2,1} - R_{2,-1}\right)\sin\theta\right]^2 - \left[\left(R_{2,2} - R_{2,-2}\right)\cos\theta + \left(R_{2,1} + R_{2,-1}\right)\sin\theta\right]^2}}, \qquad \text{(eq. 1.9.15)}$$

and

$$\sin\phi = \frac{i\left[\left(R_{2,2} - R_{2,-2}\right)\cos\theta + \left(R_{2,1} + R_{2,-1}\right)\sin\theta\right]}{\sqrt{\left[\left(R_{2,2} + R_{2,-2}\right)\cos\theta + \left(R_{2,1} - R_{2,-1}\right)\sin\theta\right]^2 - \left[\left(R_{2,2} - R_{2,-2}\right)\cos\theta + \left(R_{2,1} + R_{2,-1}\right)\sin\theta\right]^2}}. \qquad \text{(eq. 1.9.16)}$$

By rotating the Hamiltonian given in equation 1.9.13 by ϕ about I_Z^{1-3}, we find that

$$H'' = e^{-i\phi I_Z^{1-3}} H' e^{i\phi I_Z^{1-3}} = -\frac{\omega_{RF} C_Q}{\omega_0} A I_X^{1-3} = -\omega_{eff} I_X^{1-3}. \qquad \text{(eq. 1.9.17)}$$

This equation will allow us to simply analyze the effect of the pulse, because now its effect is a rotation about the I_X^{1-3} axis.

In order to examine the effect of the rf pulse on the overtone transition, we will calculate the magnetization immediately after the pulse. As discussed in section 1.2, the expectation value of the magnetization is

$$M_{coil}^i(t + t_p) = Tr[e^{-iHt}\rho(t_p)e^{iHt}I_{coil}^i], \qquad \text{(eq. 1.9.18)}$$

where $i = x, y$, specifying which component of the magnetization detected, t_p is the rf pulse length, t is the time after the pulse during which the overtone undergoes free precession, H is the Hamiltonian that governs the free precession which we assume to be the sum of the Zeeman and Quadrupole interactions, and I_{coil}^i is the observable angular momentum in the coil. There are two possible expressions for I_{coil}^i depending upon which component of the magnetization is measured:

$$I_{coil}^X = I_Z \cos\theta + I_X \sin\theta \qquad \text{(eq. 1.9.19)}$$

and

$$I_{coil}^{Y} = I_Z \cos\theta + I_Y \sin\theta. \qquad \text{(eq. 1.9.20)}$$

It is most convenient to calculate the magnetization in the rotating tilted frame, where the magnetization is given by

$$M_{coil}^{i}(t+t_p) = Tr[\rho^{\circ}(t_p) e^{iD^{\circ}t} I_{coil}^{\circ\, i} e^{-iD^{\circ}t}], \qquad \text{(eq. 1.9.21)}$$

where

$$I_{coil}^{\circ\, i} = e^{-i\omega_0 t I_Z} V^{\dagger} I_{coil}^{i} V e^{i\omega_0 t I_Z} = e^{-i\omega_0 t I_Z}\left(I_{coil}^{i} + [I_{coil}^{i}, V^{(1)}]\right) e^{i\omega_0 t I_Z}, \qquad \text{(eq. 1.9.22)}$$

$$D^{\circ} = D + i\omega_0 I_Z = D^{(1)} + D^{(2)} + \ldots, \qquad \text{(eq. 1.9.23)}$$

and $\rho^{\circ}(t_p)$ is the density matrix after the pulse in the rotating tilted frame. By substituting equations 1.9.20 and 1.9.20 into 1.9.22, keeping only those terms that oscillate at twice the larmor frequency, and then using equation 1.9.11 to write the resulting equations in terms of fictitious spin 1/2 operators, we find

$$I_{coil}^{\circ\, X} = -\frac{C_Q}{\omega_0} A\left\{\cos\phi I_X^{1-3} - \sin\phi I_Y^{1-3}\right\} \qquad \text{(eq. 1.9.24)}$$

and

$$I_{coil}^{\circ\, X} = -\frac{C_Q}{\omega_0} A\left\{\sin\phi I_X^{1-3} + \cos\phi I_Y^{1-3}\right\}, \qquad \text{(eq. 1.9.25)}$$

where A, $\cos\phi$, and $\sin\phi$ are given by equations 1.9.14-1.9.16.

Now that the observable is determined, we need to find the density matrix in the rotating, tilted frame after the pulse, $\rho^{\circ}(t_p)$, which is found by propagating the equilibrium density matrix, written in the same frame, with the Hamiltonian during the pulse:

$$\rho^{\circ}(t_p) = e^{i\phi I_Z^{1-3}} e^{-iH^{\circ\circ}t} \rho^{\circ\circ}(0) e^{iH^{\circ\circ}t} e^{-i\phi I_Z^{1-3}}. \qquad \text{(eq. 1.9.26)}$$

The Hamiltonian during the pulse, $H^{\circ\circ}$, is given by equation 1.9.16, and the initial density matrix is

$$\rho^{\circ\circ}(0) = \frac{\omega_o}{3kT} I_Z^{1-3}. \qquad \text{(eq. 1.9.27)}$$

This equation is the same as found in section 1.2 because, to lowest order, all the transformations that we have made commute with I_Z^{1-3}. Carrying out the operations indicated in equation 1.9.25, we find

$$\rho^{\circ}(t_p) = \frac{\omega_0}{3kT}\left[\left(\sin\phi I_X^{1-3} + \cos\phi I_Y^{1-3}\right)\sin(\omega_{eff} t_p) + I_Z^{1-3}\cos(\omega_{eff} t_p)\right] \qquad \text{(eq. 1.9.28)}$$

We have now found everything that is needed to substitute in equation 1.9.21 and determine the overtone spectrum. Since we are most interested in determining the overtone excitation efficiency, we will only calculate the magnetization at t_p, which is given by

$$M_{coil}^{i}(t_p) = Tr[\rho^{\circ}(t_p) I_{coil}^{\circ\, i}]. \qquad \text{(eq. 1.9.29)}$$

By substituting equations 1.9.24 or 1.9.25 and 1.9.28 we can calculate either the x or y

m	$R_{2,m}$
± 1	$\pm\frac{3}{2}V_{ZZ}\sin\beta\cos\beta e^{\pm i\alpha}$
± 2	$\frac{3}{4}V_{ZZ}\sin^2\beta\, e^{\pm i2\alpha}$

Table 1.9.1: Spacial Tensors for the axially symmetric case as defined by Haeberlen[27].

components of the magnetization after the pulse. These are given by

$$M^x_{coil}(t_p) = -\frac{C_Q}{3kT}A(\sin\phi\cos\phi - \sin\phi\cos\phi)\sin(\omega_{eff}t_p) = 0 \qquad \text{(eq. 1.9.30)}$$

and

$$M^x_{coil}(t_p) = -\frac{C_Q}{3kT}A(\sin^2\phi + \cos^2\phi)\sin(\omega_{eff}t_p) = -\frac{C_Q}{3kT}A\sin(\omega_{eff}t_p), \quad \text{(eq. 1.9.31)}$$

where we have used the orthogonality relations of the fictitious spin 1/2 operators, $Tr[I_i^{1-3}I_k^{1-3}] = \delta_{i,k}$ to find these equations. Equation 1.9.17 defined $\omega_{eff}t_p = \frac{\omega_{RF}C_Q}{\omega_0}At_p = \frac{\omega_{RF}\omega_Q}{\omega_0}A't_p$, which is of order $\frac{\omega_{RF}\omega_Q}{\omega_0}t_p \approx \frac{2\pi(.009MHz)(1MHz)}{28.896MHz}(10\,\mu sec) = .02$. Thus even if we apply a pulse that is ten times longer, we are in the small pulse limit, which will allow us to approximate

$$M^x_{coil}(t_p) = -\frac{C_Q}{3kT}A\omega_{eff}t_p = -\frac{\omega_{RF}C_Q^2}{3kT\omega_0}A^2t_p. \qquad \text{(eq. 1.9.32)}$$

This equation is what is needed to analyze the excitation efficiency of the overtone transition.

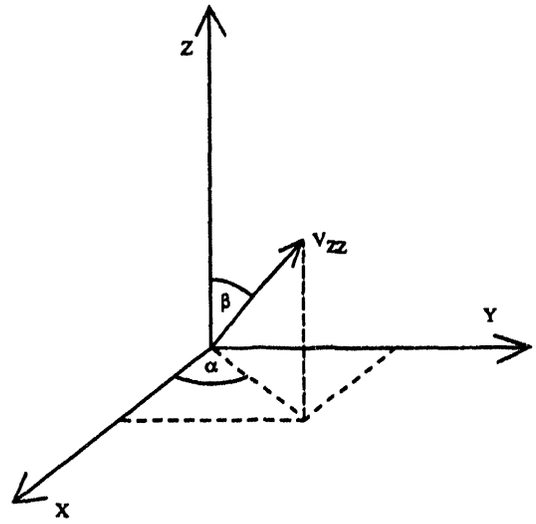

Fig. 1.9.2: Definition of the angles α and β for the axially symmetric quadrupole interaction. X, Y, Z are laboratory frame direction where Z is defined in the direction of the external magnetic field. V_{ZZ} is the direction of the Z principle axis of the quadrupole interaction.

We will examine the overtone excitation of a sample with an axially symmetric quadrupole interaction for the cases with the rf coil parallel and perpendicular to the external magnetic field ($\theta = 0$ or $\theta = \frac{\pi}{2}$). For an axially symmetric quadrupole interaction, the spacial tensors needed to find A, $\cos\phi$, and $\sin\phi$ are given in table 1.9.1. The angles α and β which appear in table 1.9.1 are defined in figure 1.9.2. With these tensors we can show that

$$A = \tfrac{3}{8} V_{ZZ} \sin^2\beta, \qquad \text{(eq. 1.9.33)}$$

$$\phi = 2\alpha, \qquad \text{(eq. 1.9.34)}$$

and

$$M^{Y}_{coil,\ \theta=0}(t_p) = -\tfrac{3}{64} \frac{\omega_{RF}\omega_Q^2}{kT\omega_0} t_p \sin^4\beta \qquad \text{(eq. 1.9.35)}$$

or the rf-coil along the external magnetic field. If the rf-coil is perpendicular to the magnetic field, we then find that

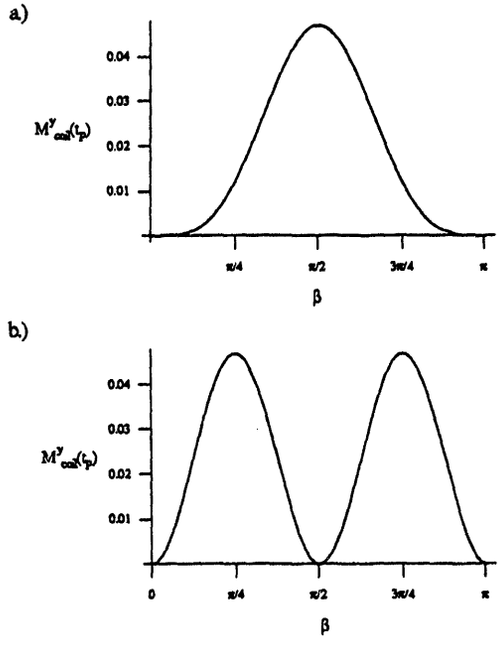

FIG. 1.9.3: The excitation efficiency of the ^{14}N overtone as a function of β, the polar angle (defined in Figure 1.5).where the quadrupolar tensor is axially symmetric a.) The excitation profile when the rf-coil is oriented along the external magnetic field. b.) The excitation profile when the rf-coil is perpendicular to this field. M^{y}_{coil} is in units where $\frac{\omega_{RF}\omega_{Q}^{2}}{kT\omega_{0}}t_{p}=1$.

$$A=\tfrac{3}{4}V_{ZZ}\sin\beta\cos\beta, \qquad \text{(eq. 1.9.36)}$$

$$\phi=\alpha, \qquad \text{(eq. 1.9.37)}$$

and

$$M^{Y}_{coil,\ \theta=\frac{\pi}{2}}(t_{p})=-\tfrac{3}{16}\frac{\omega_{RF}\omega_{Q}^{2}}{kT\omega_{0}}t_{p}\sin^{2}\beta\cos^{2}\beta. \qquad \text{(eq. 1.9.38)}$$

Intensity of the overtone transition as a function of the orientation angle for a fixed, short pulse length is shown in figure 1.9.3.

If the sample is polycrystalline, it is not obvious whether the direction of the rf-coil is going to effect the total intensity of the overtone transition. To determine this, the magnetization must be averaged over all crystallite orientations:

$$\left\langle M^{Y}_{coil}(t_p)\right\rangle = \int_{\alpha=0}^{2\pi}\int_{\beta=0}^{\pi} M^{Y}_{coil}(t_p)\sin\beta\, d\beta\, d\alpha. \qquad \text{(eq. 1.9.39)}$$

Performing this average on equations 1.9.35 and 1.9.38, we find

$$\left\langle M^{Y}_{coil,\ \theta=0}(t_p)\right\rangle = \left\langle M^{Y}_{coil,\ \theta=\frac{\pi}{2}}(t_p)\right\rangle = -\tfrac{\pi}{10}\tfrac{\omega_{RF}\omega_Q^2}{kT\omega_0}t_p \qquad \text{(eq. 1.9.40)}$$

and thus the total overtone intensity does not depend on these two rf-coil orientations. However, the shape of the observed powder pattern will depend upon the coil orientation, because different crystallites are excited which then will oscillate at different frequencies.

In this section, we have shown how the formalism presented earlier can be used to find an effective Hamiltonian that allowed us to examine the excitation of the ^{14}N overtone. We have shown that it is possible to excite the overtone in a polycrystalline sample and we have presented a formalism that can be expanded to determine the nutation effects due to the second order quadrupole interaction that we have ignored and the effects of spinning the sample. Thus the idea of an effective Hamiltonian is useful for determining the time dependence of the density matrix and thus the quantities actually observed in an experiment. However, all the time-dependent Hamiltonians that we have examined so far have be under our control. They have been due to either an artificial frame transformation or application of a coherent rf field. We have ignored the effects of

incoherent fields on our sample. These fields will lead to relaxation of the spin system and will be treated in the next section.

Section 1.10: Relaxation Theory

So far in this thesis, we have learned to calculate the interaction of nuclear spins with large, static magnetic fields and radio-frequency fields. To do this analysis, we calculated an effective Hamiltonian which then led to the time dependence of the density matrix. The initial condition for these calculations was always that the spins were in equilibrium with the rest of the lattice and thus was at the same temperature as the lattice (see the derivation of equation 1.2.13). However, we never examined how the nuclear spins came to be in equilibrium with the lattice. The examination of the process by which nuclear spins reach equilibrium is called relaxation theory, and was first analyzed by Bloembergen, Pound, and Purcell[33], and then later refined by Redfield and others[34-38].

By analogy with what occurs in atomic systems, we would expect the relaxation of the nuclear spins to be due to the coupling of the nuclear spins to the radiation field, and thus the lifetime could be calculated using Fermi's golden rule[1]. However, as shown by Abragam in his book[7], this effect is much too small to explain the relaxation times actually seen. Bloombergen, Pound, and Purcell have shown that the appropriate explanation for nuclear relaxation is the interaction of the nuclei with motions of the molecules in the sample, which is normally referred to as coupling to the lattice. The nuclei interact with these motions through the modulations of the dipole-dipole interaction, chemical shift interaction, quadrupole interaction, ect that the motions create. In order to describe the coupling between the nuclei and the motions, we will present Redfield theory which describes the relaxation of every element in the density matrix. This theory will only be appropriate to describe the relaxation where the coupling to the

lattice is weak. We will ignore the other case. We will treat the motions of the lattice classically and the nuclear system quantum mechanically (a semiclassical treatment).

With a semiclassical treatment, the nuclear spin Hamiltonian is partitioned into a large time-independent term, which contains the Zeeman interaction and all the static internal interactions, and a much smaller time dependent term, which contains the coupling to the motions of the lattice:

$$H(t) = H_0 + H_1(t). \qquad \text{(eq. 1.10.1)}$$

As we did in sections 1.2 and 1.8, we can now go into the rotating frame to remove the effects of the time-independent Hamiltonian and find a short time approximation for $\rho^*(t)$,

$$\rho^*(t) = \rho^*(0) - i\int_0^t [H_1^*(t'),\rho^*(0)]dt' - \int_0^t\int_0^{t'} [H_1^*(t'),[H_1^*(t''),\rho^*(0)]]dt''dt', \quad \text{(eq. 1.10.2)}$$

where

$$\rho^*(t) = e^{-iH_0t}\rho(t)e^{iH_0t} = e^{-iDt}V^\dagger\rho(t)Ve^{iDt} \approx e^{-iDt}\rho(t)e^{iDt}, \qquad \text{(eq. 1.10.3)}$$

and similarly

$$H_1^*(t) \approx e^{-iDt}H_1(t)e^{iDt}. \qquad \text{(eq. 1.10.4)}$$

In both of these equations, we have neglected the effect of tilting. If we take the derivative of equation 1.10.2 with respect to t, we find

$$\frac{\partial\rho^*(t)}{\partial t} = -i[H_1^*(t),\rho^*(0)] - \int_0^t [H_1^*(t),[H_1^*(t'),\rho^*(0)]]dt'. \qquad \text{(eq. 1.10.5)}$$

Both the Hamiltonian and the density matrix are independent statistical quantities in this formalism, thus the Hamiltonian, $H_1^*(t)$, must be averaged over the motions of the sample. This average can be made to disappear, because any part of it that does not average to zero can be included in H_0. This implies that the first term on the right hand side of equation 1.10.3 is zero and this equation becomes

$$\frac{\partial \rho^*(t)}{\partial t} = -\int_0^t [H_1^*(t),[H_1^*(t'),\rho^*(0)]]dt' . \qquad \text{(eq. 1.10.6)}$$

If the motions that are responsible for the time dependence of $H_1^*(t)$ have a correlation time that is much shorter than the interval over which we want to calculate the change of the density matrix, then the upper limit on the integration can be extended to infinity, because the contribution to the value of the integral beyond the correlation time is negligible. Secondly, if we assume that the coupling to the lattice is weak, we can replace $\rho^*(0)$ by $\rho^*(t)$. This assumption is equivalent to assuming that the time over which we observe the change in the density matrix is much shorter than T_2. These assumptions are referred to as the coarse graining approximation, because they limit our ability to examine the density matrix for times such that $t_c << t << T_2$. Within this approximation, equation 1.10.4 becomes

$$\frac{\partial \rho^*(t)}{\partial t} = -\int_0^\infty [H_1^*(t),[H_1^*(t'),\rho^*(t)]]dt' . \qquad \text{(eq. 1.10.7)}$$

Because of the semiclassical treatment of the lattice, this equation relaxes towards an infinite temperature condition, equal probabilities of all states; however, if the full quantum mechanical treatment is performed[7], it can be shown that the correct equation is obtained by replacing $\rho^*(t)$ with $\rho^*(t) - \rho_{eq}^*(t)$. We will make this substitution in all

further equations. A matrix element expansion of the corrected version of equation 1.10.7 is the Redfield equation; however, we find that an operator expansion of this equation is more convenient.

To find the operator equation, the interaction Hamiltonian between the spins and the lattice, $H_1(t)$, is expanded in terms of irreducible tensors,

$$H_1(t) = \sum_i \sum_l C_i \sum_m (-1)^m R^i_{l,-m}(t) T^i_{l,m}, \qquad \text{(eq. 1.10.8)}$$

where i labels the different possible interactions between the spins and the lattice (the dipole-dipole, chemical shift, and quadrupole interactions are most commonly responsible for relaxation),and l and m label the rank and order of the tensors., which are written in the laboratory frame. The $R^i_{l,-m}(t)$ are functions of time because of the motions of the lattice. Substituting equation 1.10.8 into 1.10.7, we find

$$\frac{\partial \rho^*(t)}{\partial t} = -\int_0^\infty \sum_{i,i'} \sum_{l,l'} C_i C_{i'} \sum_{m,m'} (-1)^{m+m'} R^i_{l,-m}(t) R^{i'}_{l',-m'}(t') [T^{i\,*}_{l,-m}(t), [T^{i'\,*}_{l',-m'}(t'), \rho^*(t) - \rho^*_{eq}(t)]] dt',$$

(eq. 1.10.9)

where $T^{i\,*}_{l,m}(t) = e^{-iDt} T^i_{l,m} e^{iDt}$. If we substitute $t' = t + \tau$ and expand $T^{i\,*}_{l,m}(t)$ in a Fourier series,

$$T^{i\,*}_{l,m}(t) = \sum_r A^{i,r}_{l,m} e^{-i\omega^r_{l,m} t}, \qquad \text{(eq. 1.10.10)}$$

equation 1.10.9 can be written as

$$\frac{\partial \rho^*(t)}{\partial t} = -\sum_{i,i'} \sum_{l,l'} \sum_{m,m'} \sum_{r,r'} \delta_{\omega^r_{l,m}, -\omega^{r'}_{l',m'}} (-1)^{m+m'} J^{i,i'}_{l,l',m,m'}\left(\omega^{r'}_{l',m'}\right) [A^{i,r}_{l,-m}, [A^{i',r'}_{l',-m'}, \rho^*(t) - \rho^*_{eq}(t)]],$$

(eq. 1.10.11)

where

$$J^{i,i'}_{l,l',m,m'}\left(\omega^{r'}_{l',m'}\right)=\int_0^{\infty}\left\langle C_i C_{i'} R^{i}_{l,-m}(t) R^{i'}_{l',-m'}(t+\tau)\right\rangle e^{i\omega^{r'}_{l',m'}\tau}d\tau, \qquad \text{(eq. 1.10.12)}$$

is the spectral density of the motion and $\langle\ \rangle$ explicitly indicates that an ensemble average over all initial and final configurations must be performed. In equation 1.10.11, we have kept only those terms with $\omega^{r}_{l,m}=-\omega^{r'}_{l',m'}$ because the other terms are oscillating too rapidly to contribute to the integral of this equation. This equation gives us the rate of change of the density matrix, however, we do not directly observe the density matrix in an experiment. We measure the rate of change of some observable, Q, which is given by

$$\frac{\partial <Q>}{\partial t}=Tr\left(\frac{\partial \rho^{*}}{\partial t}Q\right)$$

$$=-\sum_{i,i'}\sum_{l,l'}\sum_{m,m'}\sum_{r,r'}\delta_{\omega^{r}_{l,m},-\omega^{r'}_{l',m'}}(-1)^{m+m'}J^{i,i'}_{l,l',m,m'}\left(\omega^{r'}_{l',m'}\right)Tr\left\{\left[A^{i',r'}_{l',-m'},\left[A^{i,r}_{l,-m},Q\right]\right]\left(\rho^{*}(t)-\rho^{*}_{eq}(t)\right)\right\},$$

(eq. 1.10.13)

where we have used the identity $Tr([A,[B,C]]D)=Tr([B,[A,D]]C)$. This equation is the most general operator form of the Redfield equation. It is much more general that what will be needed in this thesis and we will simplify it by working with only a single relaxation mechanism at a time and neglecting the important cross-correlation effects. Under these conditions, the summations over the i's and l's are not needed and $m=-m'$. This simplifies equation 1.10.13 to

$$\frac{\partial <Q>}{\partial t}=-\sum_{m}\sum_{r,r'}\delta_{\omega^{r}_{l,m},-\omega^{r'}_{l,-m}}J_{m}\left(\omega^{r'}_{l,-m}\right)Tr\left\{\left[A^{r}_{l,m},\left[A^{r'}_{l,-m},Q\right]\right]\left(\rho^{*}(t)-\rho^{*}_{eq}(t)\right)\right\}, \quad \text{(eq. 1.10.14)}$$

m	$T_{2,m}$
0	$\sqrt{\frac{2}{3}}\left\{I_Z S_Z - \frac{1}{4}\left(I_+ S_- + I_- S_+\right)\right\}$
±1	$\mp\frac{1}{2}\left(I_\pm S_Z + I_Z S_\pm\right)$
±2	$\frac{1}{2} I_\pm S_\pm$

Table 1.10.1: Definition of Spherical Tensor Operators used to describe the Dipole-Dipole Interaction.

where

$$J_m\left(\omega^{r'}_{l,-m}\right) = \int_0^\infty \left\langle C^2 R_{l,-m}(t) R_{l,m}(t+\tau)\right\rangle e^{i\omega^{r'}_{l,-m}\tau} d\tau. \qquad \text{(eq. 1.10.15)}$$

The correlation function in equation 1.10.15 is given by

$$\left\langle C^2 R_{l,-m}(t) R_{l,m}(t+\tau)\right\rangle = \int_{\Omega(t+\tau)} C^2 R_{l,-m}(t) R_{l,m}(t+\tau)\, p\left(\Omega(t):\Omega(t+\tau)\right) d\Omega(t+\tau), \qquad \text{(eq. 1.10.16)}$$

where $p\left(\Omega(t):\Omega(t+\tau)\right)$ is the conditional probablitiy to go from orientation $\Omega(t)$ at time, t, to $\Omega(t+\tau)$ at $t+\tau$. This correlation function is a real function when the conditional probablity is a real, even function. This constriant is true for any symmetric motions of the molecule under study and is always true when the molecule is undergoing isotropic reorientation. Equation 1.10.14 can be used to derive the longitudinal and transverse relaxation times T_1 and T_2, respectively, for different circumstances.

As an example, we will derive the longitudinal relaxation time, T_1, for the case of two resolved spins relaxed by the dipole-dipole interaction. In this example, the static Hamiltonian is

$$H_0 = D = \omega_I I_Z + \omega_S S_Z \qquad \text{(eq. 1.10.17)}$$

and the fluctuating Hamiltonian responsible for the relaxation is

$$H_1 = C_D \sum_m (-1)^m R_{2,-m}(t) T_{2,m}, \qquad \text{(eq. 1.10.18)}$$

where

$$C_D = -2\gamma_I \gamma_S, \qquad \text{(eq. 1.10.19)}$$

$$R_{2,m}(t) = \sqrt{\tfrac{6\pi}{5}} \frac{Y_{2,m}(\theta(t),\phi(t))}{r(t)^3}, \qquad \text{(eq. 1.10.20)}$$

and the $T_{2,m}$ are given in table 1.10.1. The $Y_{2,m}(\theta(t),\phi(t))$ are spherical harmonics describing the orientation of the internuclear vector whose length is $r(t)$ by the polar angle $\theta(t)$ and the azimuthal angle $\phi(t)$. We can now go into the interaction frame defined by equation 1.10.17 and find $T^*_{2,m}$, $A^r_{2,m}$, and $\omega^r_{l,m}$:

$$T^*_{2,0}(t) = \sqrt{\tfrac{2}{3}}\left\{ I_Z S_Z - \tfrac{1}{4}\left(I_+ S_- e^{-i(\omega_I - \omega_S)t} + I_- S_+ e^{+i(\omega_I - \omega_S)t} \right) \right\},$$

$$A^0_{2,0} = \sqrt{\tfrac{2}{3}} I_Z S_Z, \qquad A^1_{2,0} = -\tfrac{\sqrt{6}}{12} I_+ S_-, \qquad A^2_{2,0} = -\tfrac{\sqrt{6}}{12} I_- S_+,$$

$$\omega^0_{2,0} = 0, \qquad \omega^1_{2,0} = \omega_I - \omega_S, \qquad \omega^2_{2,0} = -(\omega_I - \omega_S),$$

$$T^*_{2,\pm 1}(t) = \mp \tfrac{1}{2}\left\{ I_\pm S_Z e^{\mp i\omega_I t} + I_Z S_\pm e^{\mp i\omega_S t} \right\}, \qquad \text{(eq. 1.10.21)}$$

$$A^0_{2,\pm 1} = \mp \tfrac{1}{2} I_\pm S_Z, \qquad A^1_{2,\pm 1} = \mp \tfrac{1}{2} I_Z S_\pm,$$

$$\omega^0_{2,\pm 1} = \pm \omega_I, \qquad \omega^1_{2,\pm 1} = \pm \omega_S,$$

$$T^*_{2,\pm 2}(t) = \tfrac{1}{2} I_\pm S_\pm e^{\mp i(\omega_I + \omega_S)t},$$

$$A^0_{2,\pm 2} = \tfrac{1}{2} I_\pm S_\pm,$$

$$\omega^0_{2,\pm 1} = \pm(\omega_I + \omega_S).$$

Since we are calculating the longitudinal relaxation rate, the observable, Q, is I_Z, and equation 1.10.14 becomes

$$\frac{\partial < I_Z >}{\partial t} = -J_0(0)Tr\left\{\left[A^0_{2,0},[A^0_{2,0},I_Z]\right]\left(\rho^*(t)-\rho^*_{eq}(t)\right)\right\}$$

$$-J_0(\omega_I-\omega_S)Tr\left\{\left[A^1_{2,0},[A^2_{2,0},I_Z]\right]\left(\rho^*(t)-\rho^*_{eq}(t)\right)\right\}$$

$$-J_0(\omega_I-\omega_S)Tr\left\{\left[A^2_{2,0},[A^1_{2,0},I_Z]\right]\left(\rho^*(t)-\rho^*_{eq}(t)\right)\right\}$$

$$-J_1(\omega_I)Tr\left\{\left[A^0_{2,1},[A^0_{2,-1},I_Z]\right]\left(\rho^*(t)-\rho^*_{eq}(t)\right)\right\}$$

$$-J_1(\omega_I)Tr\left\{\left[A^0_{2,-1},[A^0_{2,1},I_Z]\right]\left(\rho^*(t)-\rho^*_{eq}(t)\right)\right\}$$

$$-J_1(\omega_S)Tr\left\{\left[A^1_{2,1},[A^1_{2,-1},I_Z]\right]\left(\rho^*(t)-\rho^*_{eq}(t)\right)\right\}$$

$$-J_1(\omega_S)Tr\left\{\left[A^1_{2,-1},[A^1_{2,1},I_Z]\right]\left(\rho^*(t)-\rho^*_{eq}(t)\right)\right\}$$

$$-J_2(\omega_I+\omega_S)Tr\left\{\left[A^0_{2,2},[A^0_{2,-2},I_Z]\right]\left(\rho^*(t)-\rho^*_{eq}(t)\right)\right\}$$

$$-J_2(\omega_I+\omega_S)Tr\left\{\left[A^0_{2,-2},[A^0_{2,2},I_Z]\right]\left(\rho^*(t)-\rho^*_{eq}(t)\right)\right\}. \qquad \text{(eq. 1.10.22)}$$

Assuming I and S are spin $\frac{1}{2}$, we can use the definitions in equations 1.10.21 and the commutators defined in table 1.10.2 to find

$$\frac{\partial < I_Z >}{\partial t} = -\rho\left(< I_Z > - < I_Z >_{eq}\right) - \sigma\left(< S_Z > - < S_Z >_{eq}\right), \qquad \text{(eq. 1.10.23)}$$

where

$$\rho = \tfrac{1}{12}\left[J_0(\omega_I - \omega_S) - 3J_1(\omega_I) + 6J_2(\omega_I + \omega_S)\right], \qquad \text{(eq. 1.10.24)}$$

$$\sigma = \tfrac{1}{12}\left[-J_0(\omega_I - \omega_S) + 6J_2(\omega_I + \omega_S)\right], \qquad \text{(eq. 1.10.25)}$$

and

$$J_m\left(\omega_{I,-m}^{r'}\right) = \tfrac{3\pi}{5}(-1)^m C_D^2 \int_{-\infty}^{\infty} \left\langle \frac{Y_{2,m}^*(\theta(t),\phi(t))Y_{2,m}(\theta(t+\tau),\phi(t+\tau))}{r(t)^3 r(t+\tau)^3} \right\rangle e^{i\omega_{I,-m}^{r'}\tau} d\tau. \qquad \text{(eq. 1.10.26)}$$

Equation 1.10.23 is one of the two coupled equations describing the system. The entire systems of equations is best described in matrix form, Louisville space, as

$$\frac{\partial}{\partial t}\begin{pmatrix}\langle I_z\rangle \\ \langle S_z\rangle\end{pmatrix} = \begin{pmatrix}\rho & \sigma \\ \sigma & \rho\end{pmatrix}\begin{pmatrix}\langle I_z\rangle - \langle I_z\rangle_{eq} \\ \langle S_z\rangle - \langle S_z\rangle_{eq}\end{pmatrix}. \qquad \text{(eq. 1.10.27)}$$

These equations are the Solomon equations.

Spin 1/2 Commutators

$$[I_Z, I_\pm] = \pm I_\pm$$

$$[I_+, I_-] = 2I_Z$$

$$[I_+S_-, I_-S_+] = I_Z - S_Z$$

$$[I_+S_+, I_-S_-] = I_Z + S_Z$$

Table 1.10.2: Spin 1/2 Commutators used in deriving relaxation equations.

Equation 1.10.23 makes the interesting prediction that the measured longitudinal relaxation rate depends on the exactly how the experiment is performed. There are three distinct experiments that can be performed. First, the I spin can be inverted while the S spin is saturated. Under these conditions, the equation of motion of the I spin is

$$\frac{\partial < I_Z >}{\partial t} = -\rho\left(< I_Z > - < I_Z >_{eq} \right), \qquad \text{(eq. 1.10.28)}$$

and the magnetization recovers with a rate ρ. To determine what happen in the other two cases the relaxation equation, defined in equation 1.10.27, must be integrated. This is done by diagonalizing the rate matrix and then solving the resulting differential equation. The rate matrix can be diagonalized in the two spin case with the unitary transformation

$$U = \begin{pmatrix} 1 & 1 \\ 1 & -1 \end{pmatrix}. \qquad \text{(eq. 1.10.29)}$$

The inverse of this transformation is

$$U^{-1} = \frac{1}{2}\begin{pmatrix} 1 & 1 \\ 1 & -1 \end{pmatrix}. \qquad \text{(eq. 1.10.30)}$$

Using this unitary transformation, the solution for the differential equation in equation 1.10.27 is

$$\langle I_Z \rangle - \langle I_Z \rangle_{eq} = \tfrac{1}{2}\left[\left(e^{-(\rho+\sigma)t} + e^{-(\rho-\sigma)t} \right)\left(\langle I_Z \rangle_{initial} - \langle I_Z \rangle_{eq} \right) + \left(e^{-(\rho+\sigma)t} - e^{-(\rho-\sigma)t} \right)\left(\langle S_Z \rangle_{initial} - \langle S_Z \rangle_{eq} \right) \right]. \qquad \text{(eq. 1.10.31)}$$

The equation for S_Z is found by exchanging the roles of I_Z and S_Z in equation 1.10.31. The second experiment that can be performed on this system is the simultaneous

inversion of both spins: $\langle I_z \rangle = -\langle I_z \rangle_{eq}$ and $\langle S_z \rangle = -\langle S_z \rangle_{eq}$. Assuming that I and S are a resolved homonuclear system, the expected recovery of the system is

$$\langle I_z \rangle = \langle I_z \rangle_{eq} \left(1 - 2e^{-(\rho+\sigma)t}\right) \qquad \text{(eq. 1.10.32)}$$

and

$$\langle S_z \rangle = \langle S_z \rangle_{eq} \left(1 - 2e^{-(\rho+\sigma)t}\right). \qquad \text{(eq. 1.10.33)}$$

In this case, the system recovers monoexponentially with a rate $\rho + \sigma$. If only the I spin is inverted, initially $\langle I_z \rangle = -\langle I_z \rangle_{eq}$ and $\langle S_z \rangle = \langle S_z \rangle_{eq}$. The expected recovery of the system is now

$$\langle I_z \rangle = \langle I_z \rangle_{eq} \left(1 - e^{-(\rho+\sigma)t} - e^{-(\rho-\sigma)t}\right) \qquad \text{(eq. 1.10.34)}$$

and

$$\langle S_z \rangle = \langle S_z \rangle_{eq} \left(1 - e^{-(\rho+\sigma)t} + e^{-(\rho-\sigma)t}\right). \qquad \text{(eq. 1.10.35)}$$

Now the I magnetization recovers biexponentially. So as we can see the measured T_1 depends upon which experiment is performed. Thus caution must be used when attempting to interpret this parameter.

Throughout this first chapter, we have shown how to calculate the effect of static and time dependent Hamiltonians on a spin system. The static interactions we now know how to deal with include interaction with the large external magnetic field used in NMR as well as the smaller internal interactions, such as the dipole-dipole coupling, quadrupole coupling, and scalar coupling (J-coupling). We have also determined how to calculate the

effects of time-dependent interactions, such as interaction with the oscillating rf-field used to excite the spins and random time-dependent interactions that lead to relaxation of the spin system back to equilibrium. The rest of this thesis will be investigating relaxation processes in nuclear magnetic resonance spectroscopy. These relaxation processes will be investigated in semiconductor nanocrystals, biological molecules, and ^{13}C enriched solids. By measuring the relaxation properties of these materials, we will determine both dynamic information about the motions of the molecules and also structural information that will that will constrain the geometry of the molecules.

Chapter 2: NMR Studies of the Structure and Surface Dynamics of Semiconductor Nanocrystals

Section 2.1: Introduction to Nanocrystals

A novel form of matter which has recently received much theoretical and experimental interest is the nanocrystal. A nanocrystal is intermediate in size between the molecular and the bulk causing its physical properties to become size dependent.[1,2] For example, the energy at which light is absorbed depends on the radius of the nanocrystal. The size dependence of the properties of the nanocrystal has lead to the realization that they might be tuned for technological purposes;[3,4] however, before these nanocrystals can be used in devices the relationship between the structure of the nanocrystal and its properties must be understood. In this chapter, we present NMR studies of cadmium sulfide nanocrystals capped with thiophenol molecules in order to obtain structural information about these nanocrystals.

The structure of the nanocrystal can be loosely divided into two parts, the surface and the core (or interior). Our studies address only the surface of the nanocrystals, which, not surprisingly, plays an important role in determining many of size dependent properties of the nanocrystal. For example, trapping of the optically produced hole, the fluorescence of the nanocrystal, the surface energy and hence the phase diagram all depend upon the structure of the surface. In addition, it is necessary to synthetically manipulate the nanocrystal surface to achieve solubility in a wide variety of organic solvents. Thus, a study of the organic molecules bound to the surface of the nanocrystal is crucial to understanding these systems. Despite its importance, the surface structure of these particles

has so far received relatively little attention. We will approach this important problem by examining the solution state ^{1}H and ^{13}C NMR of the thiophenol molecules bound to the surface, which will tell us not only about how the thiophenols are bound to the surface, but also about their motions on the surface.

Section 2.2: ^{1}H NMR Results of Thiophenol of CdS Nanocrystals

We have used one- and two-dimensional solution state ^{1}H-NMR to characterize the organic molecules bound to the surface of CdS nanocrystals. To perform the solution state studies, Vicki Colvin synthesized pyridine soluble, thiophenol capped nanocrystals using inverse micelles according to standard procedures,[5] except that they were not annealed and thus their interior was poorly crystalline. The non-annealed samples were used because annealing is performed in quinoline at high temperatures, which greatly complicates the NMR spectra. NMR samples of nanocrystals were prepared by dissolving 5 mg of CdS

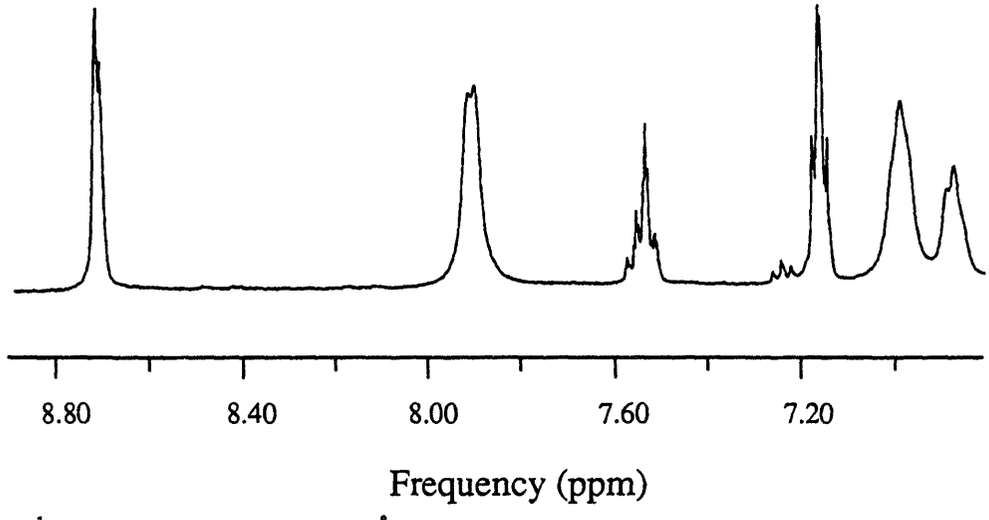

Fig. 2.2.1: ^{1}H NMR spectrum of an 11.8Å CdS Nanocrystal in d_5-pyridine at room temperature. The sample was prepared by dissolving 5 mg of dry powder of nanocrystals in 0.5 ml of 99.99% deuterated solvent. The spectrum was taken at a ^{1}H Larmour frequency of 400 MHz on a Bruker AM400 spectrometer.

nanocrystals in 0.5 ml of 100% d_5-pyridine. 400 MHz ^{1}H-NMR spectra were recorded within a week of particle synthesis at room temperature with Bruker AM-400 and AM-400X spectrometers.

In figure 2.2.1 is a representative proton NMR spectrum of a thiophenol capped nanocrystal in d_5-pyridine. As can be seen, despite the possibility of many different environments on the nanocrystal surface causing a featureless ^{1}H NMR spectrum, we have observed high resolution spectra that are shifted with respect to free thiophenol. This immediately tells us that the thiophenol molecules are bound to the surface and that the distribution of thiophenol sites on the surface is relatively small. The proton NMR spectra of the model compounds $Cd(SC_6H_5)_2$ and $[Cd(SC_6H_5)_2]_2[H_3CPCH_2CH_2PCH_3]$ have

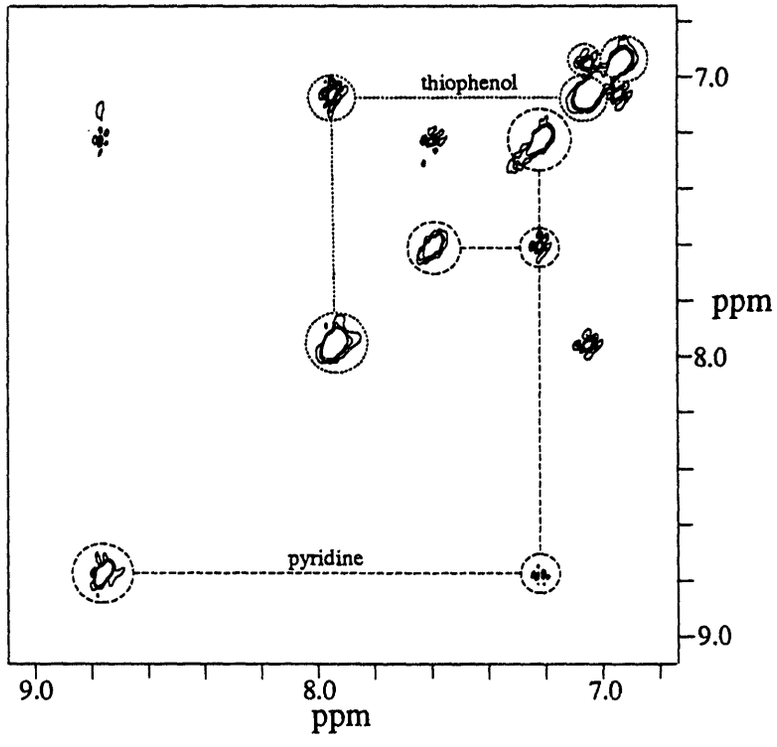

Fig. 2.2.2: Amplitude modulated COSY spectrum CdS nanocrystals in d_5-pyridine. The spectrum was taken within one week after preparation at room temperature at a ^{1}H frequency of 400 MHz..

identical spectra to that of the thiophenol ligands on the semiconductor nanocrystals. The crystal structures of these two model compounds are known[6,7 and show that the thiophenol ligands bind both terminally to a single cadmium atom and bridging between two cadmium atoms. Comparison of these spectra with that of the nanocrystal implies that thiophenol binds to cadmium atoms on the surface in a similar way in both the nanocrystal and the model compounds. Unfortunately, we cannot use these data to specify whether thiophenol binds to the nanocrystal surface in a terminal or bridging manner, as the solution state structure of the models is unknown.

Two-dimensional phase-sensitive COSY spectra[8,9] were used to assign the chemical shifts. As shown in figure 2.2.2, we see only one set of resonances which are attributable to the *ortho-*, *meta-* and *para-* protons of thiophenol and which show the corresponding characteristic connectivities. Thus, the peaks at 7.91, 7.03 and 6.92 ppm are assigned to the *ortho*, *meta*, and *para* protons respectively of thiophenol molecules bound to the surface. The peaks at 8.71, 7.19 and 7.56 ppm are due to the *ortho*, *meta*, and *para* protons respectively of residual protonated pyridine co-purified from the synthesis procedure. These resonances are identical to those for pure pyridine.

The surface of the nanocrystal changes with time, as can be seen from the appearance of new peaks at 7.25, 7.38, and 8.34 ppm in the ^1H spectra. The intensity of these peaks is seen to increase with time, while the bound thiophenol peaks decrease with approximately the same rate. For particles in pyridine solution at room temperature the bound thiophenol ligand resonances disappear in approximately 16 days. The same change in the NMR spectrum is seen in samples kept as powders, however, the rate slowed considerably. For this reason, many of the samples of nanocrystals were studied within one week of their synthesis before degradation could occur. Russell Bowers and Robert Grubbs identified the degradation product as the dithiophenol, $C_5H_5SSC_5H_5$. We showed that the change requires both O_2 and light, and a plot of the amount of the dithiophenol present as a function of the number of ultra-violet photons for a pyridine solution of CdSe

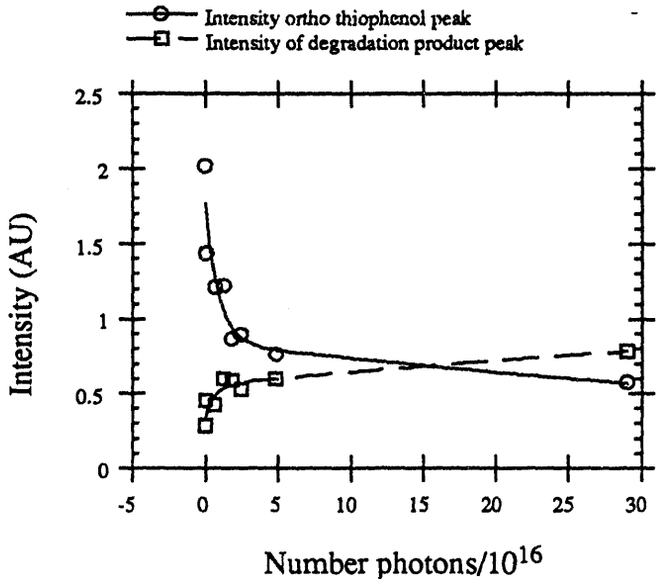

Fig. 2.2.3: Intensity of the ortho selenophenol peak and the degradation product peak at 8.34 ppm in the 1H NMR spectrum as a function of the number of ultra-violet photons (λ=530 nm) to which the sample of Selenophenol capped CdSe nanocrystals was exposed. Degradation of this sample is seen to form the same type of product as the CdS nanocrystals.

nanocrystals that has been saturated with O_2 is presented in figure 2.2.3. Robert and Russ showed that if the O_2 is excluded from the NMR tube, no reaction occurs independent of the number of UV photons exposed to the nanocrystals. Thus, samples can be kept indefinitely in sealed tubes when oxygen is removed by the freeze-pump-thaw method.

Figure 2.2.4 shows a size dependent series of spectra to which a known amount of CH_2Cl_2 was added. The intensity of the thiophenol peaks falls rapidly as the nanocrystal radius is increased. Using these spectra, we are able to determine the number of thiophenol capping molecules per nanocrystal, and the percent coverage by comparing the integrated thiophenol signal to that of a standard present at known concentration (Figure 2.2.5 and

Figure 2.2.4: Intensity calibrated, size-dependent ^1H spectra of thiophenol capped CdS nanocrystals. The samples were made from the same stock solution of d_5-pyridine to which had been added 0.9 mmoles of CH_2Cl_2 per kilogram of solution. The intensity of the CH_2Cl_2 at 5.68 ppm is constant in these spectra.

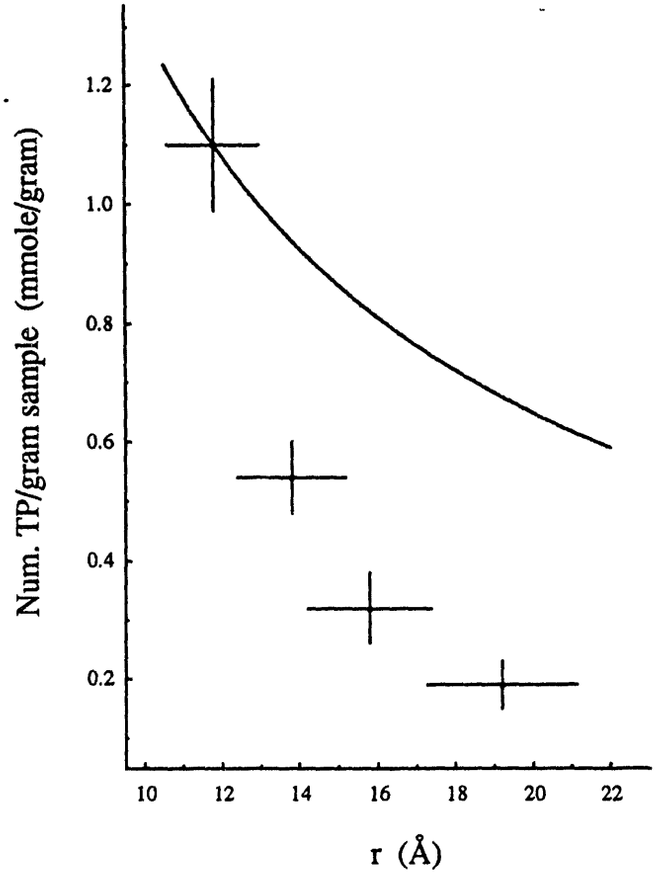

Fig. 2.2.5 Number of thiophenol molecules per gram of nanocrystal versus radius. Notice that the data do not follow the expected 1/r dependence given by the solid line.

Table 2.2.1). In the table, the number of surface Cd atoms was determined for the thiophenol coverage calculation from the shell model of Lippens and Lannoo.[10] This model builds a nanocrystal by tetrahedrally binding atoms in shells starting from a single central atom and predicts the number of atoms N in a particle with a given number of shells n_s to be

$$N = \tfrac{1}{12}(10n_s^3 - 15n_s^2 + 26n_s - 9) \text{ for odd } n_s, \qquad \text{(eq. 2.2.1)}$$

$$N = \tfrac{1}{12}(10n_s^3 - 15n_s^2 + 26n_s - 12) \text{ for even } n_s. \qquad \text{(eq. 2.2.2)}$$

This model is consistent with the nanocrystal preparation, which was performed with the addition of excess Cd at the end of the synthesis in order to create a Cd rich surface. The nanocrystal radius is calculated assuming a spherical nanocrystal. Where the lattice constant of the unit cell is a, the radius is given by

$$r = \frac{a}{2}\sqrt[3]{\frac{3N}{4\pi}}. \qquad \text{(eq. 2.2.3)}$$

With these formulae, we can estimate an upper limit for the number of Cd atoms in the nanocrystal surface. The NMR data can then be used to provide a lower limit for the

Radius (Å)[b]	Molecular Wt (kDa)[c]	Actual No. T.P./part	No. Cd on Surface[d]	% Coverage of T.P.	Effective T.P. radius (Å)[e]	T_2 of T.P *para* peak (msec)[f]
11.8±1.0	23±6	24±6	92	26	9±1	57±3
13.8±1.0	34±7	18±4	162	11	12±2	76±3
15.8±1.0	50±10	16±5	204	7.8	14±2	121±3
19.2±1.0	89±14	17±5	304	5.6	16±2	220±3

Table 2.2.1: Experimental measure of the coverage of thiophenol on CdS nanocrystals[a] as a function of nanocrystal radius.[b]

a. Determined by integration of the spectra presented in Figure 2.2.4. b. The radius of the nanocrystal, excluding the capping group using UV-VIS spectroscopy and graphs in Lippens and Lannoo.[10] *c. Assuming the nanocrystal is spherical. This molecular weight is a lower limit. d. Based on Lippens and Lannoo and assuming completed shells.*[10] *This coverage is a lower limit. e. Note that the Van der Waals radius of thiophenol is 2.1Å if bound in a bridging fashion and is 4.9 Å if bound in a terminal fashion. f. T_2 was measured by the method of Emsley, Kowalewski, and Bodenhausen.*[11]

thiophenol coverage (Table 2.2.1). *This percent coverage increases with decreasing nanocrystal radius*. The data show that the coverage increases from 5.6 to 26 percent as the nanocrystal radius changes from 19.2 Å to 11.8 Å (Table 1). Thus, the nanocrystal is not completely capped. It is of considerable interest to determine whether, at low coverage, the thiophenol molecules are uniformly dispersed on the nanocrystal surface, or if there are substantial local fluctuations in the coverage. If the thiophenol coverage were uniform, the average distance from one surface molecule to another would change from 18Å to 32Å. Such large separations would indicate that there should be negligible interaction between thiophenol molecules.

In figure 2.2.6, the concentration of pyridine per gram of particles is plotted versus the nanocrystal radius. These data show no correlation between the amount of pyridine and the nanocrystal radius. The pyridine resonances disappear upon repeated evaporation and resuspension in deuterated solvent. However, the pyridine resonances do not disappear when powders of nanocrystals are placed under vacuum at room temperature. These data

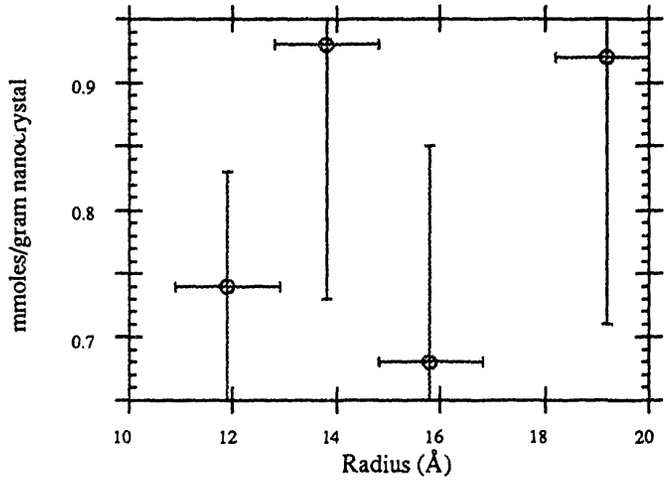

Fig: 2.2.6: Pyridine concentration per gram of nanocrystal versus nanocrystal radius. Data obtained from the integrals of the intensity calibrated spectra shown in figure 2.2.4. Notice that there is no trend in the data.

suggest that the pyridine is not specifically attached to the nanocrystal surface, but merely trapped in the powder; however, we cannot determine if some proportion of the pyridine does associate with the nanocrystal surface, as would be suggested by the low thiophenol coverage.

Perhaps the most remarkable feature of figure 2.2.4 is the size dependence of the linewidths of the thiophenol peaks. As the nanocrystals become smaller, the resonances broaden. This broadening could be either homogeneous as a result of changes in the mechanism of motional narrowing of the lines, or inhomogeneous and due to site variations on the nanocrystal surface. We investigated the source of the broadening by measuring the ^{1}H and ^{13}C longitudinal and transverse relaxation times of the thiophenol ligands. The necessary techniques and the results of these experiments will be discussed in the next sections.

Section 2.3: ^{1}H Longitudinal and Transverse Relaxation Time Measurements of Thiophenol Capped Nanocrystals

To determine the homogeneous linewidth of the ^{1}H resonances of thiophenol on the CdS nanocrystal surface, we measured the transverse relaxation time, T_2, by the selective Hahn echo technique.[11] This relaxation time is related to the homogeneous linewidth by

$$\Delta\nu = \frac{1}{\pi T_2}, \qquad \text{(eq. 2.3.1)}$$

where $\Delta\nu$ is the full width at half the maximum intensity. If the linewidth determined by relaxation time is about the same as the observed linewidth, the line is homogeneously broadened and we must find a mechanism to explain the linewidth. However, if the relaxation time measurement indicates that the homogeneous linewidth is much less than the

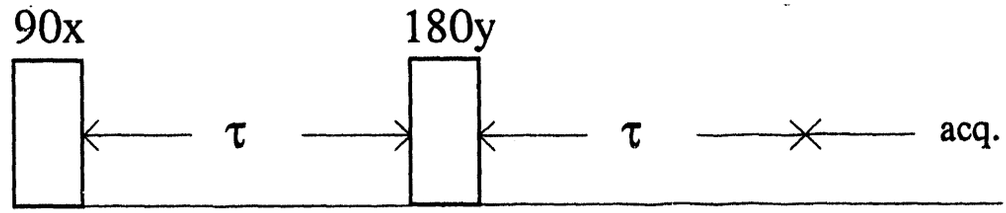

Fig. 2.3.1: The Hahn echo sequence consists of a 90x and 180y pulses separated by a time τ. The chemical shifts refocus at 2τ at which time signal acquisition can begin.

observed linewidth, the line must be broadened inhomogeneously, say by a distribution of sites on the nanocrystal surface.

To measure the transverse relaxation time in this system, a selective experiment must be performed to remove the effects of J-couplings[12]. For example, let us assume that we have two J-coupled spins, I and S, and that we perform a nonselective Hahn echo on this system. The Hahn echo sequence[13-15] is shown in figure 2.3.1. In the rotating frame, the Hamiltonian for this system is

$$H = \omega_I I_Z + \omega_S S_Z + 2\pi J_{IS} I_Z S_Z. \qquad \text{(eq. 2.3.2)}$$

The zeroth order Average Hamiltonian can be found by using equation 1.3.7 of section 1.3 of this thesis. During the first free precession period, the Hamiltonian acting on the spins, H_1, is eq. 2.3.2. After the π pulse, this Hamiltonian is rotated and becomes

$$H_2 = -\omega_I I_Z - \omega_S S_Z + 2\pi J_{IS} I_Z S_Z. \qquad \text{(eq. 2.3.3)}$$

The Average Hamitonian to zeroth order is

$$\overline{H}^{(0)} = \tfrac{1}{t_1+t_2}\left(H_1 t_1 + H_2 t_2\right) = 2\pi J_{IS} I_Z S_Z, \qquad \text{(eq. 2.3.4)}$$

and the intensity of the echo is modulated by the J-coupling. If many J-couplings are present, the echo modulations become too complicated to interpret. In the case of a Hahn echo, the zeroth order average Hamiltonian is equivalent to the exact result.

These echo modulations can be removed by performing a selective Hahn echo. By a selective Hahn echo, we mean that only a single multiplet due to a single spin is affected by the pulses. For the two spin case, where we selectively excite only the I spin, the Hamiltonian during the first time period is again given by equation 2.3.2. After the selective π pulse, the Hamiltonian during the second time period is

$$H_2 = -\omega_I I_Z + \omega_S S_Z - 2\pi J_{IS} I_Z S_Z. \qquad \text{(eq. 2.3.5)}$$

The zeroth order Average Hamiltonian is

$$\overline{H}^{(0)} = \omega_S S_Z. \qquad \text{(eq. 2.3.6)}$$

This Average Hamiltonian does not effect the I spin, so the echo amplitude evolves only because of the transverse relaxation. By using this method, it is easy to obtain an accurate measure of the transverse relaxation time.

To perform the selective Hahn echo experiment, good selective pulses are needed. Emsley and Bodenhausen have found shaped pulses that give good selective excitation without phase problems. They have shown that a gaussian 270° pulse can have a narrow excitation bandwidth with good in phase response[16]. Inversion can be achieved by using a pulse made of three gaussians of different widths and amplitudes that causes almost "tophat" like inversion. They have called this pulse a q^3 pulse[17]. By using these pulses in a Hahn echo sequence[11], they can accurately measure transverse relaxation times and distinguish slightly different relaxation rates.

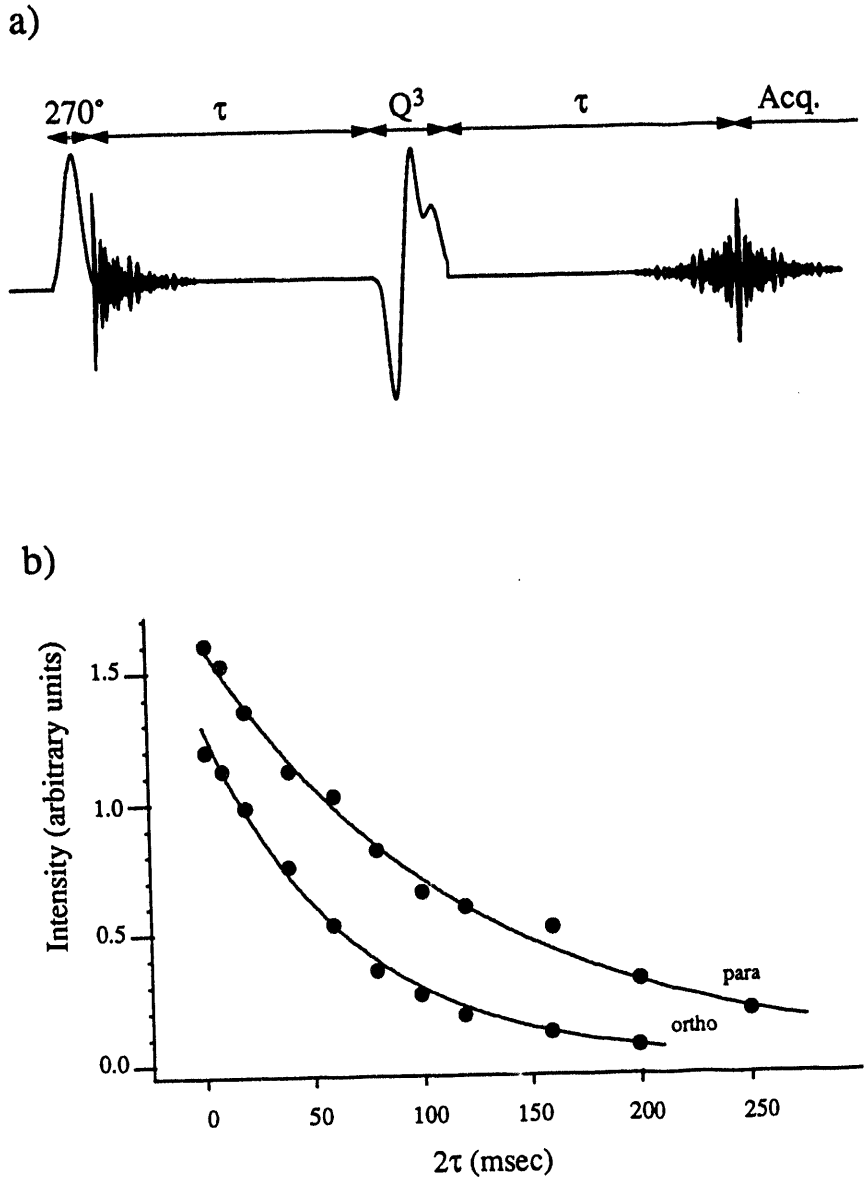

Fig 2.3.2: The Selective T_2 experiment of Emsley, Kowalewski, and Bodenhausen: a.. The pulse sequence. b. Representative data from the ortho and para protons of the thiophenol ligands on CdS nanocrystals.

We have used this selective T_2 sequence to measure the homogeneous proton linewidths of the thiophenol molecules bound to the nanocrystal surface. Figure 2.3.2 shows the selective T_2 pulse sequence of Emsley, Kowalewski, and Bodenhausen[11] that

a.)

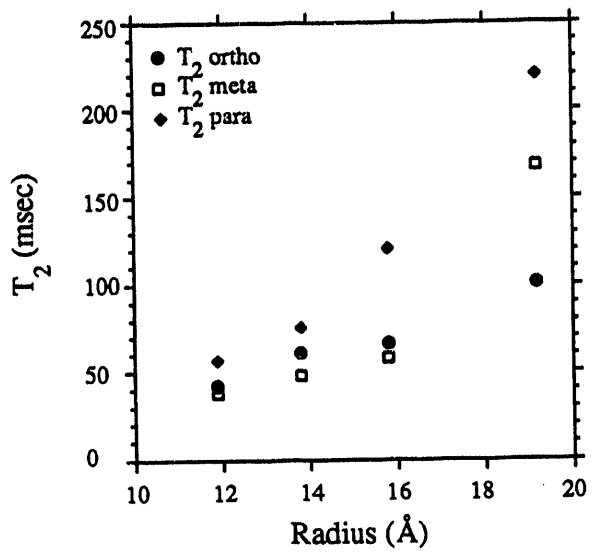

b.)

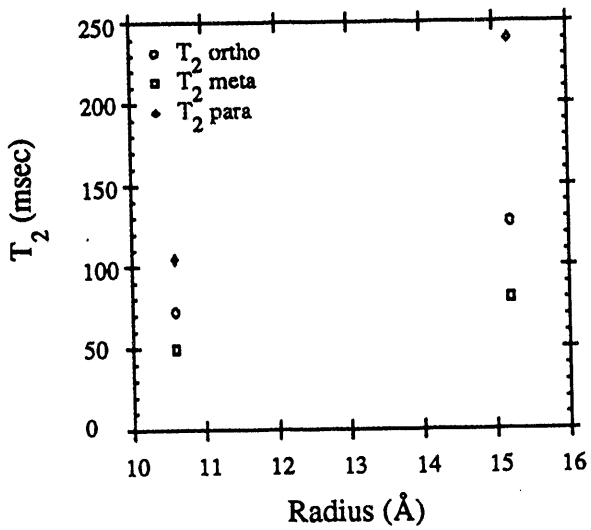

Fig. 2.3.3: T_2 as a function of CdS nanocrystal radius. T_2 was measured using the selective T_2 sequence shown in figure 2.3.2. a.) T_2 measured on sampled prepared by dissolving 5 mg of nanocrystals in 0.5 ml of d5-pyridine. By the time the meta peak of the r=19.2 Å nanocrystal was measured, significant decomposition of the surface had occurred as evidenced by the appearance of peaks due to the dithiophenol decomposition product. b.) Samples prepared at the same concentrations as in a), but the samples were purged of O_2 by repeating the freeze-pump-thaw procedure five times. This had the benefit of both preventing decomposition of the nanocrystals and removing random field relaxation due to dissolved O_2. The removal of random field effects explains the increase in T_2 of the particles in b over what they were measured in a.

was used to make the measurements, together with some representative T_2 data. The resulting transverse relaxation times (given for the *para* peak in Table 1) fully account for the trend in the linewidth, demonstrating that the lines are in fact homogeneously broadened. Therefore, the changes in linewidth must be due to motional averaging effects. The simplest model assumes that the entire nanocrystal undergoes isotropic rotational diffusion as described by the Stokes-Einstein equation while the thiophenol ligands remain fixed with respect to the nanocrystal surface. This predicts that as the particle size increases from 11.8 to 19.2 Å, the correlation time for reorientation of the entire nanocrystal increases from 1.7 to 7.1 ns, and that the transverse relaxation times should correspondingly decrease with increasing nanocrystal radius. If only *intra*-thiophenol dipole-dipole interactions are considered, this theory predicts that $T_2^{para}=T_2^{meta}=\frac{1}{2}T_2^{ortho}$. Neither of these predictions is borne out in our experimental data, presented in figure 2.3.3.

Figure 2.3.4 shows the ^1H longitudinal relaxation times, T_1, of the thiophenol ligands. The data for the nondegassed samples possibly suggest that the 13.8Å nanocrystals are near the T_1 minimum. However, the degassed samples show that T_1 monotonically increases with nanocrystal radius, indicating that the nanocrystals are tumbling in the slow motion regime. This would be expected for particles whose overall tumbling time is 1.7 to 7.1 ns in a 400 MHz magnetic field; therefore, the possible T_1 minimum observed in the nondegassed samples must be an experimental error. Notice that the longitudinal relaxation times of the different sites in the thiophenol molecules in the gassed and degassed samples occur in a different order. In the nondegassed samples, $T_{1ortho}>T_{1meta}>T_{1para}$ while in the degassed samples, $T_{1para}>T_{1meta}>T_{1ortho}$. These data suggest that in the nondegassed samples, longitudinal relaxation due to random fields created by dissolved oxygen, which has greater exposure to the para ^1H's , is the predominant effect. In the degassed samples, this effect is removed.

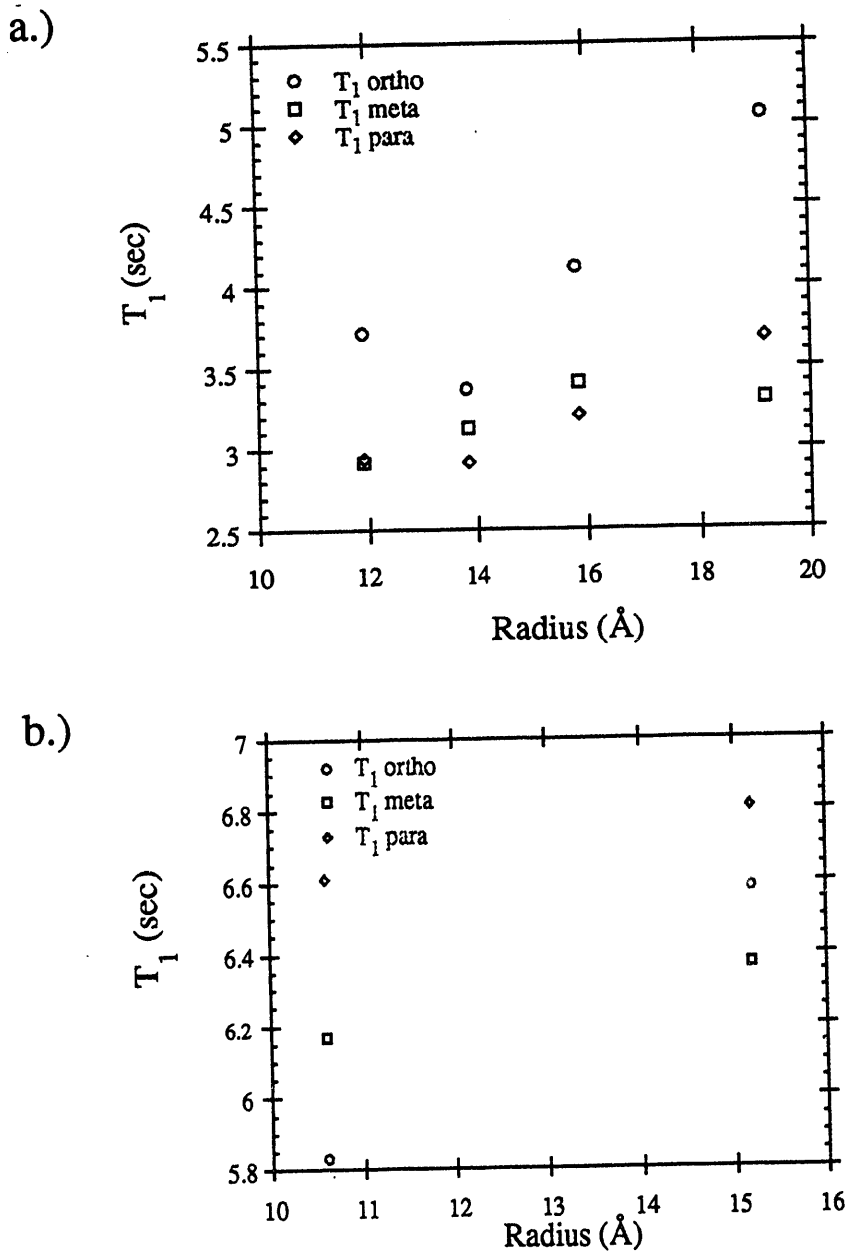

Fig. 2.3.4: ^1H longitudinal relaxation times of thiophenol ligands as a function of nanocrystal radius. T_1 was measured by nonselective inversion recovery of all ^1H resonances. a.) T_1 measured on sampled prepared by dissolving 5 mg of nanocrystals in 0.5 ml of d_5-pyridine. By the time the meta peak of the r=19.2 Å nanocrystal was measured, significant decomposition of the surface had occurred as evidenced by the appearance of peaks due to the dithiophenol decomposition product. b.) Samples prepared at the same concentrations as in a), but the samples were purged of O_2 by repeating the freeze-pump-thaw procedure five times. This had the same benefits as in figure 2.3.3.

Change of ^1H relaxation rate in 10.6Å thiophenol capped CdS nanocrystals.

Peak	T (°C)	T_2 (msec)	$\frac{1}{T_2^{high}} - \frac{1}{T_2^{low}}$
ortho	26.0	72.6	2.0
	79.1	63.4	
meta	26.0	49.8	2.5
	79.1	44.2	
para	26.0	104.9	0.97
	79.1	95.2	

Change of ^1H relaxation rate in 15.2Å thiophenol capped CdS nanocrystals.

Peak	T (°C)	T_2 (msec)	$\frac{1}{T_2^{high}} - \frac{1}{T_2^{low}}$ (sec^{-1})
ortho	25.9	127.0	8.8
	79.3	59.9	
meta	25.9	80.3	10.1
	79.3	44.4	
para	25.9	239.8	7.9
	79.3	83.0	

Table 2.3.1: Change in relaxation rate with temperature.

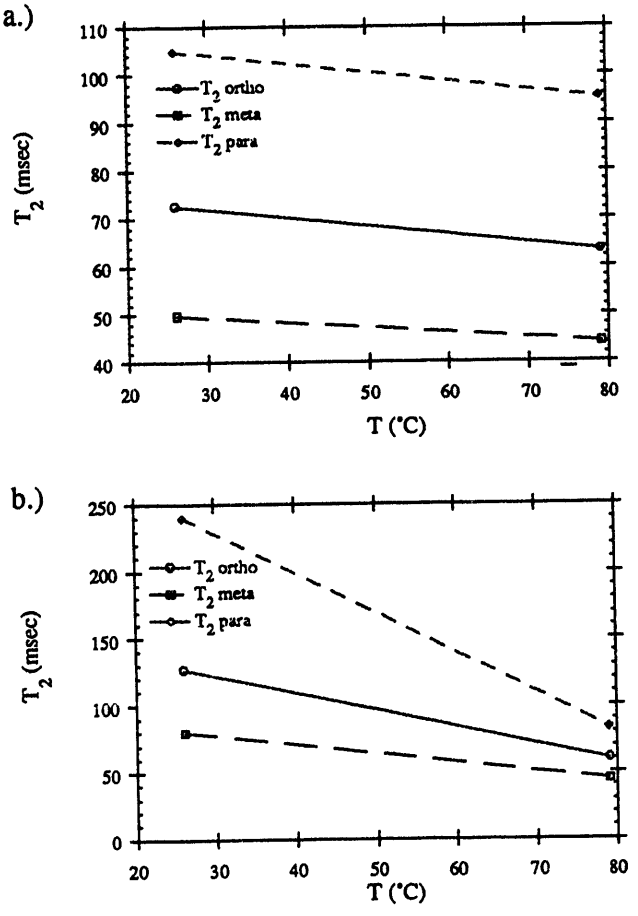

Fig. 2.3.5: Temperature dependence of the ^1H transverse relaxation rates for the thiophenol ligands of CdS nanocrystals. The temperature dependence for two sizes of nanocrystals is presented: a.) r=10.6 Å. b.) r=15.2 Å. These samples were prepared by dissolving 5 mg of nanocrystal powder in 0.5 ml of d_5-pyridine and then purging the samples of O_2 by repeating the freeze-pump-thaw procedure five times and flame sealing the NMR tubes.

The temperature dependence of the T_2 data was measured, and is presented in figure 2.3.5. T_2 decreases as the temperature is raised. This trend is unexpected, because the correlation time of the motion of the nanocrystal should decrease with temperature and lengthen the T_2 . Table 2.3.1 presents the difference in the high and low temperature rates for the two particle sizes. For a nanocrystal of a given size, the relaxation rates of the different sites on the thiophenol ligand change by an amount that is the same to within the

error of the measurement. This result implies that the mechanism responsible for the decrease in the relaxation time does not distinguish between the different locations on the thiophenol ligand.

To obtain more information about the relaxation behavior of the thiophenol molecules, we performed ^{13}C relaxation measurements. These experiments are presented in the next section.

Section 2.4: ^{13}C T_1 and T_2 Measurements of Thiophenol Capped Nanocrystals

In order to obtain more information about the relaxation mechanisms in the thiophenol ligands of the CdS nanocrystals, we performed ^{13}C longitudinal, T_1, and transverse, T_2, relaxation measurements. ^{13}C dipole-dipole relaxation depends only upon the motion of the ^{13}C -^{1}H vector to those H atoms directly covalently bound to the carbon atom. Thus, this relaxation process is only sensitive to the motions of a single thiophenol and is totally unaffected by neighboring thiophenols.

However, despite the advantage ^{13}C relaxation measurements have for interpretation of the data, they are difficult experiments to perform because of the sensitivity problems of ^{13}C. The simplest, but expensive, solution to this sensitivity problem is isotopic enrichment of the sample with ^{13}C. This is not a possible solution in the case of the thiophenol nanocrystals because of the lack of availability of ^{13}C labeled thiophenol. Thus, we had to measure the ^{13}C spectra without enrichment. Unfortunately, direct measurement of the spectrum by the simple pulse-acquire method never produced a thiophenol spectrum because the d_5-pyridine solvent signal totally dominated the spectrum. Because of these problems, the ^{13}C spectra were indirectly detected via the thiophenol protons by using the double INEPT experiment[18-23] shown in figure 2.4.1. This sequence transfers magnetization from the ^{1}H to the ^{13}C via the antiphase coherence formed in

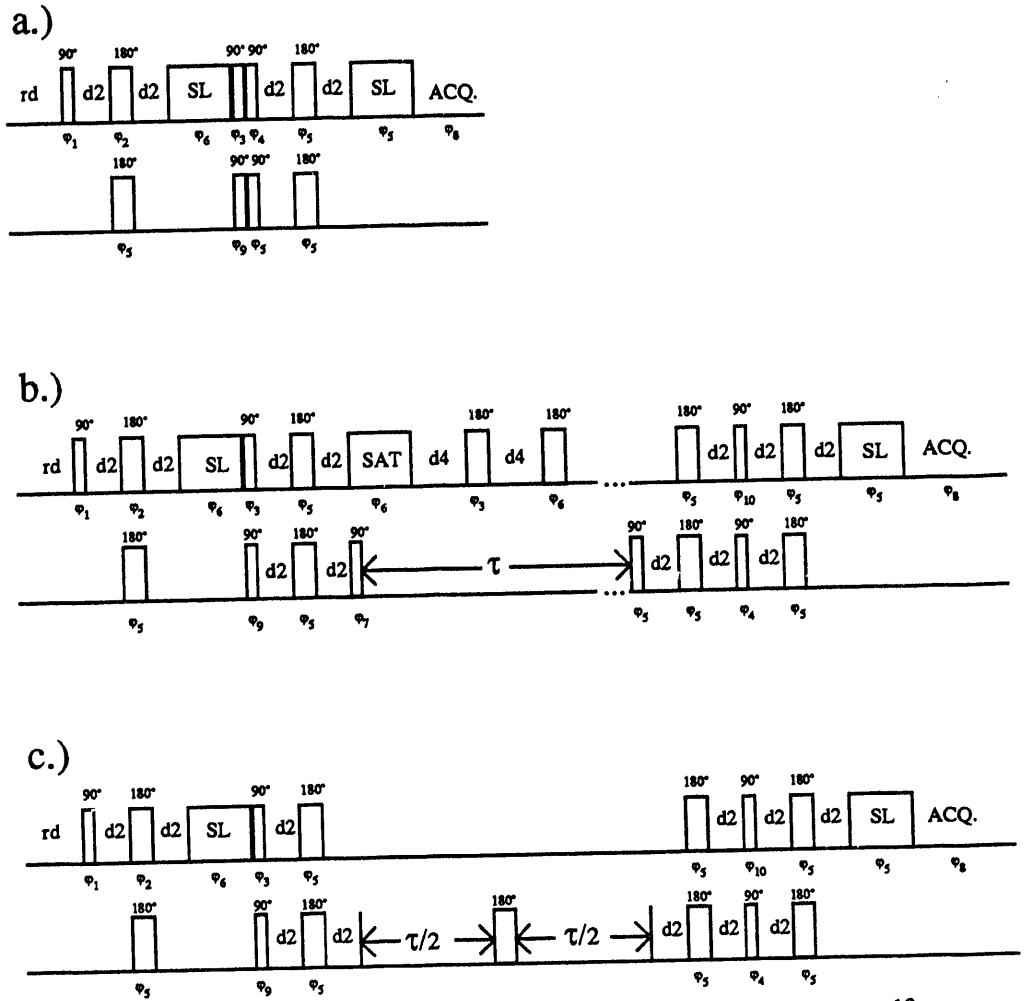

Fig. 2.4.1: The double INEPT experiments used in this section to observe the ^{13}C resonances of the thiophenol ligands of CdS nanocrystals. In the sequences shown, rd is the recycle delay, d2 is set to $1/(4J_{HC})$ and allows build up of ^{1}H-^{13}C antiphase coherence, and the two pulses labeled SL are spin lock pulses to remove residual proton coherence. In the experiments described in this section, rd=20sec, d2=1.5 msec, and the two spin lock pulses equaled 4 msec and 1 msec, respectively. The phases used in these sequences are given in table 4.2.1. a.) The double INEPT experiment used to observe the proton detected ^{13}C spectrum shown in figure 2.4.2. b.) The double INEPT T_1 experiment used to measure the ^{13}C longitudinal relaxation time, T_1. The pulse labeled SAT was used to saturate the ^{1}H resonances which were kept saturated by the repeated 180° pulses every d4 sec. The saturation pulse length was 0.5 msec and the 180° degree pulses were applied every 0.5 msec for the measurements on the CdS nanocrystals. c.) The double INEPT T_2 experiment used to measure the ^{13}C transverse relaxation time, T_2.

Phases for the double INEPT sequence shown in figure 2.4.1.a.

φ_1	$xy\bar{x}\bar{y}\bar{x}\bar{y}xy$
φ_2	$xy\bar{x}\bar{y}xy\bar{x}\bar{y}y\bar{x}\bar{y}xy\bar{x}\bar{y}x$
φ_3	$y\bar{x}\bar{y}x$
φ_4	$xxxxxxxxxxxxxxxxxxxxxxxxxxxxxxxx$ $\bar{x}$
φ_5	x
φ_6	$xy\bar{x}\bar{y}$
φ_8	$xxxx\bar{x}\bar{x}\bar{x}\bar{x}\bar{x}\bar{x}\bar{x}\bar{x}xxxx\bar{x}\bar{x}\bar{x}\bar{x}xxxxxxxx\bar{x}\bar{x}\bar{x}\bar{x}$ $\bar{x}\bar{x}\bar{x}\bar{x}xxxxxxxx\bar{x}\bar{x}\bar{x}\bar{x}xxxx\bar{x}\bar{x}\bar{x}\bar{x}\bar{x}\bar{x}\bar{x}\bar{x}xxxx$
φ_9	$xxxxxxxxxxxxxxxx\bar{x}\bar{x}\bar{x}\bar{x}\bar{x}\bar{x}\bar{x}\bar{x}\bar{x}\bar{x}\bar{x}\bar{x}\bar{x}\bar{x}\bar{x}\bar{x}$

Phases for the double INEPT T_1 and T_2 experiments shown in figure 2.4.1.b and .c.

φ_1	$xy\bar{x}\bar{y}\bar{x}\bar{y}xy$
φ_2	$xy\bar{x}\bar{y}xy\bar{x}\bar{y}y\bar{x}\bar{y}xy\bar{x}\bar{y}x$
φ_3	$y\bar{x}\bar{y}x$
φ_4	x
φ_5	y
φ_6	$xy\bar{x}\bar{y}$
φ_7	$yyyyyyyyyyyyyyyyyyyyyyyyyyyyyyyy$ $\bar{y}$
φ_8	$xxxx\bar{x}\bar{x}\bar{x}\bar{x}\bar{x}\bar{x}\bar{x}\bar{x}xxxx\bar{x}\bar{x}\bar{x}\bar{x}xxxxxxxx\bar{x}\bar{x}\bar{x}\bar{x}$ $\bar{x}\bar{x}\bar{x}\bar{x}xxxxxxxx\bar{x}\bar{x}\bar{x}\bar{x}xxxx\bar{x}\bar{x}\bar{x}\bar{x}\bar{x}\bar{x}\bar{x}\bar{x}xxxx$ $\bar{x}\bar{x}\bar{x}\bar{x}xxxxxxxx\bar{x}\bar{x}\bar{x}\bar{x}xxxx\bar{x}\bar{x}\bar{x}\bar{x}\bar{x}\bar{x}\bar{x}\bar{x}xxxx$ $xxxx\bar{x}\bar{x}\bar{x}\bar{x}\bar{x}\bar{x}\bar{x}\bar{x}xxxx\bar{x}\bar{x}\bar{x}\bar{x}xxxxxxxx\bar{x}\bar{x}\bar{x}\bar{x}$
φ_9	$xxxxxxxxxxxxxxxx\bar{x}\bar{x}\bar{x}\bar{x}\bar{x}\bar{x}\bar{x}\bar{x}\bar{x}\bar{x}\bar{x}\bar{x}\bar{x}\bar{x}\bar{x}\bar{x}$
φ_{10}	$xxxxxxxxxxxxxxxxxxxxxxxxxxxxxxxx$ $xxxxxxxxxxxxxxxxxxxxxxxxxxxxxxxx$ $\bar{x}$ $\bar{x}$

Table 4.2.1: Phase Table for the Double INEPT experiments shown in figure 2.4.1.

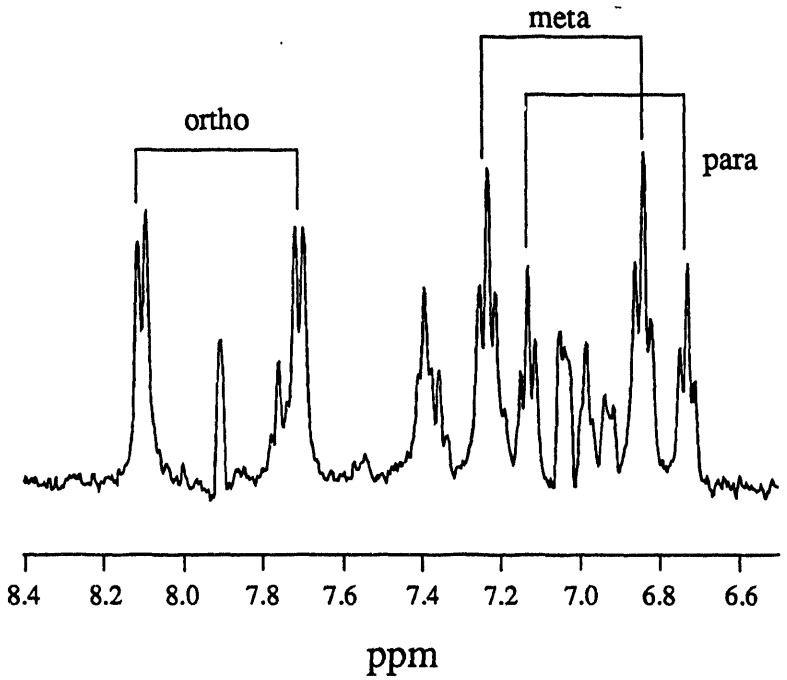

Fig. 2.4.2: ^{1}H detected ^{13}C spectrum of an r=15.8 Å nanocrystal. The double INEPT sequence shown in part a of figure 2.4.1 a was used. The sample was prepared by dissolving 5 mg of nanocrystal in 0.5 ml of d_5-pyridine and then freeze-pump-thawing the sample and flame sealing the sample. The recycle delay in this experiment was 10 sec. The ^{1}H 90° pulse length was 4.8 μsec, the ^{13}C 90° pulse length was 10.0 μsec, the first spin-lock length was 1 msec, and the second was 4 msec. The delay d2 was 1.5625 msec. This spectrum was obtained in 512 scans and was apodized before fourier transformation with an exponential filter of 2 Hz.

response to the heteronuclear J-coupling. Such an inverse detected spectrum is shown in figure 2.4.2. In this spectrum, each multiplet of the proton spectrum is split into a doublet by the large, approximately 160 Hz, ^{1}H-^{13}C J-coupling. The artifacts between the doublets are due to incomplete suppression of the ^{1}H signal not coupled to a ^{13}C.

The double INEPT inversion recovery and Hahn echo sequences used to measure the ^{13}C longitudinal and transverse relaxation times are also shown in figure 2.4.1. These sequences are the double INEPT sequence with a inversion recovery or Hahn echo sequence inserted. In the inversion recovery sequence, proton saturation is performed while the carbon magnetization is inverted in order that simple monoexponential decays are

observed, as discussed at the end of section 1.10 of this thesis. Representative data from these sequences are shown in figure 2.4.3. The signal to noise in these data are not nearly as good as in the proton spectra measured in section 2.3, but they are good enough to give us a reasonable measure, ±15%, of the relaxation times.

Figure 2.4.4 shows the ^{13}C longitudinal relaxation time, T_1, as a function of nanocrystal radius. The measured relaxation times are very similar for different synthetic

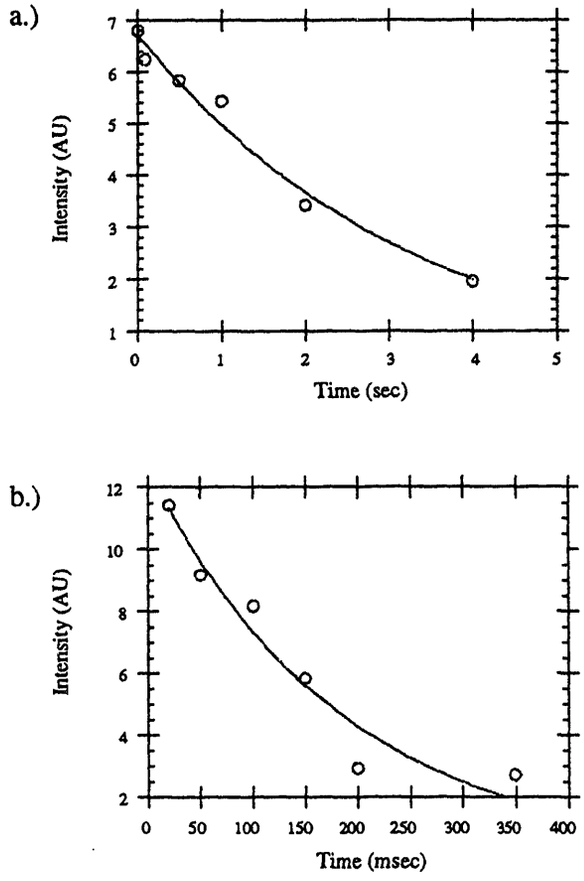

Fig. 2.4.3: Representative ^{13}C T1 and T_2 data of the thiophenol ligands of CdS nanocrystals taken with the double INEPT T_1 and T_2 sequences. a.) T_1 data for the para thiophenol carbon on a 15.8Å radius nanocrystal. b.) T_2 data for the para thiophenol carbon on a 15.8Å radius nanocrystal. The experiment time for both of these data sets was approximately 12 hours. The intensity is the sum of the integrated area of the two members of the doublet seen in the proton detected carbon spectrum.

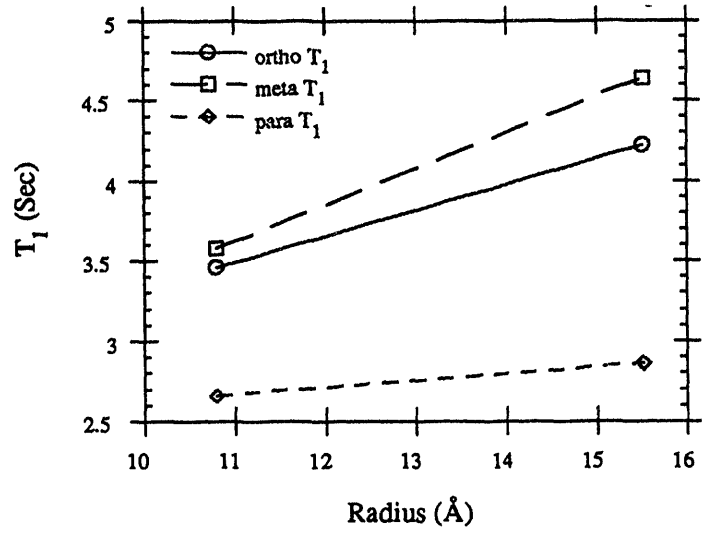

Fig. 2.4.4: ^{13}C longitudinal relaxation times, T_1, as a function of particle radius. These relaxation times were measured using the double INEPT T_1 experiment shown in figure 2.4.1. The relaxation times presented in this figure is average data from two different batches of nanocrystals per size whose radii were within 0.4Å of each other.

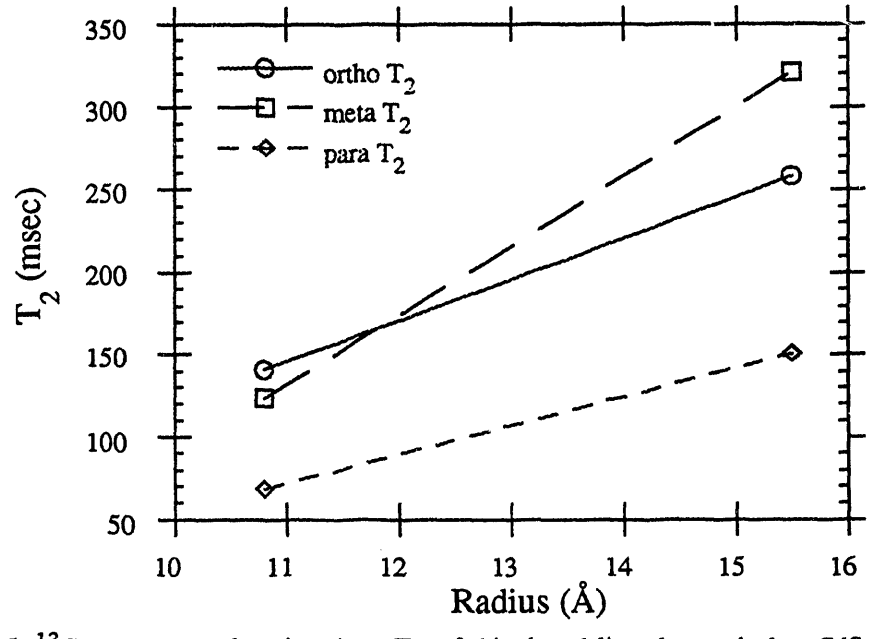

Fig. 2.4.5: ^{13}C transverse relaxation time, T_2, of thiophenol ligands attached to CdS nanocrystals. The relaxation times at 15.5Å is averaged over two different synthetic batches.

batches, so the data were averaged over different batches with approximately the same radius. Since the relaxation times were not dependent upon which synthetic batch was observed, we can compare the relaxation times of different sized nanocrystals without considering that the effects we are seeing are a result of inconsistencies in the synthesis procedure. These data show that the T_1 increases as the particles get larger, implying that the particles are randomly tumbling at a rate on the slow motion side of the T_1 minimum as one would expect from a particle of this size. This result is consistent with the ^1H T_1's measured before on the degassed samples and it shows that the possible T_1 minimum observed in the other experiment is not a real effect.

Figure 2.4.5 shows the ^{13}C transverse relaxation time, T_2, as a function of the nanocrystal radius. These transverse relaxation times follow the same trend as seen in the ^1H transverse relaxation data presented in section 2.3. The relaxation times become longer as the particle radius increases. As for the previously measured proton relaxation times, these data cannot be explained by reorientation of the nanocrystal with immobile thiophenol ligands. These data differ from the ^1H data in that the para ^{13}C now has the shortest transverse relaxation time for a given radius of nanocrystal, while the para ^1H had the longest. This suggests that the thiophenol ligands must be rotating about either the C-S or Cd-S bonds, because this rotation would cause averaging of the dipolar coupling in the case the para ^1H and little averaging in the ^{13}C case.

To understand the relaxation mechanism of both the ^1H and the ^{13}C, we must perform explicit calculations of the longitudinal and transverse relaxation rates for both the ^1H data and the ^{13}C data. These explicit calculations will be performed in the next section.

Section 2.5: Motional Models Explored to Explain the ^1H and ^{13}C Relaxation Measurements

In order to understand the relaxation data presented in the previous sections, detailed relaxation calculations must be performed. The equations we will use for calculating T_1 and T_2 are derived from Redfield theory, which was presented in section 1.10 and was there used to derive the T_1 equation. They assume only two spin interactions without J-couplings and are the same as those presented by Szabo[24] with only slight change of the definition of the spectral density. These equations only approximately describe our system and neglect cross-correlation effects. Since all of our experiments were performed selectively and, in all cases, the spins responsible for the relaxation are not degenerate with the spin being relaxed, we must use heteronuclear (I S) relaxation equations given in table 2.5.1. We will neglect the effect of transverse cross relaxation in the ^1H T_2 experiments.

As you can see from the equations in table 2.5.1, we need to calculate the spectral densities,

$$J_m(\omega^r_{I,-m}) = (-1)^m \int_{-\infty}^{\infty} C_m(\tau) e^{i\omega^r_{I,-m}\tau} d\tau, \qquad \text{(eq. 2.5.1)}$$

^1H Dipole-Dipole Relaxation	$T_1^{-1} = C\left[3J(\omega_0) + 12J(2\omega_0)\right]$
	$T_2^{-1} = \frac{1}{2}C\left[5J(0) + 9J(\omega_0) + 6J(2\omega_0)\right]$
^{13}C Dipole-Dipole Relaxation	$T_1^{-1} = C\left[J(\omega_I - \omega_S) + 3J(\omega_I) + 6J(\omega_I + \omega_S)\right]$
	$T_2^{-1} = \frac{1}{2}C[4J(0) + J(\omega_I - \omega_S) + 3J(\omega_I) + 6J(\omega_S)$
	$+6J(\omega_I + \omega_S)]$

Table 2.5.1: Longitudinal and transverse relaxation rates[24] for 1H and 13C dipolar relaxation. The constant C is given by $\frac{1}{4}\gamma_I^2\gamma_S^2 r^{-6}$, where I is the observed spin, S is the spin responsible for the relaxation.

which are the real fourier transform of the correlation function of the molecule under study,

$$C_m(\tau) = \frac{3\pi}{5} C_D^2 \left\langle \frac{Y_{2,m}^L(\Omega_{ij},0) Y_{2,m}^L(\Omega_{ij},t)^*}{r(t)^3 r(t+\tau)^3} \right\rangle. \qquad \text{(eq. 2.5.2)}$$

The $Y_{2,m}^L(\Omega_{ij},t)$ are spherical harmonics with Ω_{ij} being the direction of the internuclear vector in the laboratory frame at time t. In this section, we will hypothesize a model for the motion of the thiophenol molecules and derive the resulting correlation functions and spectral densities. From these results, we will learn about the motions of the thiophenol ligands with respect to the surface.

The crystal structure of the model compounds synthesized by Dance's group[7] show that thiophenol molecules can bond bridging two cadmium atom or terminally to a single cadmium atom. Also, the crystal structure of a single sized small nanocrystal has been obtained[25] and shows that the thiophenols in this sample are bound in a bridging fashion. From these crystallographic results, we based our motional models on bridgingly bound thiophenol molecules. A schematic drawing of this bonding arrangement is shown in figure 2.5.1 along with the definition of the various axis system we will use. The final axis

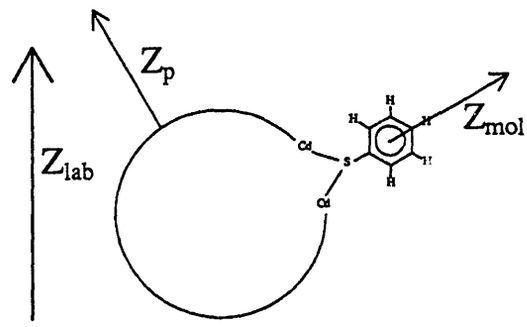

Fig. 2.5.1: Definition of the axis systems used in modeling the relaxation data, assuming that the thiophenol is bound bridging two cadmium atoms. The principle axis system (PAS) is not shown and is given by the vector between the nuclei involved in the relaxation process being investigated.

system we will need is the principle axis system of the dipole-dipole interaction. This system is not explicitly indicated in figure 2.5.1 because it depends upon which nucleus is examined.

The expressions we derive for a bridging thiophenol molecules will apply to both the ^{13}C and ^{1}H cases, except that in the ^{1}H case, we will assume that we can add the effects of multiple spins and, in the ^{13}C case, we assume that only the bound ^{1}H is responsible for the relaxation of the carbon. We need to rotate the spherical harmonics in equation 3.5.2 into the principle axis system (PAS) of the dipole-dipole interaction, so that $Y^{L}_{2,m}(\Omega_{ij},t)$ becomes

$$Y^{L}_{2,q}(\Omega_{ij},t)=\sum_{m,n}Y^{PAS}_{2,0}(\Omega_{PAS})D^{(2)}_{n,m}(\Omega_{mol})D^{(2)}_{m,q}(\Omega_{P}) \qquad \text{(eq. 2.5.3)}$$

where Ω_P are the Euler angles between the lab frame and the axis system defined on the nanocrystal, Ω_{mol} are the angles between the particle defined axis system and the thiophenol defined axis system illustrated in figure 2.5.1, and Ω_{PAS} are the angles between the thiophenol defined axis system and the PAS. The correlation function then becomes

$$C(t)=\tfrac{3\pi}{5}\omega_D^2\sum_{\substack{m,n\\m',n'}}\left\langle D^{(2)}_{m,q}(\Omega_P)D^{(2)}_{m',q'}(\Omega_P')^{*}\right\rangle\left\langle D^{(2)}_{n,m}(\Omega_{mol})D^{(2)}_{n',m'}(\Omega_{mol}')^{*}\right\rangle$$

$$\times Y^{PAS}_{2,0}(\Omega_{PAS})Y^{PAS}_{2,0}(\Omega_{PAS}')^{*}, \qquad \text{(eq. 2.5.4)}$$

where $\omega_D=\frac{C_D}{r^3}$, the unprimed euler angles, Ω, correspond to the angles at time t, the primed angles are the angles at time $t+\tau$, and the angular brackets, $\langle\ \rangle$, indicate that an ensemble average must be performed. In expression 2.5.4, we have assumed that the overall tumbling of the nanocrystal is uncorrelated with the internal rotations of the thiophenol molecules, which allows the separate ensemble averages of the overall tumbling from the internal motions. This assumption implies that the internal correlation time must be

much shorter than the overall correlation time. If the overall tumbling of the nanocrystal is isotropic, its ensemble average has been shown to be

$$\left\langle D^{(2)}_{m,q}(\Omega_P) D^{(2)}_{m',q'}(\Omega_P')^* \right\rangle = \tfrac{1}{5}\delta_{m,m'} e^{-6D_m t}, \qquad \text{(eq. 2.5.5)}$$

where D_m is the rotational diffusion coefficient of the nanocrystal. By using this relation, the explicit form the Wigner rotation matrix,

$$D^{(j)}_{m,m'}(\alpha,\beta,\gamma) = e^{-im'\alpha} d^{(j)}_{m,m'}(\beta) e^{-im\beta}, \qquad \text{(eq. 2.5.6)}$$

and the orthogonality relation of the $d^{(j)}_{m,m'}(\beta)$,

$$\sum_m d^{(j)}_{n,m}(\beta) d^{(j)}_{n',m}(\beta) = \delta_{n,n'}, \qquad \text{(eq. 2.5.7)}$$

the correlation function simplifies to

$$C(t) = \tfrac{3\pi}{25}\omega_D^2 e^{-6D_m t} \sum_n d^{(2)}_{0,n}(\beta_{PAS})^2 \left\langle e^{in(\alpha_{mol}' - \alpha_{mol})} \right\rangle. \qquad \text{(eq. 2.5.8)}$$

As described in section 1.10, the correlation function is real so we can ignore the imaginary part of the expansion of the exponential, so that

$$C(t) = \tfrac{3\pi}{25}\omega_D^2 e^{-6D_m t} \sum_n d^{(2)}_{0,n}(\beta_{PAS})^2 \left\langle \cos\left[n(\alpha_{mol}' - \alpha_{mol})\right] \right\rangle. \qquad \text{(eq. 2.5.9)}$$

To calculate the ensemble average indicated in equation 3.5.9,

$$C_n'(t) = \left\langle \cos\left[n(\alpha_{mol}' - \alpha_{mol})\right] \right\rangle, \qquad \text{(eq. 2.5.10)}$$

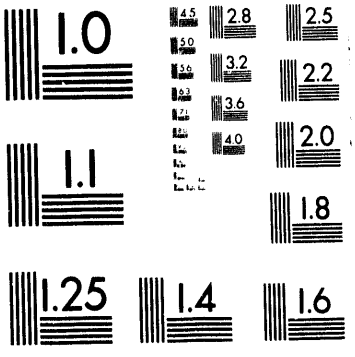
1.0
1.1
1.25
1.4
1.6
1.8
2.0
2.2
2.5
2.8
3.2
3.6
4.0
4.5
5.0
5.6
6.3
7.1
8.0
9.0

2 of 2

we need to evaluate the integral,

$$C_n'(t) = P_{eq} \int_0^{2\pi} \int_0^{2\pi} p(\alpha_{mol}', t|\alpha_{mol}, 0) \cos[n(\alpha_{mol}' - \alpha_{mol})] d\alpha_{mol}' \, d\alpha_{mol}, \qquad \text{(eq. 2.5.11)}$$

where $p(\alpha_{mol}', t|\alpha_{mol}, 0)$ is the conditional probability that a molecule at angle α_{mol} at time 0 will be at α_{mol}' at time t. Models of the motion appear in this theory in terms of these conditional probabilities.

For the bridging case, we have examined four different motional models; rotational diffusion, two site jumps, and six site jumps in both the weak and strong collision limits. To find the condition probability for rotational diffusion, the diffusion equation,

$$\frac{\partial p(\alpha', t|\alpha, 0)}{\partial t} = D_{\text{int}} \frac{\partial^2 p(\alpha', t|\alpha, 0)}{\partial \alpha^2}, \qquad \text{(eq. 2.5.12)}$$

must be solved with the delta function initial condition,

$$p(\alpha', 0|\alpha, 0) = \delta(\alpha' - \alpha), \qquad \text{(eq. 2.5.13)}$$

and periodic boundary conditions,

$$p(0, t|0, 0) = p(2\pi, t|0, 0). \qquad \text{(eq. 2.5.14)}$$

The periodic boundary conditions implies a Fourier series expansion of the solution,

$$p(\alpha', t|\alpha, 0) = 2 \sum_{m=0}^{\infty} C_m(t) \cos[m(\alpha' - \alpha)], \qquad \text{(eq. 2.5.15)}$$

which can be substituted into the differential equation to produce

$$\sum_{m=0}^{\infty}\frac{\partial C_m(t)}{\partial t}\cos[m(\alpha'-\alpha)]=-D_{\text{int}}\sum_{m=0}^{\infty}m^2C_m(t)\cos[m(\alpha'-\alpha)]. \qquad \text{(eq. 2.5.16)}$$

This new equation gives us an infinite number of differential equations, one for each $C_m(t)$. If $m=0$, then $\frac{\partial C_0(t)}{\partial t}=0$, which implies that $C_0(t)$=constant. For $m\neq 0$, we find that

$$\frac{\partial C_m(t)}{\partial t}=-D_{\text{int}}m^2C_m(t), \qquad \text{(eq. 2.5.17)}$$

which can be integrated to give

$$C_m(t)=C_m(0)e^{-D_{\text{int}}m^2t}. \qquad \text{(eq. 2.5.18)}$$

The $C_m(0)$ are given by

$$C_m(0)=\tfrac{1}{\pi}\int_{-\pi}^{\pi}\delta(\theta)\cos(m\theta)d\theta=\tfrac{1}{\pi}, \qquad \text{(eq. 2.5.19)}$$

for all m. Thus, we find for rotational diffusion that the conditional probability is

$$p(\alpha',t|\alpha,0)=\tfrac{2}{\pi}\sum_{m=0}^{\infty}e^{-D_{\text{int}}m^2t}\cos[m(\alpha'-\alpha)], \qquad \text{(eq. 2.5.20)}$$

which can be simplified to

$$p(\alpha',t|\alpha,0)=\tfrac{2}{\pi}\left[1+e^{-D_{\text{int}}t}\cos(\alpha'-\alpha)\right] \qquad \text{(eq. 2.5.21)}$$

in the long time limit.

With this conditional probability, we can find the ensemble average in equation 3.5.11 for thiophenol molecules undergoing rotational diffusion,

$$C_n'(t) = \frac{2}{\pi} P_{eq} \int_0^{2\pi} \int_0^{2\pi} \left[1 + e^{-D_{int} t} \cos(\alpha' - \alpha)\right] \cos\left[n(\alpha_{mol}' - \alpha_{mol})\right] d\alpha_{mol}' \, d\alpha_{mol}$$

$$= \begin{cases} 2\pi & \text{for } m = 0 \\ \pi e^{-D_{int} t} & \text{for } m = \pm 1, \\ 0 & \text{for } m = \pm 2 \end{cases} \qquad \text{(eq. 2.5.22)}$$

where we have used $P_{eq} = \frac{1}{2\pi}$. Combining equations 3.5.1, 3.5.9 and 3.5.22, we can

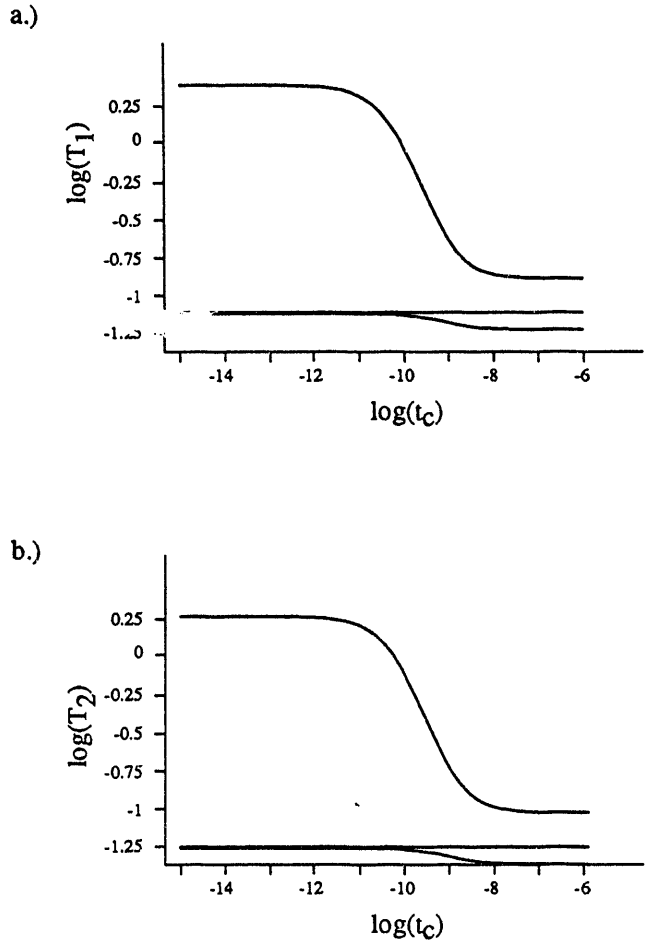

Fig. 2.5.2: Simulations of the ^1H T_1 and T_2 versus the C-S rotational correlation time , tc, assuming that the thiophenol is bridgingly bound and undergoing rotational diffusion about this bond. The overall rotational correlation time was assumed to be 10 nsec. a.) $\log(T_1)$ versus $\log(tc)$. b.) $\log(T_2)$ versus $\log(tc)$.

finally arrive at the spectral density for bridging thiophenol molecules undergoing rotational diffusion,

$$J(\omega) = \frac{12\pi^2}{25}\omega_D^2\left\{d_{0,0}^{(2)}(\beta_{PAS})^2\frac{6D_m}{(6D_m)^2+\omega^2} + d_{1,0}^{(2)}(\beta_{PAS})^2\frac{6D_m + D_{\text{int}}}{(6D_m + D_{\text{int}})^2+\omega^2}\right\}. \quad \text{(eq 2.5.23)}$$

We used this two spin spectral density to calculate the ^1H and ^{13}C relaxation rates of the thiophenol ligands of the CdS nanocrystals. The results of the ^1H calculations are shown in figure 2.5.2 and the ^{13}C calculations are shown in figure 2.5.3. Notice that this calculation can only predict our relaxation data if the internal rotation rate is slow, ~10^{-8} sec. In this

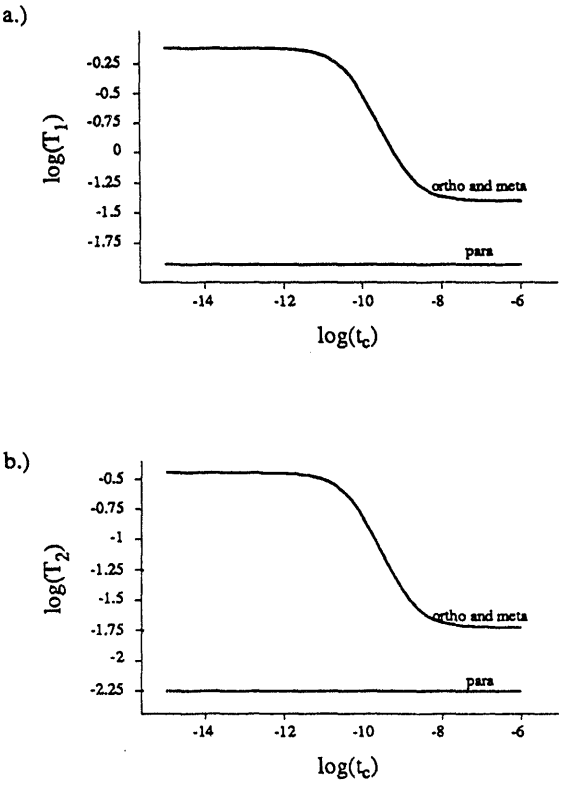

Fig. 2.5.3: Simulations of the ^{13}C T_1 and T_2 versus the C-S rotational correlation time , tc, assuming that the thiophenol is bridgingly bound and undergoing rotational diffusion about this bond. The overall rotational correlation time was assumed to be 10 nsec. a.) log(T_1) versus log(tc). b.) log(T_2) versus log(tc).

time regime the assumption of no correlation between the overall tumbling and the internal reorientation is becoming invalid. We performed similar calculations for a two site jump, and six site jump models in both the strong and weak collision limit and these calculations show the same trends as the rotational diffusion calculation and we are not able to distinguish these subtleties in the motion.

In the slow motion regime for the rotation of the C-S bond in the thiophenol, the theory we have presented is invalid. This can be seen in figures 2.5.2 to 2.5.5 by the fact that when the C-S bond is not rotating (the infinite correlation time limit for this motion) the relaxation times do not attain the expected ortho:meta:para ratio of 1:1/2:1/2. The reason for the failure of the theory in this limit is the assumption that the overall rotation of the particle is uncorrelated to the internal rotation. Thus the separation of the correlation function in equation 2.5.4 into two separate ensemble averages is inaccurate. As future work, this ensemble average will be carried out in a single step.

Section 2.6: Conclusions about Thiophenol Motions on the Nanocrystal Surface

In this chapter, we have presented ^{1}H and ^{13}C NMR data on the thiophenol ligands of CdS nanocrystals. These data have provided a wealth of information on the surface structure and dynamics of these materials. The data clearly show that the surface coverage by the observed thiophenol molecules is low and that this coverage increases as the particles become smaller. Since all the nanocrystals are synthesized with an excess of thiophenol, this result is not a consequence of an insufficient quantity of thiophenol to cause a highly covered surface, but must be due to a kinetic constraint on the coverage process. Perhaps the smaller nanocrystals require higher coverage to force them out of the micelles in which they are formed and precipitate.

We concluded in section 2.2 that the thiophenol coverage is so low that if the thiophenol ligands are homogeneously dispersed on the nanocrystal there should be negligible interaction between the thiophenol molecules. However, our relaxation calculations suggest that the data can most simply be explained if we assume that the correlation time of the rotation about the C-S bond in a bridgingly bound thiophenol is slow, longer than 10^{-8} sec. This long correlation time suggests a highly hindered rotor for which there are at least three possible explanations. First, the distribution of thiophenol ligands on the surface is not homogeneous, but rather the thiophenol ligands form covered islands on the surface. In this case the densely covered regions would make rotation highly sterically hindered. The motion could also be sterically hindered if the thiophenol molecules are homogeneously distributed across the surface, but that the solvent pyridine densely covers the rest of the thiophenol surface. The pyridine must be at least exchanging on and off the surface, and we have yet to see any positive evidence that it really associates with the surface. The final explanation is that the C-S bond is not free to rotate because of conjugation of the ring pi electrons to the sulfur lone pair and then to the surface atoms. If the thiophenol is bound in a bridging fashion, the sulfur would be sp2 hybridized leading to good overlap of the lone pair electrons with the pi electrons in the benzene ring. This conjugation could continue into the surface via the Cd d-orbitals. Of course it would be difficult to explain the change in the correlation time with size for the last two hypotheses.

Along with the unusually long correlation times for the internal rotation rate, we also see an unusual temperature dependence of the relaxation times. We see the ^1H transverse relaxation time decrease as the temperature is increased. Our motional model predicts that the correlation time then must increase with temperature. This is contradictory to the idea that the motion was so slow because of steric hindrance. If this were true, the correlation time should decrease as the temperature is raised and increase the relaxation time. Possibly a reversible increase of the surface thiophenol density occurs as the temperature is raised, however, it is nonintuitive that such a change would be reversible.

Another possible explanation is that the motional model we have proposed is wrong, and the correct explanation is that we are seeing one site of thiophenol that exchanges to an unobserved second site. This would explain the increase in T_2 as the temperature is raised, but we have never seen any suggestion of another site in our data. The data would also imply that the exchange rate would depend upon the nanocrystal radius. This implication is highly suspect.

The final possibility is that there are two mechanisms responsible for the observed relaxation data. The ratio of the various relaxation times is explained by the dipolar relaxation mechanisms presented in section 2.5. However, the temperature dependence is governed by some other mechanism. A possible mechanism is paramagnetic relaxation of the ^1H by a thermally populated paramagnetic state of the nanocrystal. This mechanism is consistent with the data presented in table 2.3.1 where it is seen that the smaller nanocrystals have smaller changes in the relaxation rates than do the larger particles. Since the band gap of the nanocrystal gets smaller as the nanocrystal gets larger, the population of the thermally excited paramagnetic state should become larger as the particle gets bigger thus making the paramagnetic relaxation more robust.

In conclusion, we have presented the first NMR study of the surface structure of semiconductor nanocrystals. It seems that these spectra, while at first sight appearing relatively simple, conceal a wealth of information not only about the nature of the surface but also possible of the core. The spectra show that the nanocrystal surface is not completely capped. Rather, due to nanocrystal faceting, steric effects or kinetic limitations of the capping process, islands of covered regions seem to exist which are separated by uncovered regions. Furthermore, to consistently explain both our ^1H and ^{13}C data these covered islands must be fairly densely packed with thiophenol molecules to cause the 10^{-8} sec correlation times of the rotation of the thiophenol molecules. We also propose the existence of a thermally activated paramagnetic state that contributes significantly to the relaxation of the larger nanocrystals at higher temperatures.

Until now, such detailed information about the structure and dynamics of surface capping molecules on nanocrystal surfaces has been difficult to obtain. NMR appears to be an ideal tool for extracting this information, which is needed in order to understand fully such properties of the nanocrystal as ultrafast trapping of photon-generated electrons and holes.[26-29] By binding organic molecules to the surface, one hopes to move all mid or near band gap surface states to much higher energies. Clearly, to accomplish this, the coverage will need to be increased to saturation and the effects of these changes on the surface can be monitored by NMR.

Chapter 3: Determining Conformational Parameters in Small Peptides by Measuring Scalar Relaxation Rates

Section 3.1: Introduction

NMR spectroscopy determines the structure of biological molecules by providing the researcher with distances between ^1H nuclei and conformation constraints on torsion angles. The internuclear distances are measured using Nuclear Overhauser Spectroscopy (NOESY), while the conformational constraints are determined from an analysis of the scalar coupling (J-coupling) between different nuclei. The distance information from the NOESY experiment is crucial for determining the basic backbone folding pattern of a protein; however, it is not sufficient to determine sidechain conformations in proteins or sugar ring and phosphate backbone conformation in RNA or DNA. In these cases, the precise measurement of J-couplings becomes more important.

The J-coupling provides a measure of the conformation of a small region of the molecule because these couplings vary with the torsion angle of the bonds between the two nuclei. This was first theoretically shown by Martin Karplus in 1959[1], and then he later showed that the variation of the J-coupling in the molecular fragment (HCC'H') can be approximated by the Karplus equation,

$$J_{HH'} = A + B\cos\phi + C\cos 2\phi, \qquad \text{(eq. 3.1.1)}$$

where ϕ is the dihedral angle. Karplus calculated values of A, B, and C, but it was found to be more accurate to empirically fit these parameters. This equation has been empirically applied to J-couplings other than just those between two protons and has shown itself to be reliable. These empirically fit equations have become the basis for extracting dihedral angles from the measured J-couplings.

In principle, the values of these J-couplings can be determined from the normal one-dimensional experiment; however, spectral overlap normally prevents this, so that analysis of cross-peaks in correlation spectroscopy (COSY) becomes necessary. The cross-peaks in the normal COSY spectrum become complicated in large systems leading to overlap of the numerous multiplet components. Thus, the techniques commonly used to acquire J-couplings simplify the cross-peak structure by limiting the coherence transfer to directly connected transitions, i.e. those sharing a common energy level. The first technique proposed to make this simplification is the E. COSY experiment[2], which consists of a superposition of 2,3, and 4 quantum filtered COSY spectra in a ratio 1:2:4. This experiment gives rise to coherence transfer exclusively between connected transitions for weakly coupled spins, and, for this reason, is called exclusive correlation spectroscopy (E. COSY). Another experiment which results in coherence transfer between directly connected transitions is the z-COSY[3], which produces coherence transfer through multispin longitudinal order. Unfortunately, this experiment suffers from inferior signal to noise ratio when compared to the E. COSY, but it is also considerably easier to perform. Finally, the selective COSY experiment[4], which uses selective pulses to selectively transfer coherence between two spins, has recently been shown to lead to the same type of spectra as the E. and z-COSY experiments, but has the advantage of excellent spectral resolution because the sweep widths can be made very small; commonly 500 by 200 Hz. All of these techniques give rise to the same distinctive crosspeak intensity pattern: four lines with the signs $\begin{pmatrix} + & - \\ - & + \end{pmatrix}$ due to coupling between active spins and then splitting of this pattern into two

identical patterns displaced by the coupling constant to the passive spin. Notice that such a cross-peak pattern contains much information about the coupling network.

These techniques suffer from two disadvantages when one wants to measure J_{NH} couplings. First, in large proteins, it is hard to determine the J-couplings by these methods because of the increasing linewidths in the spectra lead to cancellation problems. Finally, to perform these techniques, the protein must be enriched with ^{15}N in order to observe a splitting due to the J-coupling, because the splitting due to the quickly relaxing spin 1 ^{14}N nucleus is unobservable. However, the effect of the quickly relaxing ^{14}N nucleus can be observed on the relaxation of the ^{1}H nuclei to which it is scalar coupled. This effect on the ^{1}H nuclei is known as scalar relaxation of the second kind and is related to the scalar coupling between the ^{1}H and ^{14}N nuclei. This chapter will present a new technique for measuring these J-couplings by measuring this scalar relaxation rate. We will present data for the extreme narrowing case only, but with additional measurements, one should be able to measure these coupling in larger molecules.

Section 3.2: The Approach: Exploiting Scalar Relaxation of the Second Kind

The scalar coupling between a slowly relaxing nucleus, such as an ^{1}H nucleus, and a quickly relaxing quadrupolar nucleus, such as the ^{14}N nucleus, can enhance the transverse relaxation rate of the more slowly relaxing nucleus. This effect is directly related to the scalar coupling (J-coupling) between the fast and slowly relaxing nuclei, and can be exploited to measure this coupling. In this section, we will show what effect this scalar relaxation has on the observed relaxation rates and will present a method for determining the J-coupling from the relaxation rates.

The scalar relaxation rates can be derived by using the formalism of section 1.10 if we assume that the quadrupolar ^{14}N nucleus relaxes so quickly that it can be assumed to be

a part of the lattice[5]. In this case, the time-dependent Hamiltonian responsible for the relaxation of the ^{1}H nucleus is

$$H_1(t) = 2\pi J \mathbf{I} \cdot \mathbf{S}(t), \qquad \text{(eq. 3.2.1)}$$

where **I** and **S** are the angular momenta of the ^{1}H and ^{14}N, respectively, and J is the scalar coupling between the nuclei. One can rewrite this equation as

$$H_1(t) = \gamma_I \mathbf{B}_S(t) \cdot \mathbf{I}, \qquad \text{(eq. 3.2.2)}$$

where $\mathbf{B}_S(t) = 2\pi J \mathbf{S}(t)/\gamma_I$ is the fluctuating magnetic field seen by the ^{1}H created by the ^{14}N nucleus. If we now follow the formalism presented in section 1.10, we can calculate the longitudinal and transverse relaxation times for this relaxation mechanism. They are

$$\frac{1}{T_1^{SR}} = \frac{8\pi^2 J^2}{3} S(S+1) \frac{{}^{14N}T_2}{1+(\omega_I - \omega_S)^2 {}^{14N}T_2^2} \qquad \text{(eq. 3.2.3)}$$

and

$$\frac{1}{T_2^{SR}} = \frac{4\pi^2 J^2}{3} S(S+1) \left\{ \frac{{}^{14N}T_2}{1+(\omega_I - \omega_S)^2 {}^{14N}T_2^2} + {}^{14N}T_1 \right\}, \qquad \text{(eq. 3.2.4)}$$

where S is the angular momentum quantum number of the ^{14}N nucleus, which equals 1, and ${}^{14N}T_1$ and ${}^{14N}T_2$ are the longitudinal and transverse relaxation times of the ^{14}N nucleus. For most biomolecules in solution at typical magnetic field strengths, $(\omega_I - \omega_S)^2 {}^{14N}T_2^2$ is a large number , which allows us to simplify the above equations to

$$\frac{1}{T_1^{SR}} \approx 0 \qquad \text{(eq. 3.2.5)}$$

and

$$\frac{1}{T_2^{SR}} \approx \frac{8\pi^2}{3} J^{2\,14N} T_1. \qquad \text{(eq. 3.2.6)}$$

Thus the scalar relaxation of the second kind reduces the transverse relaxation rate while not perturbing the longitudinal rate.

Since the scalar relaxation of the second kind only effects one of the measurable relaxation rates, we now have a method for measuring the scalar relaxation rate. If the proton relaxation in the molecule under study is assumed to be caused by both the scalar relaxation mechanism and the dipole-dipole mechanism, the measured relaxation times can be written as

$$\frac{1}{T_1} = \frac{1}{T_1^{DD}} + \frac{1}{T_1^{SR}} \approx \frac{1}{T_1^{DD}} \qquad \text{(eq. 3.2.7)}$$

and

$$\frac{1}{T_2} = \frac{1}{T_2^{DD}} + \frac{1}{T_2^{SR}} \approx \frac{1}{T_2^{DD}} + \frac{8\pi^2}{3} J^{2\,14N} T_1. \qquad \text{(eq. 3.2.8)}$$

If we are studying a molecule in the extreme narrowing limit, then the difference in the ^{1}H longitudinal and transverse relaxation rates directly measures the scalar relaxation rate:

$$\frac{1}{T_2} - \frac{1}{T_1} \approx \frac{8\pi^2}{3} J^{2\,14N} T_1. \qquad \text{(eq. 3.2.9)}$$

To determine ^{14}N to ^{1}H scalar couplings of biomolecules, we measured proton longitudinal and transverse relaxation times and the ^{14}N longitudinal relaxation time. By using equation 4.2.9, we can then extract the square of the J-coupling which can be used to place conformational constraints on the molecule under study. The only fundamental limit

of this approach at this time is that the molecule must be undergoing rapid tumbling in the extreme narrowing limit. In slower tumbling regimes, more measurements must be made to separate the dipole-dipole mechanisms from the scalar relaxation mechanism. We have not gone into explicit detail on how to perform this more complicated set of experiments.

Section 3.3: Measuring $J_{^{14}NH}$ Couplings in Pyridine

To investigate the feasibility of this proposed strategy for measuring ^{14}N-H J-couplings and to evaluate its potential problems, we studied a simple model compound, pyridine. This compound provides many advantages for initial studies of this type. It is a small molecule and therefore is tumbling in the extreme narrowing limit. It is easy to make concentrated samples, and the spectrum is well resolved, so established NMR techniques can be used to measure the needed relaxation times. For these reasons, we attempted to measure the $J_{^{14}NH}$ to the ortho ^{1}H in a sample of 0.05 ml of freshly distilled pyridine diluted into 0.5 ml of d_5-pyridine (99.99% deuterated, Aldrich) from a freshly opened vial. The sample was degassed by repeating the freeze-pump-thaw method five times. All relaxation measurements were performed on a Bruker 400AMX spectrometer with a recycle delay of 5 minutes.

As presented in the previous section, we need to measure the T_1 and T_2 of the ortho proton and the T_1 of the ^{14}N nucleus. The ^{1}H T_1 was measured by a nonselective inversion-recovery sequence, 180°-τ-90°-acq, which gives monoexponential recovery of the ^{1}H magnetization. The ortho proton longitudinal relaxation time measured in this way was 62.7 sec. The transverse relaxation time was measured using the selective Hahn echo of Emsley, Kowalewski, and Bodenhausen[6], which was described in section 2.3 of this thesis. The ortho proton transverse relaxation time measured with this method was 208 msec. The ^{14}N T1 was measured directly from fitting the ^{14}N spectrum to a Lorentzian line and recognizing that in the extreme narrowing limit

$$T_1 = \frac{1}{\pi \Delta \upsilon_{FWHM}}. \qquad \text{(eq. 3.3.1)}$$

In this way, the ^{14}N T_1 was determined to be 1.47 msec. From these data and equation 3.29, we found that the absolute value of the ^{14}N-ortho ^1H J-coupling is 11.1 Hz. The value of the ^{15}N-ortho ^1H J-coupling is reported to be -10.76 Hz[7] When this value is scaled by the ratio of ^{14}N to ^{15}N gyromagnetic ratios, the ^{14}N-ortho ^1H J-coupling should be -7.67 Hz. This error of 45% is not explained by the error in our relaxation measurements.

The method we have described for determining $J_{^{14}NH}$ depends on a precise cancellation of all relaxation effects other than the desired scalar relaxation. This is true when the other relaxation pathways are dipole-dipole effects, however, cancellation does not occur when the ^1H undergoes relaxation due to chemical shift anisotropy. Wittebort and Szabo[8] present the expressions for relaxation due to chemical shift anisotropy:

$$T_1^{-1} = CJ(\omega_0) \qquad \text{(eq. 3.3.2)}$$

and

$$T_2^{-1} = \frac{C}{6}\left[4J(0) + 3J(\omega_0)\right], \qquad \text{(eq. 3.3.3)}$$

where

$$C = \frac{\gamma_I^2 B_0^2}{4}\left[2\delta_Z - (\delta_X + \delta_Y)\right]^2 \qquad \text{(eq. 3.3.4)}$$

and the δ's are the principal values of the chemical shift tensor. Including this effect, the difference in the transverse and longitudinal relaxation rates is now

$$T_2^{-1} - T_1^{-1} = AB_0^2 + \tfrac{8\pi^2}{3} J_{^{14}NH}^2 \, {}^{14}N T_1, \qquad \text{(eq. 3.3.5)}$$

where $A = \frac{\gamma_I^2}{4}\left[2\delta_Z - (\delta_X + \delta_Y)\right]^2$. This mechanism predicts that the error in the determination of the ^{14}N-H J-coupling should have a strong magnetic field dependence.

The appropriate relaxation times were measured for a sample of 0.05 ml of freshly distilled pyridine dissolved in 0.5 ml of d_6-DMSO (Aldrich, 99.99% deuterated) which had been freeze pump thawed and then sealed in the NMR tube to exclude O_2. The relaxation measurements on this sample were performed on a Bruker 600AMX spectrometer. We measured the relaxation rates as before, and found that the longitudinal and transverse relaxation times of the ortho proton were 1.08 sec and 50.3 msec, respectively. The longitudinal relaxation time of the ^{14}N nucleus was measured to be 1.40 msec. With these data, we calculated the ^{14}N-^{1}H ortho J-coupling to be 22.7 Hz. Thus we can see that the determined J-coupling does depend strongly on the magnetic field. Unfortunately, the change in solvent between the 400 MHz and the 600 MHz experiments made extraction of the correct J-coupling value impossible.

In this section, we have shown that extraction of approximate values of $J_{^{14}NH}$ is possible as long as one either works at lower field strengths or performs an explicit magnetic field dependence of the data. Acknowledging these limitations, we decided to measure biologically relevant J-couplings in a small peptide and see if this method could be used to obtain information on amino acid sidechain conformation in a small peptide.

Section 3.4: Three Bond ^{14}N-H J-couplings in Residue Sidechains of Oxytocin

The goal of this research is to obtain biologically relevant ^{14}N-H J-couplings in order to constrain the conformation of a biomolecule. To investigate this possibility, we

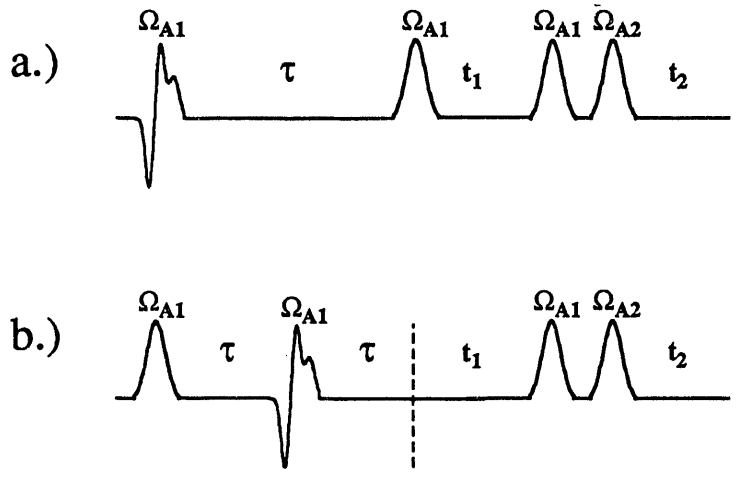

Fig. 4.3.1: Pulse sequences suitable for recording two-dimensional longitudinal and transverse relaxation spectra. a.) This sequence measures the selective inversion recovery of a spin whose resonance frequency is Ω_{A1}. It consists of a selective inversion at Ω_{A1} followed by a selective COSY to transfer the coherence to a spin at .Ω_{A2}. b.) This sequence measures the decay of a selective Hahn echo of a spin whose resonance frequency is Ω_{A1}. It consists of a selective Hahn echo at Ω_{A1} followed by a selective COSY to transfer the coherence to a spin at .Ω_{A2}.

attempted to measure the three bond ^{14}N-H_β J-coupling in the isoleucine residue of the small peptide oxytocin. Oxytocin is a small peptide with nine amino acids and a molecular weight of 1007 Da. At room temperature, the correlation time for the isotropic tumbling of this peptide in an H_2O solution is at the T_1 minimum, however, when the sample is heated to 40°C, the peptide is then moving in the extreme narrowing limit, and our approach for measuring the J-couplings can be applied. We prepared a sample of 20 mg of oxytocin dissolved in 0.5 ml of H_2O to which 0.05 ml of D_2O had been added. The acidity of the sample was adjusted to a pH of 3. All experiments were performed on a Bruker AMX400 spectrometer.

Because of the larger size of this molecule and its greater spectral complexity than the previously examined pyridine, simple inversion recovery sequences and selective T_2 experiments could not be used. Methods which dealt with the spectral overlap problems had to be developed. These new techniques consisted of combining the relaxation

a.)

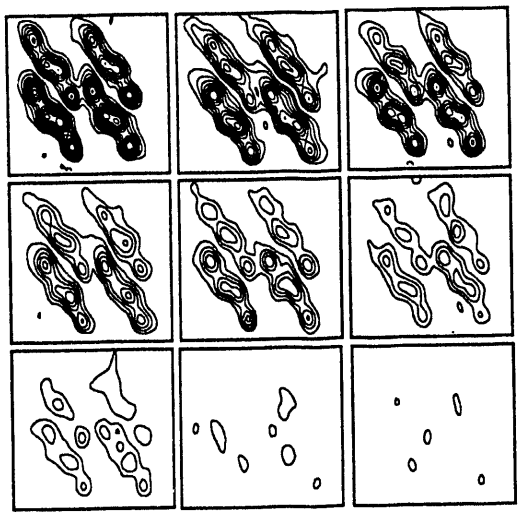

b.)

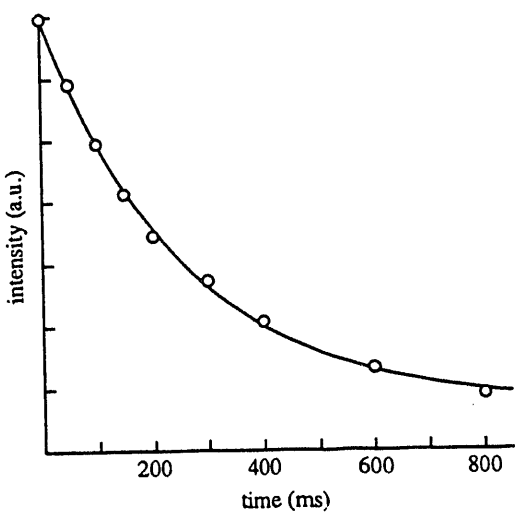

Fig. 3.4.2: a.)A series of spectra resulting from the application of the Hahn echo COSY sequence which correspond to the 2'-2" cross peak of T1 in *d*-TATA. The delay times 2τ are (from left to right and top to bottom), 0, 50, 100, 150, 200, 300, 400, 600 and 800 ms respectively. No distinction is made between positive and negative contours. The spectra were acquired using a 10 mmol solution of *d*-TATA in D_2O at 400 MHz and 44K, with spectral widths of 200 x 500 Hz and a digital resolution of 64 x 256 points in t_1 and t_2, zero-filled to 256 x 1024 before apodization and Fourier transformation. b.) A plot of the integrated intensities of the cross peaks as a function of 2τ (open circles), together with the best fit value of the transverse relaxation rate, which yields $T_2 = 258$ ms. Note that the intensity does not decay to zero, but to a constant value which represents the integral of the absolute value of the noise in the spectra.

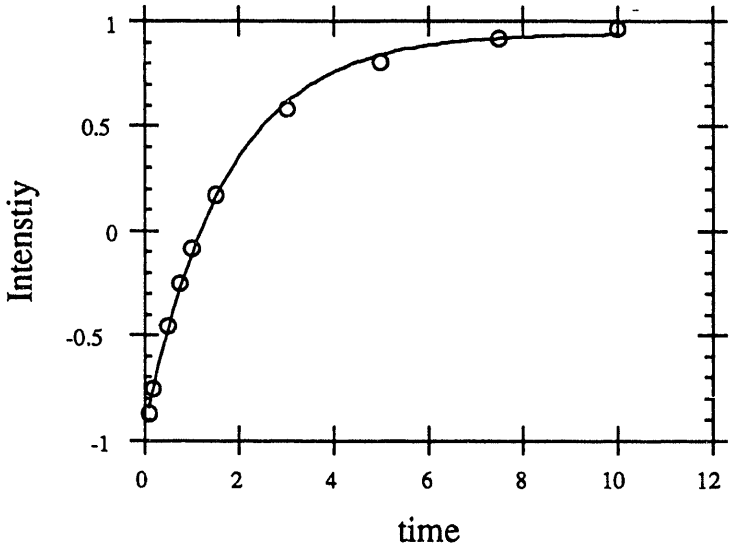

Fig. 3.4.3: Fit of simulated biexponential recovery data with a single exponential recovery. The circles correspond to data simulated with the equation $I(t) = 1 - e^{-t} - e^{-3t}$. The line is the best fit of the simulated data to the function $I(t) = A\left(1 - 2e^{-t/T_1^{eff}}\right)$. The best fit value of T_1^{eff} was 1.71.

experiments with a 2-D selective COSY so that only a single nuclear site is observed. The sequences for a selective inversion recovery COSY and a selective Hahn echo COSY are shown in figure 3.4.1. A test of these sequences is shown in figure 3.4.2, which shows results for the selective Hahn echo COSY on a sample of the single stranded DNA tetramer TATA. As can be seen, the intensity of the absolute value of the observed T_1 2'-2" crosspeak[9] decays monoexponentially to a constant value, which is the integral of the absolute value of the noise. The selective inversion recovery COSY spectra are of similar quality.

Unfortunately, the interpretation of the selective inversion recovery sequence is complicated by the expected biexponential recovery of the magnetization. As shown is section 1.10 of this thesis, the result of this experiment for a two spin system undergoing dipole-dipole relaxation should be biexponential with a ratio of relaxation times of 3:1 if the molecule is tumbling in the extreme narrowing limit. The data that we will present is not of sufficient quality to make this biexponential fit, so the data was fit to a single exponential.

Figure 3.4.3 shows a monoexponential fit to biexponential data where the relaxation times are related by the 3:1 ratio. As can be seen, the fit is quite good and the determined relaxation time by this method is approximately 1.71 times the true relaxation time. A justification for this scaling factor can be made by Taylor expanding the equation for the biexponential recovery of the system:

$$I_Z(t) = I_\infty\left(1 - e^{-t/T_1} - e^{-t/3T_1}\right)$$

$$= I_\infty[1 - \left(1 - \frac{t}{T_1} + \frac{1}{2!}\left(\frac{t}{T_1}\right)^2 - \frac{1}{3!}\left(\frac{t}{T_1}\right)^3 + \ldots\right)$$

$$- \left(1 - \frac{t}{3T_1} + \frac{1}{2!}\left(\frac{t}{3T_1}\right)^2 - \frac{1}{3!}\left(\frac{t}{3T_1}\right)^3 + \ldots\right), \qquad \text{(eq. 3.4.1)}$$

which upon collecting terms becomes

$$I_Z(t) = I_\infty[1 - 2\left(1 - C_1\frac{t}{T_1} + \frac{1}{2!}C_2\left(\frac{t}{T_1}\right)^2 - \frac{1}{3!}C_3\left(\frac{t}{T_1}\right)^3 + \ldots\right), \qquad \text{(eq. 3.4.2)}$$

where $C_n = \frac{1}{2}\left[1 + \left(\frac{1}{3}\right)^n\right]$. If the first three C_n's are averaged and used to define a single exponential recovery, the longitudinal magnetization can be approximated by

$$I_Z(t) = I_\infty\left(1 - 2e^{-t/T_1^{eff}}\right), \qquad \text{(eq. 3.4.3)}$$

where $T_1^{eff} = 1.72T_1$. This is close to the scaling factor seen above when the biexponential curve was fit to a single exponential. In order to interpret our data, we will divide our fit T_1 values by 1.71 to take into account the neglected biexponentiality. The biexponentiality of the recovery could be removed if the selective inversion pulse were replaced by a nonselective pulse that inverted all ^{1}H resonances. This experiment has not yet been performed.

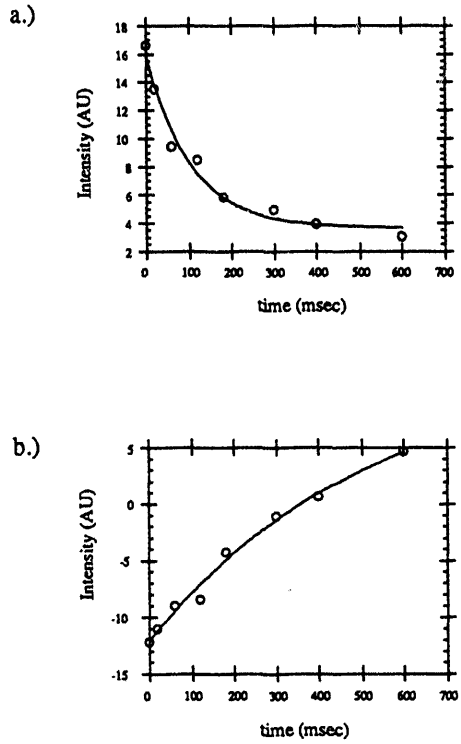

Fig. 3.4.4: Transverse and longitudinal relaxation data for the b proton of the isoleucine residue of oxytocin. a.) The transverse relaxation data for this proton measured with the Hahn echo COSY experiment. Notice that the data decay to a constant, which is the integral of the absolute value of the noise. b.) The longitudinal relaxation data measured with the inversion recovery COSY. The given intensity data are measured by taking the integral of the absolute value of the data minus the integral of the noise. The absolute value of the data must be taken in both cases because the integral of the selective COSY crosspeaks is zero because of its antiphase nature.

The longitudinal and transverse relaxation data for the β proton of the isoleucine residue of oxytocin is presented in figure 3.4.4. These data are quite good and allowed the relaxation times to be measured: T_1^{eff}=526 msec, which implies that the true longitudinal relaxation time is T_1=308 msec, and T_2=103 msec. Direct attempts at measuring the ^{14}N T_1 failed because of the low sensitivity of this nucleus. This relaxation time was measured by taking advantage of the scalar relaxation rate of the amide proton for which the ^{15}N-H J-coupling is known to be 93.2 Hz[10], which scales to a value of 66.4 Hz for the ^{14}N-H J-coupling. Effects due to exchange are minimized because the pH of the sample was

adjusted to a value of 3 where exchange is at a minimum for amide protons.[11] The effective longitudinal relaxation time of the amide proton and the transverse relaxation time of this proton was measured using the same selective sequences described above. The effective longitudinal relaxation time for the amide proton was 238 msec, which implies that the real T_1 is 139 msec. The transverse relaxation time was measured to be 121 msec. From these data, the ^{14}N T_1 was determined to be 9.2 μsec and the J-coupling between the ^{14}N and the β proton was 163 Hz. This value of the J-coupling is in outside the expected range of 0 to 5.6 Hz. The error is probably due to relaxation due to chemical shift anisotropy and exchange of the amide proton leading to an inaccurate measure of the longitudinal relaxation time of the 14N nucleus. This problem with amide proton exchange can be eliminated by using the H_α proton as the spy on the ^{14}N relaxation time, because its J-coupling to this nucleus is always approximately 2.2 Hz[10]. The effect of the chemical shift anisotropy relaxation mechanism can be analyzed be performing a field dependence of the relaxation data.

Section 3.5: Conclusions

In this chapter, we have presented preliminary results suggesting a new method for measuring ^{14}N-^{1}H J-couplings in biological molecules. We have shown that the technique is viable, however, many details of the method need to be worked out. As seen in the pyridine data, relaxation due to chemical shift anisotropy causes the largest error in this method for small molecules, but this effect can be separated from scalar relaxation by measuring the field dependence of the difference in relaxation rates. Much more work will need to be done to apply this technique to measuring J-couplings in large molecules where the longitudinal and transverse relaxation times due to dipole-dipole relaxation are not the same. By performing additional measurements, these effects should be separable.

An additional piece of information provided by this technique is the longitudinal relaxation time of the ^{14}N nucleus in the amide bond. This parameter is itself important because it provides important constraints on the backbone motion of the peptide and this method could provide a simple, inexpensive method for measuring these relaxation rates. The technique presented here has many possibilities for future applications and is currently under active research.

Chapter 4: Solid State Magic Angle Spinning: Cross Relaxation NMR Spectroscopy of Homonuclear Dipolar Coupled Spin Systems

Section 4.1: Introduction

The high field carbon-13 NMR spectrum of a static solid sample containing many different ^{13}C sites is determined by a Hamiltonian which contains both chemical shift and dipolar interactions.[1-3] These interactions can be represented by first and second rank spherical tensor components to express the spatial and spin dependence of the Hamiltonian. The spectrum contains all the parameters necessary to determine the three dimensional structure of the molecule under investigation. Unfortunately the spatial dependence of the second rank terms broadens the resonances and makes the spectra of all but the simplest systems difficult to interpret, even in the presence of high power proton decoupling.

A quantum leap was made in solid state NMR with the introduction of magic angle spinning (MAS).[4] In this experiment the sample is rapidly rotated ($\approx 10^4$ Hz) about an axis inclined at an angle 54.74° with respect to the magnetic field. This has the effect of averaging the anisotropy of the chemical shift and dipolar interactions to a single value by removing the second rank terms from the effective Hamiltonian. In the case of the chemical shift this average value is the so called "isotropic" chemical shift, and is different for different chemical environments. This leads to a high resolution spectrum of narrow lines, which allows identification of the different sites in a manner analogous to a liquid state

spectrum. Since there are no first rank contributions the average value of the dipolar interaction under magic angle spinning is zero. Thus, whilst MAS allows one to obtain a high resolution spectrum, the resolution is achieved by sacrificing information about dipolar couplings.

Recently there has been considerable interest in retaining the resolution of magic angle spinning, but nevertheless including information about homonuclear dipolar couplings.[5-16] Methods such as rotational resonance have been successfully applied to structure determination,[17,18] but they depend on pairwise measurements; the technique is *selective*. Recently, the idea of radio frequency driven recoupling has been introduced in which a train of pulses is applied that leads to an average Hamiltonian which is proportional to the homonuclear dipolar Hamiltonian over a reasonably broad range of chemical shifts.[5-7,11,13,16] The object of this type of experiment is to develop a *broadband* method for measuring all the dipolar couplings in one experiment. The main disadvantage of these techniques is the need to apply complex mixing sequences consisting of many pulses.

In this chapter, we present initial results obtained from an alternative approach towards broadband dipolar correlation under magic angle spinning which does not require the application of pulses during the mixing period. Our technique correlates resonances by using dipolar cross relaxation between the carbon nuclei. Two dimensional solid state MAS cross relaxation spectra have been recorded for both triply ^{13}C L-labeled alanine and doubly ^{13}C labeled zinc acetate, yielding results reminiscent of liquid state NOESY spectra.[19]Cross relaxation between carbon atoms as a mechanism for correlating spins in solids has previously been discounted as unlikely to provide sufficiently rapid transfer rates. Although the timescale for transfer we observe is longer than would be observed under conditions where the full dipolar Hamiltonian is reintroduced, cross relaxation is much faster than expected in these rigid systems. We discuss possible mechanisms of polarization transfer in terms of either the restricted motion of the carbon skeleton using conventional second order treatments, or the motion of nearby protons using third order

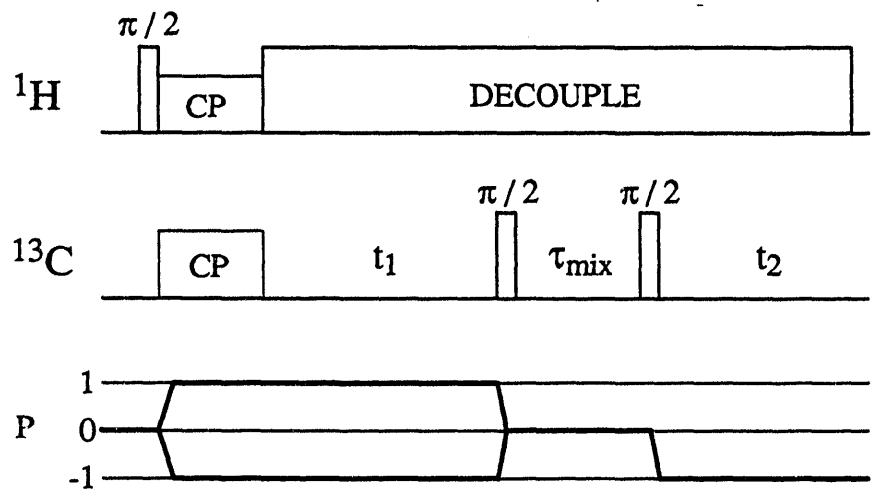

Fig. 4.2.1: Pulse sequence used to record magic angle spinning cross relaxation spectra. The sequence uses cross polarization from protons to create carbon single quantum coherence which evolves with a characteristic frequency during t_1, and which is then stored along the z-axis by the action of the $\pi/2$ mixing pulse for a period τ_{mix}. The magnetization is then recalled and detected during t_2. High power proton decoupling is applied throughout the sequence. The phases of the carbon spin lock pulse and the storage pulse are cycled in order to retain only the carbon coherence transfer pathway shown below the sequence.

perturbation theory. The method appears to provide a particularly simple broadband means of correlating distances in solids which should be useful for both assignment and structure determination.

Section 4.2: Experimental

Cross relaxation spectra were recorded using the pulse sequence shown in Fig. 4.2.1. The experiment consists of two free precession periods separated by a mixing period during which longitudinal ^{13}C magnetization is exchanged on a timescale of tens of milliseconds. The protons are subjected to high power decoupling throughout the sequence, preventing transfer through proton polarization and thereby quenching polarization transfer

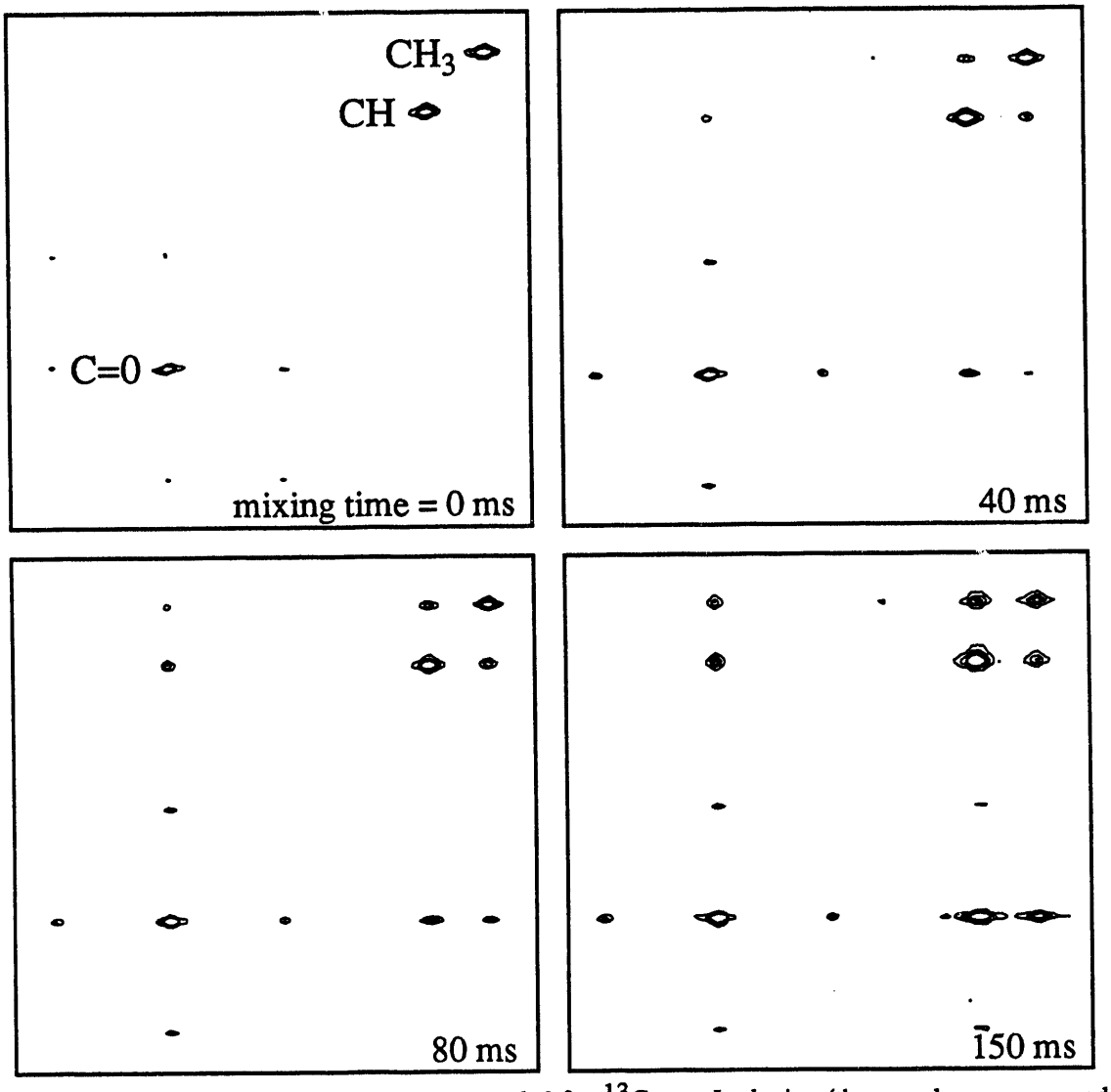

Fig. 4.2.2: Four cross relaxation spectra recorded for $^{13}C_{1,2,3}$-L-alanine (the sample was prepared as described in the text). The spectra were recorded at room temperature using the pulse sequence of Fig. 1 on a "homebuilt" spectrometer operating at a proton frequency of 301 MHz (^{13}C = 75.7 MHz) using a tecmag operating system and a homebuilt magic angle spinning probe. 256 points in t_2 were acquired for each of 64 points in t_1. Each increment was averaged for eight scans yielding a total acquisition time of ≈30 minutes per spectrum. The spectra were zero filled to 256 × 128 and apodized with a Lorentzian line broadening function before two dimensional Fourier transform and phasing. Phase sensitivity was achieved using the States method. The spinning speed was carefully adjusted to 4.25 kHz, so that there should be no effects from rotational resonance. The mixing time τ_{mix} is shown in the lower right corner of each spectrum.

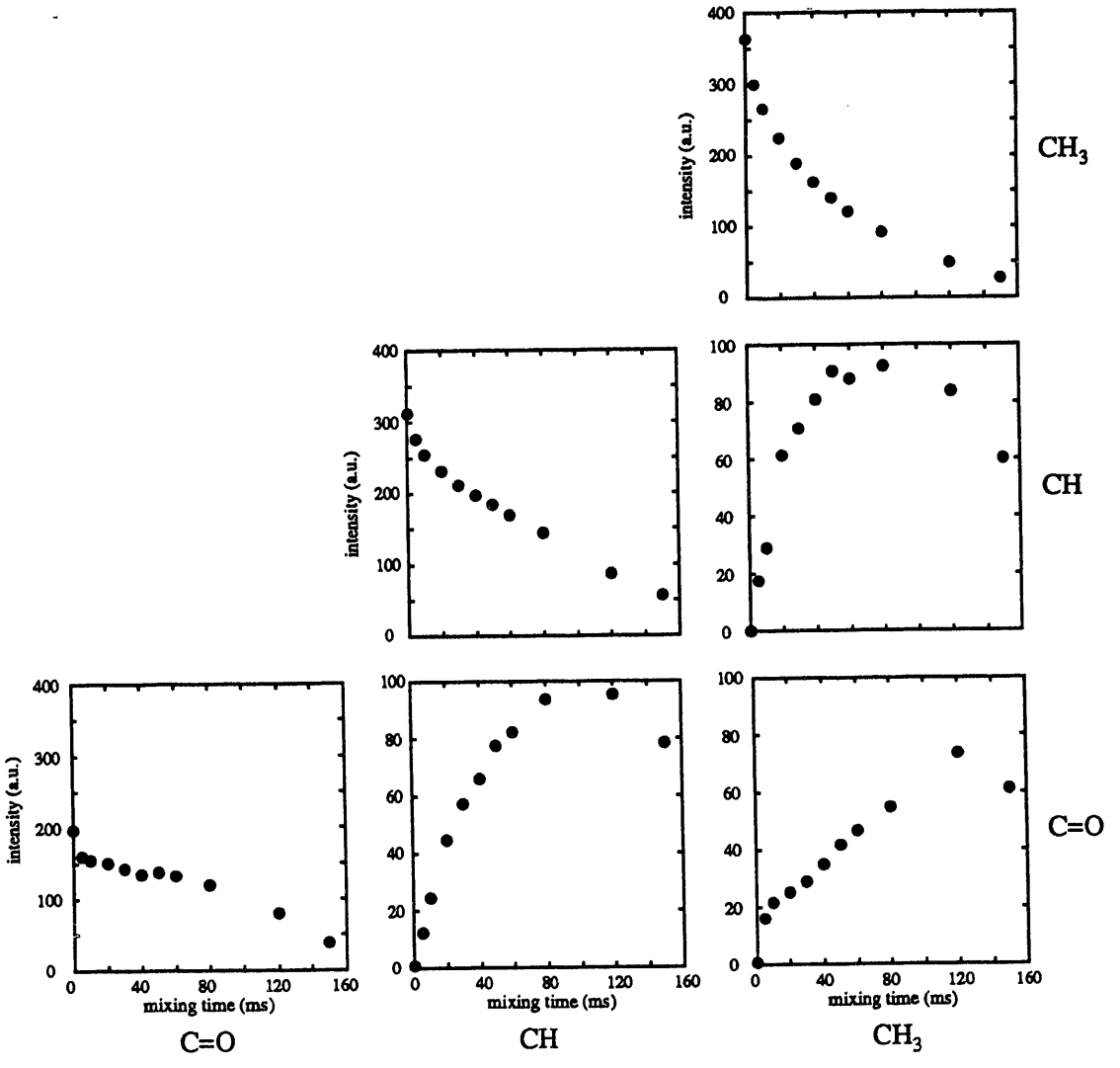

Fig. 4.2.3: Integrated intensities of the peaks observed in the spectra of Fig. 2 together with spectra corresponding to other values of the mixing time τ_{mix} ranging from 0 to 150 ms (longer times are inadvisable due to problems with high power decoupling and probe breakdown). The cross peak integrals were obtained by summing the cross peaks on both sides of the diagonal. Note the change in scale between the cross peaks and the diagonal peaks. The initial rates measured for the cross peak growth are given in table 1. It is important to notice that the growth rates are not oscillatory in nature, but have the appearance of exponential behavior typical for cross relaxation, as discussed in the text.

		CH_3
	CH	20±6
C=O	28±6	65±5

Table 4.2.1: Cross relaxation rates between ^{13}C nuclei in $^{13}C_{1,2,3}$-L-alanine determined from the initial slopes of the buildup curves shown in Fig. 3. The rates are shown in $(ms)^{-1}$

between carbons by proton driven spin diffusion, a subject which has received much attention in its own right.[8-10]

Figure 4.2.2 shows four spectra taken from a series recorded with different values of the mixing time for a sample of 10% triply labeled $^{13}C_{1,2,3}$-L-alanine co-crystallized with 90% natural abundance L-alanine. In this way we can be sure that there is no significant contribution to cross relaxation from intermolecular mechanisms. If cross relaxation is occurring we expect that as the mixing time gets longer, the ratio of the cross peak to diagonal peak intensity gets larger, and that is indeed what we observe. In Fig. 4.2.3 we plot the intensities of the diagonal and the cross peaks in the L-alanine spectrum as a function of mixing time. At short mixing times we observe only diagonal peaks (together with cross peaks between sidebands of the C=O resonance; if necessary these peaks can

simply be removed by synchronizing the mixing time to an integral number of rotor periods). It is particularly interesting to note that the initial rates of buildup of the cross peaks extracted from these curves (given in table 4.2.1) show a relatively fast, and more or less equal, rate for both the one bond C-C cross peaks, and a much slower rate for the CH_3-C=O cross peak which corresponds to a larger distance. These spectra represent the first observation of direct cross relaxation between carbon atoms in a solid.

In order to confirm that there is an extra relaxation pathway in the enriched compound, we measured the decay of longitudinal polarization shown in figure 4.2.4. As

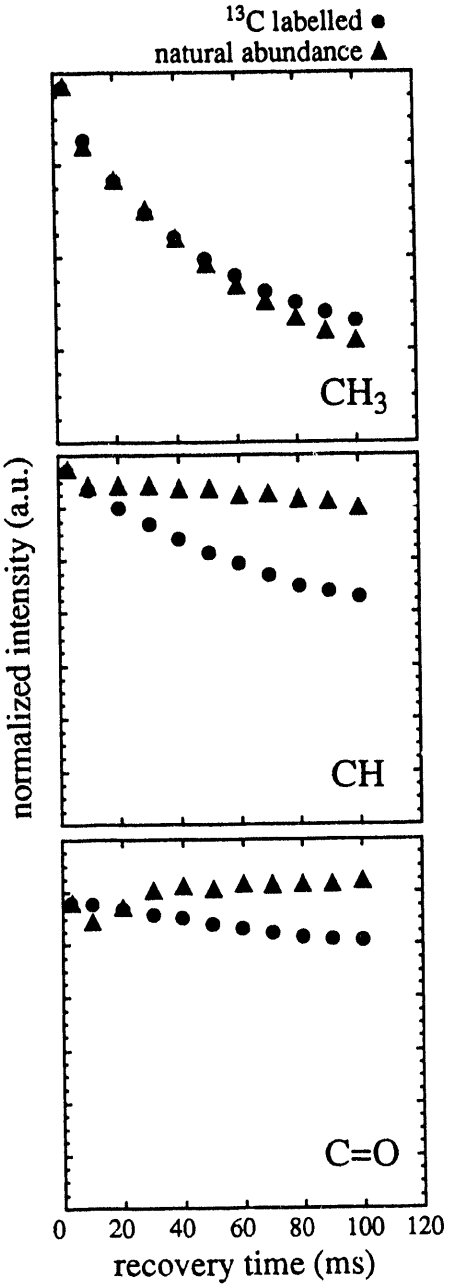

Fig. 4.2.4: A comparison of the decay of longitudinal carbon-13 magnetization in natural abundance and triply ^{13}C enriched L-alanine. The data represent the integrals of peaks recorded for various values of the recovery time in a ^{13}C CP-MAS inversion recovery experiment with high power proton decoupling during the recovery time. The experimental conditions were the same as those for the spectra used in Figs. 2 and 3. As we expect, if cross relaxation between carbons occurs, the long CH and C=O relaxation times are shortened in the enriched compound, whilst the CH_3 relaxation time is slightly lengthened. This is a reflection of the fact that all three carbons are more efficiently coupled together in the enriched compound due to the addition of the homonuclear relaxation pathway.

expected cross relaxation in the enriched compound causes the long CH and C=O relaxation times to shorten, whilst the short CH_3 relaxation time is slightly lengthened. This result serves to confirm that there is indeed an extra mechanism which couples the carbon atoms in the enriched solid. Finally, in order to confirm that this effect is not special to L-alanine (even though we shall see that the mechanisms proposed below are very general in nature) we have also recorded a series of cross relaxation spectra for doubly labeled $^{13}C_{1,2}$ zinc acetate (not shown) and there we again observe polarization transfer between the two carbon sites. The initial rate we observe in this case being 120 $(ms)^{-1}$.

Section 4.3: Theoretical Models for the Relaxation Behavior

We are aware of two reasonable models that can explain magnetization exchange between the carbons, both of which are induced by rapid molecular motion. In the case where cross relaxation between the carbon atoms is caused by motion of the carbon framework, a conventional second order perturbation treatment is appropriate. In the presence of proton decoupling and assuming that the carbon framework itself is rigid, a third order treatment of cross relaxation is necessary to provide a mechanism for cross relaxation. In this model the fluctuations in dipolar couplings to nearby protons provide the missing energy required for the carbon nuclei to communicate. There are also some familiar mechanisms for magnetization exchange in solid state NMR that are unreasonable mechanisms in this experiment. The first is a failure of decoupling leading to spin diffusion, and the second is rotational resonance.

Section 4.3.1: Unreasonable Mechanisms for Magnetization Transfer

Before continuing with a treatment of cross relaxation, we should outline why we can discount more common mechanisms for cross relaxation. The most obvious choice

would be proton driven spin diffusion.[8,9] Even though high power proton decoupling is applied together with magic angle spinning to remove both heteronuclear and homonuclear dipolar couplings, homonuclear couplings in a three spin system are not completely refocused, and rapid molecular motion can interfere with rf decoupling. That removal of the dipolar couplings is slightly less effective in fully ^{13}C enriched alanine is evidenced by the slightly larger linewidths (we observe ≈150 Hz as opposed to ≈70 Hz). However, the three resonances in the MAS spectra of enriched alanine and the two resonances in zinc acetate are all fully resolved. There is negligible overlap between the lines which immediately tells us that spin diffusion, whether direct carbon or proton driven, will be completely quenched to first order. Even if this simple criteria were not sufficient, we would (i) expect to see a dependence on decoupling power which is not verified by experiment, (ii) we also expect to see a dependence of the buildup rates on the difference in chemical shifts between the carbons, which is not borne out in the alanine spectra.

The second well known mechanism for polarization transfer is rotational resonance.[14]We can discount rotational resonance because we have carefully adjusted the spinning speeds used in our experiments to avoid rotational resonance. As we mentioned above, rotational resonance is a particularly selective technique, and is usually only effective if the resonance condition is set to within the dipolar linewidth. In the experiments shown below we are always at least 1.2 kHz away from rotational resonance. Additionally we do not see any (significant) dependence of the relaxation rates on spinning speed.

We postulate that the actual mechanism of polarization transfer is true cross relaxation between the carbon nuclear spins and that there are two distinct contributions. The first is caused by the dynamic mixing of the ^{13}C energy levels by the carbon proton dipole-dipole interaction and the second is driven by the local field generated by the motion of nearby protons. *This latter is a true three body effect.* The usual treatment of dipolar relaxation uses second order perturbation theory to model what is normally a two body problem.[1,20-22]

Section 4.3.2: Second Order Treatment of Relaxation

In section 1.10 of this thesis, we presented a second order expansion of the Liouville-von Neumann equation in order to describe the relaxation of an ensemble of spins to equilibrium. The master equation for the relaxation of an operator, Q, was shown in that section to be

$$\frac{\partial <Q>}{\partial t} = -\sum_{m}\sum_{r,r'} \delta_{\omega^{r}_{l,m},-\omega^{r'}_{l,-m}} J_m\left(\omega^{r'}_{l,-m}\right) Tr\left\{\left[A^{r}_{l,m},\left[A^{r'}_{l,-m},Q\right]\right]\left(\rho^{*}(t)-\rho^{*}_{eq}(t)\right)\right\}, \quad \text{(eq. 4.3.2.1)}$$

where $J_m\left(\omega^{r'}_{l,-m}\right)$ is the spectral density of the motion, and $A^{r}_{l,m}$ is defined by the fourier decomposition of the time-dependent spherical tensors,

$$T^{*}_{l,m}(t) = \sum_{r} A^{r}_{l,m} e^{i\omega^{r}_{l,m}t}. \quad \text{(eq. 4.3.2.2)}$$

Calculation of the commutators in equation 4.3.2.1 is relatively straightforward and provides the well known results of Redfield theory.[20,22] Cross relaxation can occur between the two carbons. However, the corresponding spectral densities tell us that these terms will only be non zero if the dipolar coupling between the two carbons is fluctuating, i.e. if the carbon skeleton is mobile. Thus, contributions to relaxation from second order mechanisms will only arise from the small amplitude librational motions of the carbon skeleton. Not only are these motions small, but they are expected to occur at relatively high frequencies which are inefficient for relaxation. This is the reason why cross relaxation has previously been discounted as unimportant in rigid organic solids. Indeed, the crystal structure of alanine leaves little room for framework motion.[23]

Calculating the commutators and spectral densities of equation 4.3.2.1 for various random Hamiltonians, but always assuming that the C-C dipolar couplings are not varying,

shows that direct cross relaxation between the carbons is quenched. In contrast, the large amplitude motions of the protons on the methyl and amine groups yield large spectral densities but the corresponding commutators all lead to the conversion of carbon polarization into proton polarization or multi spin order of the carbon and proton spins. In the experiment of figure 4.2.1 these terms will be immediately destroyed by the decoupling field, and will thus not contribute to the observables. Also, the efficiency of such mechanisms will only be marginally affected by enrichment with labeled carbon atoms, the primary effect being due to carbon proton pairs. Given that second order perturbations do not contribute much to carbon cross relaxation, we must consider other alternatives to explain our data and the way is now open for the observation of the effect of the smaller third order contributions at longer timescales. There are several qualitative reasons why third order contributions may be large compared to second order contributions. Firstly, we shall see that they depend on the larger carbon proton dipolar couplings, as opposed to the homonuclear carbon couplings, and secondly the spectral densities are influenced mostly by the large amplitude motions of the protons which are known to occur at frequencies comparable to the Larmor frequency,[24] as opposed to the small librational motions at higher frequencies.

There is, however, another possible second order relaxation mechanism that could cause cross relaxation between ^{13}C nuclei. This effect is the dynamic mixing of the ^{13}C energy states by the time-dependent C-H dipolar coupling. The Hamiltonian for the system of two ^{13}C nuclei and one proton is

$$H = \omega_H S_Z + \omega_{C_1} I_Z^{(1)} + \omega_{C_2} I_Z^{(2)} + H_{DD}^{C_1C_2} + H_{DD}^{C_1H}(t) + H_{DD}^{C_2H}(t). \qquad \text{(eq. 4.3.2.3)}$$

To diagonalize this Hamiltonian, we must find a time dependent unitary transformation. This unitary transformation will lead to a time dependent mixing of the ^{13}C states and allow

cross relaxation between these state due to the motion of the proton. The detailed theory for this idea has not yet been determined.

Section 4.3.3: Third Order Treatment of Relaxation

A third order description of relaxation can simply be formulated by following the same framework as was used in section 1.10 for the second order treatment. The expansion of the density at time, t, to third order gives

$$\sigma(t)=\sigma(0)-i\int_0^t\left[\mathbf{H}_1^*(t'),\sigma(0)\right]dt'-\int_0^t dt'\int_0^{t'}dt''\left[\mathbf{H}_1^*(t'),\left[\mathbf{H}_1^*(t''),\sigma(0)\right]\right]$$
$$-i\int_0^t dt'\int_0^{t'}dt''\int_0^{t''}dt'''\left[\mathbf{H}_1^*(t'),\left[\mathbf{H}_1^*(t''),\left[\mathbf{H}_1^*(t'''),\sigma(0)\right]\right]\right] \qquad \text{(eq. 4.3.3.1)}$$

and now the time derivative of equation 4.3.3.1 yields

$$\frac{d\sigma}{dt}=-i\left[\mathcal{H}_1^*(t),\sigma(0)\right]-\int_0^t dt'\left[\mathcal{H}_1^*(t),\left[\mathcal{H}_1^*(t'),\sigma(0)\right]\right]-i\int_0^t dt'\int_0^{t'}dt''\left[\mathcal{H}_1^*(t),\left[\mathcal{H}_1^*(t'),\left[\mathcal{H}_1^*(t''),\sigma(0)\right]\right]\right] \qquad \text{(eq. 4.3.3.2)}$$

Introducing the variables $\tau=t-t'$ and $\tau'=t-t''$, taking the ensemble average, making the Redfield approximation, and neglecting the second order term since we assume it does not contribute to cross relaxation (although it does contain non zero elements that contribute to the overall decay of magnetization), we obtain the equation for the average density matrix

$$\frac{d\sigma}{dt}=-i\int_0^\infty d\tau\int_0^\infty d\tau'\overline{\left[\mathcal{H}_1^*(t),\left[\mathcal{H}_1^*(t-\tau_1),\left[\mathcal{H}_1^*(t-\tau_2),\sigma(t)\right]\right]\right]}. \qquad \text{(eq. 4.3.3.3)}$$

We now introduce the three-time correlation functions,

$$g_{mm'm''}^{rr'r''}(t;\tau_1,\tau_2)=C^{(r)}C^{(r')}C^{(r'')}\overline{R_{2,-m''}^{(r'')}(t)R_{2,-m'}^{(r')}(t-\tau_1)R_{2,-m}^{(r)}(t-\tau_2)}. \qquad \text{(eq. 4.3.3.4)}$$

Replacing $\mathscr{H}_1^*$ in equation 4.3.3.3, we obtain

$$\frac{d\sigma}{dt} = -i \sum_{\substack{r,r',r'' \\ m,m',m'' \\ p,p',p''}} exp\left\{i\left(\omega_{m,p}^{(r)} + \omega_{m',p'}^{(r')} + \omega_{m'',p''}^{(r'')}\right)t\right\}\left[A_{m'',p''}^{(r'')}, \left[A_{m',p'}^{(r')}, \left[A_{m,p}^{(r)}, \sigma(t)\right]\right]\right]$$

$$\times \int_0^{\infty}\int_0^{\infty} g_{mm'm''}^{rr'r''}(\tau_1, \tau_2) exp\left\{-i\left(\omega_{m,p}^{(r)}\tau_2 + \omega_{m',p'}^{(r')}\tau_1\right)\right\} d\tau_1 d\tau_2 \qquad \text{(eq. 4.3.3.5)}$$

Keeping only secular terms, $\omega_{m,p}^{(r)} + \omega_{m',p'}^{(r')} + \omega_{m'',p''}^{(r'')} \approx 0$, then yields

$$\frac{d\sigma}{dt} = -i \sum_{\substack{r,r',r'' \\ m,m',m'';m+m'+m''=0 \\ p,p',p''}} \left[A_{m'',p''}^{(r'')}, \left[A_{m',p'}^{(r')}, \left[A_{m,p}^{(r)}, \sigma(t)\right]\right]\right] \times \int_0^{\infty}\int_0^{\infty} g_{mm'm''}^{rr'r''}(\tau_1, \tau_2) exp\left\{-i\left(\omega_{m,p}^{(r)}\tau_2 + \omega_{m',p'}^{(r')}\tau_1\right)\right\} d\tau_1 d\tau_2$$

(eq. 4.3.3.6)

Note that, in contrast to the second order case where the secular approximation led to a reduction in the number of indices over which the sum is carried out, this is a lesser restriction in the third order case, as we still have three indices. The restriction introduced by the secular approximation being only that they sum to zero. Using the relation

$$\int_0^{\infty}\int_0^{\infty} g_{mm'm''}^{rr'r''}(\tau_1, \tau_2) exp\left\{-i\left(\omega_{m,p}^{(r)}\tau_1 + \omega_{m',p'}^{(r')}\tau_2\right)\right\} d\tau_1 d\tau_2 = \int_0^{\infty}\int_0^{\infty} g_{mm'm''}^{rr'r''}(\tau_1, \tau_2) cos\left(\omega_{m,p}^{(r)}\tau_1 + \omega_{m',p'}^{(r')}\tau_2\right) d\tau_1 d\tau_2$$

$$-i\int_0^{\infty}\int_0^{\infty} g_{mm'm''}^{rr'r''}(\tau_1, \tau_2) sin\left(\omega_{m,p}^{(r)}\tau_1 + \omega_{m',p'}^{(r')}\tau_2\right) d\tau_1 d\tau_2 ,$$

and given that $g_{mm'm''}^{rr'r''}$ can be shown to be a real function we obtain

$$\int_0^{\infty}\int_0^{\infty} g_{mm'm''}^{rr'r''}(\tau_1, \tau_2) exp\left\{-i\left(\omega_{m,p}^{(r)}\tau_1 + \omega_{m',p'}^{(r')}\tau_2\right)\right\} d\tau_1 d\tau_2 = J_{mm'm''}^{rr'r''}\left(\omega_{m,p}^{(r)}, \omega_{m',p'}^{(r')}\right) - ik_{mm'm''}^{rr'r''}\left(\omega_{m,p}^{(r)}, \omega_{m',p'}^{(r')}\right)$$

(eq. 4.3.3.8)

where $J^{rr'r''}_{mm'm''}$ and $k^{rr'r''}_{mm'm''}$ are real numbers defined by equation 4.3.3.7. In this case the real part of this expression is the third order dynamic shift, which can be included in a redefined unperturbed Hamiltonian, while the imaginary part contributes to relaxation. The master equation at third order is thus

$$\frac{d\sigma}{dt} = -\sum_{\substack{m,m',m'';m+m'+m''=0 \\ p,p',p'' \\ r,r',r''}} k^{rr'r''}_{mm'm''}\left(\omega^{(r)}_{m,p},\omega^{(r')}_{m',p'}\right)\left[A^{(r'')}_{m'',p''},\left[A^{(r')}_{m',p'},\left[A^{(r)}_{m,p},\sigma(t)\right]\right]\right]. \qquad \text{(eq. 4.3.3.9)}$$

The equation of motion for the expectation value of an observable operator Q is given by

$$\frac{d\langle Q\rangle}{dt} = -\sum_{\substack{m,m',m'';m+m'+m''=0 \\ p,p',p'' \\ r,r',r''}} k^{rr'r''}_{mm'm''}\left(\omega^{(r)}_{m,p},\omega^{(r')}_{m',p'}\right) Tr\left\{\left[A^{(r'')}_{m'',p''},\left[A^{(r')}_{m',p'},\left[A^{(r)}_{m,p},\sigma(t)\right]\right]\right]Q\right\}. \qquad \text{(eq. 4.3.3.10)}$$

which, through repeated use of the relation $Tr\{A[B,C]\} = Tr\{[A,B]C\}$, can be rewritten as

$$\frac{d\langle Q\rangle}{dt} = -\sum_{\substack{m,m',m'';m+m'+m''=0 \\ p,p',p'' \\ r,r',r''}} k^{rr'r''}_{mm'm''}\left(\omega^{(r)}_{m,p},\omega^{(r')}_{m',p'}\right) Tr\left\{\left[A^{(r)}_{m,p},\left[A^{(r')}_{m',p'},\left[A^{(r'')}_{m'',p''},Q\right]\right]\right]\sigma(t)\right\}. \qquad \text{(eq. 4.3.3.11)}$$

We are now in a position to use equation 4.3.3.11 to predict the behavior of our system at third order. The simplest spin system that serves to demonstrate homonuclear carbon cross relaxation is that of two carbon atoms and one proton. The unperturbed Hamiltonian is

$$\mathcal{H}_0 = \omega_S S_z + \omega_{I_1} I_{1z} + \omega_{I_2} I_{2z} \qquad \text{(eq. 4.3.3.12)}$$

and the random perturbation is

$$\mathcal{H}_1 = \omega_{C_1H}\sum_m R^{C_1H}_{2,-m}(t)T^{C_1H}_{2,m} + \omega_{C_2H}\sum_n R^{C_2H}_{2,-n}(t)T^{C_2H}_{2,n} + \omega_{C_1C_2}\sum_l R^{C_1C_2}_{2,-l}(t)T^{C_1C_2}_{2,l}.$$

(eq. 4.3.3.13)

In our first example we neglect the (time independent) homonuclear carbon carbon dipolar coupling. It may either be assumed to be zero, or it may be included in a redefined unperturbed Hamiltonian. For simplicity we assume it is zero. We have

$$T^{C_1H}_{2,0} = \tfrac{1}{2\sqrt{6}}(4I_{1z}S_z - I_{1+}S_- - I_{1-}S_+), \qquad T^{C_1H}_{2,\pm1} = \tfrac{1}{\sqrt{2}}(4I_{1\pm}S_z + I_{1z}S_\pm), \quad T^{C_1H}_{2,\pm2} = I_{1\pm}S_\pm,$$

(eq. 4.3.3.14)

for $r = C_1H$ with similar expressions for $r = C_2H$. Transforming into the interaction representation, we obtain, for $r = C_1H$

$$T^{C_1H}_{2,0}(t) = \tfrac{1}{2\sqrt{6}}\left(4I_{1z}S_z - I_{1+}S_- \exp\left\{i\left(\omega_{I_1} - \omega_S\right)t\right\} - I_{1-}S_+ \exp\left\{i\left(\omega_S - \omega_{I_1}\right)t\right\}\right),$$

$$T^{C_1H}_{2,\pm1}(t) = \tfrac{1}{\sqrt{2}}\left(4I_{1\pm}S_z \exp\left\{\pm i\omega_{I_1}t\right\} + I_{1z}S_\pm \exp\left\{\pm i\omega_S t\right\}\right),$$

$$T^{C_1H}_{2,\pm2} = I_{1\pm}S_\pm \exp\left\{\pm i\left(\omega_S + \omega_{I_1}\right)t\right\}. \qquad \text{(eq. 4.3.3.15)}$$

The $T^{(r)}_{2,m}(t)$ are then decomposed into $A^{(r)}_{m,p}$ and $\omega^{(r)}_{m,p}$ for $r = C_1H$,

$$A^{C_1H}_{0,0} = \tfrac{2}{\sqrt{6}}I_{1z}S_z, \qquad A^{C_1H}_{0,1} = -\tfrac{1}{2\sqrt{6}}I_{1+}S_-, \qquad A^{C_1H}_{0,2} = -\tfrac{1}{2\sqrt{6}}I_{1-}S_+,$$

$$\omega^{C_1H}_{0,0} = 0, \qquad \omega^{C_1H}_{0,1} = \omega_{I_1} - \omega_S, \qquad \omega^{C_1H}_{0,2} = \omega_S - \omega_I,$$

$$A^{C_1H}_{\pm1,0} = \tfrac{1}{\sqrt{2}}I_{1\pm}S_z, \qquad A^{C_1H}_{\pm1,1} = \tfrac{1}{\sqrt{2}}I_{1z}S_\pm, \qquad A^{C_1H}_{\pm2,0} = I_\pm S_\pm,$$

$$\omega_{\pm 1,0}^{C_1H} = \pm\omega_{I_1}, \qquad \omega_{\pm 1,1}^{C_1H} = \pm\omega_S, \qquad \omega_{\pm 2,0}^{C_1H} = \pm\left(\omega_S + \omega_{I_1}\right),$$

(eq. 4.3.3.16)

with similar expressions for $r = C_2H$. Calculation of the commutators of equation 4.3.3.11 for the secular terms is now straightforward, though tedious. As an example of a representative term we find

$$\left[A_{-1,0}^{C_1H}, \left[A_{+1,1}^{C_2H}, \left[A_{0,1}^{C_1H}, I_{1z}\right]\right]\right] = \frac{1}{4\sqrt{6}} I_{1z} I_{2z}. \qquad \text{(eq. 4.3.3.17)}$$

In total there are twelve terms which are involved in the conversion $I_{1z} \rightarrow I_{1z} I_{2z}$ depending

$\left[A_{m,p}^{(r)}, \left[A_{m',p'}^{(r')}, \left[A_{m'',p''}^{(r'')}, Q\right]\right]\right]$	$k_{mm'm''}^{rr'r''}\left(\omega_{m,p}^{(r)}, \omega_{m',p'}^{(r')}\right)$
$\left[A_{0,2}^{C_1H}, \left[A_{0,0}^{C_2H}, \left[A_{0,1}^{C_1H}, I_{1z}\right]\right]\right] = \frac{1}{12\sqrt{6}}\left(I_{2z}S_z - I_{1z}I_{2z}\right)$	$k_{0,0,0}^{C_1H,C_2H,C_1H}\left(\omega_S - \omega_{I_1}, 0\right)$
$\left[A_{0,1}^{C_1H}, \left[A_{0,0}^{C_2H}, \left[A_{0,2}^{C_1H}, I_{1z}\right]\right]\right] = -\frac{1}{12\sqrt{6}}\left(I_{2z}S_z - I_{1z}I_{2z}\right)$	$k_{0,0,0}^{C_1H,C_2H,C_1H}\left(\omega_{I_1} - \omega_S, 0\right)$
$\left[A_{0,1}^{C_1H}, \left[A_{+1,1}^{C_2H}, \left[A_{-1,0}^{C_1H}, I_{1z}\right]\right]\right] = -\frac{1}{4\sqrt{6}}\left(I_{2z}S_z - I_{1z}I_{2z}\right)$	$k_{0,+1,-1}^{C_1H,C_2H,C_1H}\left(\omega_{I_1} - \omega_S, \omega_S\right)$
$\left[A_{0,2}^{C_1H}, \left[A_{-1,1}^{C_2H}, \left[A_{+1,0}^{C_1H}, I_{1z}\right]\right]\right] = \frac{1}{4\sqrt{6}}\left(I_{2z}S_z - I_{1z}I_{2z}\right)$	$k_{0,-1,+1}^{C_1H,C_2H,C_1H}\left(\omega_S - \omega_{I_1}, -\omega_S\right)$
$\left[A_{+1,0}^{C_1H}, \left[A_{-1,1}^{C_2H}, \left[A_{0,2}^{C_1H}, I_{1z}\right]\right]\right] = -\frac{1}{4\sqrt{6}} I_{1z}I_{2z}$	$k_{+1,-1,0}^{C_1H,C_2H,C_1H}\left(\omega_{I_1}, -\omega_S\right)$
$\left[A_{-1,0}^{C_1H}, \left[A_{+1,1}^{C_2H}, \left[A_{0,1}^{C_1H}, I_{1z}\right]\right]\right] = -\frac{1}{4\sqrt{6}} I_{1z}I_{2z}$	$k_{-1,+1,0}^{C_1H,C_2H,C_1H}\left(-\omega_{I_1}, \omega_S\right)$
$\left[A_{0,2}^{C_1H}, \left[A_{-1,1}^{C_2H}, \left[A_{-1,0}^{C_1H}, I_{1z}\right]\right]\right] = \frac{1}{2}\left(I_{2z}S_z + I_{1z}I_{2z}\right)$	$k_{+2,-1,-1}^{C_1H,C_2H,C_1H}\left(\omega_S + \omega_{I_1}, -\omega_S\right)$
$\left[A_{-2,0}^{C_1H}, \left[A_{+1,1}^{C_2H}, \left[A_{+1,0}^{C_1H}, I_{1z}\right]\right]\right] = -\frac{1}{2}\left(I_{2z}S_z + I_{1z}I_{2z}\right)$	$k_{-2,+1,+1}^{C_1H,C_2H,C_1H}\left(-\omega_S - \omega_{I_1}, -\omega_S\right)$
$\left[A_{-1,0}^{C_1H}, \left[A_{-1,1}^{C_2H}, \left[A_{2,0}^{C_1H}, I_{1z}\right]\right]\right] = -\frac{1}{2} I_{1z}I_{2z}$	$k_{-1,-1,+2}^{C_1H,C_2H,C_1H}\left(-\omega_{I_1}, -\omega_S\right)$
$\left[A_{+1,0}^{C_1H}, \left[A_{+1,1}^{C_2H}, \left[A_{-2,0}^{C_1H}, I_{1z}\right]\right]\right] = \frac{1}{2} I_{1z}I_{2z}$	$k_{+1,+1,-2}^{C_1H,C_2H,C_1H}\left(\omega_{I_1}, \omega_S\right)$
$\left[A_{+2,0}^{C_1H}, \left[A_{0,0}^{C_2H}, \left[A_{-2,0}^{C_1H}, I_{1z}\right]\right]\right] = -\frac{2}{\sqrt{6}}\left(I_{2z}S_z + I_{1z}I_{2z}\right)$	$k_{+2,0,-2}^{C_1H,C_2H,C_1H}\left(\omega_S + \omega_{I_1}, 0\right)$
$\left[A_{-2,0}^{C_1H}, \left[A_{0,0}^{C_2H}, \left[A_{+2,0}^{C_1H}, I_{1z}\right]\right]\right] = \frac{2}{\sqrt{6}}\left(I_{2z}S_z + I_{1z}I_{2z}\right)$	$k_{-2,0,+2}^{C_1H,C_2H,C_1H}\left(-\omega_S - \omega_{I_1}, 0\right)$

Table 4.3.3.1: Commutators and spectral densities from Eq. (32) involved in the conversion $I_{1z} \rightarrow I_{1z} I_{2z}$.

on twelve corresponding spectral densities, and they are listed in Table 4.3.3.1. The important thing to realize is that the fluctuations of the proton carbon dipolar couplings can convert single spin order of one carbon into two spin (dipolar) order of the two carbons with a rate proportional to the sum of spectral densities and prefactors given in Table 4.3.3.1 There are a similar set of commutators which convert two spin order into polarization of the second carbon, thereby achieving polarization transfer between the carbons. If we include a non-zero carbon carbon dipolar coupling in the perturbing dipolar Hamiltonian, there are even more terms which allow this conversion, *even if the CC coupling is not fluctuating*. Note that all these mechanisms are, in the language of normal Redfield theory, cross correlation terms as the spectral densities represent correlations between (up to three) different dipolar couplings.[22] Note also that we do not find terms which simply cause direct cross relaxation between carbon polarizations.

Section 4.4: Discussion

Homonuclear cross relaxation spectroscopy of ^{13}C as outlined in this article seems to present a attractive method for broadband correlation of dipolar couplings in solids spinning at the magic angle. The experimental considerations of the experiment are especially simple, as correlations are achieved without the need for matching any special condition or for the application of pulses during the mixing period. At first sight the results we present here may seem surprising. It appears that cross relaxation between carbon atoms in "rigid" organic solids has previously been discounted as likely to occur only on a timescale of tens of seconds, although cross relaxation has been observed between mobile carbons. To our knowledge this work provides the first direct observation of carbon-carbon cross relaxation in a rigid solid, and moreover we have shown that it is efficient on a timescale of tens of milliseconds.

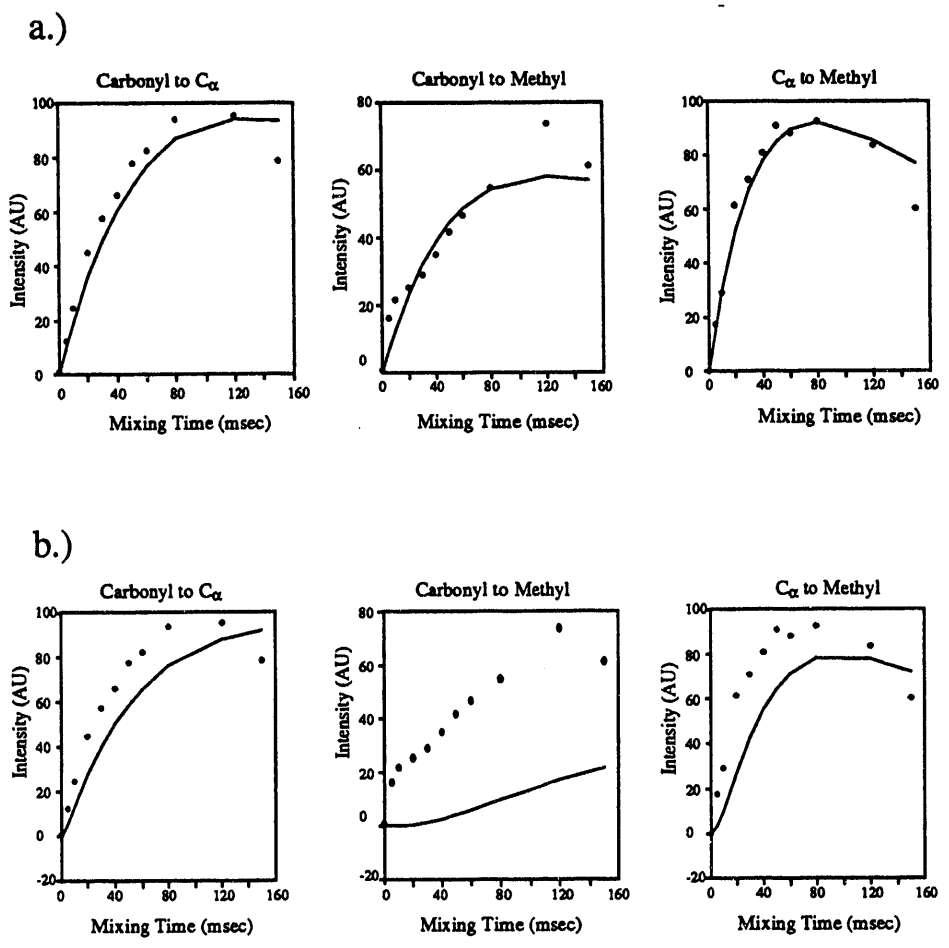

Fig. 4.4.1: Fits of cross relaxation data to the full rate matrix. a.) Fits to a direct cross relaxation mechanism. b.) Fits to an indirect cross relaxation mechanism where the intermediate is assumed to be two spin order between the cross relaxing spins.

To determine which mechanism is reasonable for the observed cross relaxation, we performed full rate matrix calculations[19,25,26] of the three spin system for both a direct and indirect cross relaxation. The indirect cross relaxation is assumed to involve an intermediate two spin order state. Figure 4.4.1 shows the fitted cross peak growth curves for both mechanisms. Clearly the direct cross relaxation mechanism fits the data much better than the mechanism involving the two spin order intermediate, implying that the cross relaxation is due primarily to the dynamic mixing of the carbon states. The rates determined in this fitting procedure are presented in table 4.4.1. While the proposed third

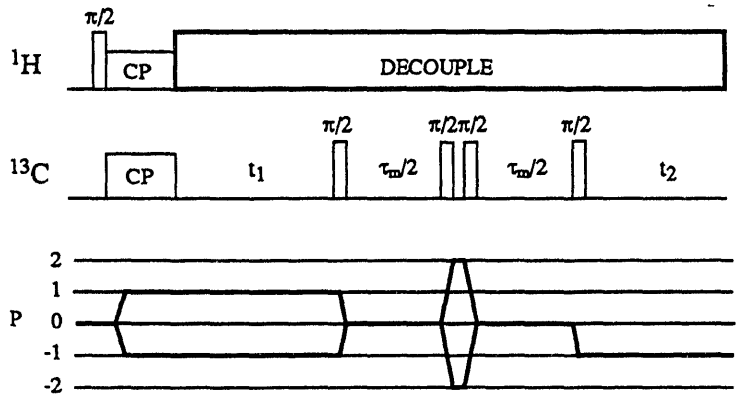

Fig. 4.4.2: Double quantum filtered exchange experiment used to test for the presence of two spin order during the mixing period.

order mechanism is not the predominate effect leading to cross relaxation, we have observed the predicted two spin order (data not shown) by performing the double quantum filtered experiment shown in figure 4.4.2. Further experiments are planned to determine whether we are truly observing this third order effect. One should also note that although the examples of zinc acetate and L-alanine presented here are clearly model examples, nevertheless there is nothing obviously special about these materials and we expect the effects to be observed in all organic solids of this type, with a most obvious application being to the spectra of polypeptides.

The results and analysis we present here are only preliminary, we are currently investigating the temperature dependencies of the cross relaxation to determine the source of the cross relaxation. We hope to be able to quantitate the effect in order to determine internuclear distances in powdered organic solids. However, even if the goal of absolute quantitation turns out to be difficult to achieve, these experiments will surely provide a useful means of sequentially assigning complex solid state spectra and determining qualitative distances. Such data should be capable of providing the solid state structure of larger molecules, in a manner analogous to liquid state structure determination using NOESY data.

Bibliography

Chapter 1

(1) J. J. Sakurai, *Modern Quantum Mechanics*, Addison-Wesley Publishing Company, Inc, Redwood City, California, 1985.

(2) Tolman, , .

(3) C. P. Slichter, *Principles of Magnetic Resonance,* Third ed., Springer-Verlag, Berlin, 1990, Vol. 1.

(4) U. Fano, Reviews of Modern Physics **29**, 74-93 (1957).

(5) R. R. Ernst, G. Bodenhausen and A. Wokaun, *Principles of Nuclear Magnetic Resonance in One and Two Dimensions*, Clarendon Press, Oxford, 1990, Vol. 14.

(6) U. Fano, Phys. Rev. **90**, 577-579 (1953).

(7) A. Abragam, *Principles of Nuclear Magnetism*, Clarendon Press, Oxford, 1989, Vol. 32.

(8) U. Haeberlen and J. S. Waugh, Phys. Rev. **175**, 453 (1968).

(9) J. S. Waugh, L. M. Huber and U. Haeberlen, Phys. Rev. Lett. **20**, 180- (1968).

(10) M. E. Rose, *Elementary Theory of Angular Momentum*, Wiley, New York, N.Y., 1955.

(11) A. R. Edmonds, *Angular Momentum in Quantum Mechanics,* Second ed., Princeton University Press, Princeton, N.J., 1974, Vol. 4.

(12) M. Mehring, *Principles of High Resolution NMR in Solids*, Springer-Verlag, 1976.

(13) E. Butkov, *Mathematical Physics*, Addison-Wesley Publishing Co., Reading Mass., 1968.

(14) V. Heine, *Group Theory in Quantum Mechanics*, 1977.

(15) B. F. Chmelka, K. T. Mueller, A. Pines, J. Stebbins, Y. Wu and J. W. Zwanziger, Nature **339**, 42 (1989).

(16) A. Llor and J. Virlet, Chem. Phys. Lett. **152**, 248 (1988).

(17) A. Samoson, E. Lippmaa and A. Pines, Mol. Phys. **65**, 1013 (1988).

(18) E. Kundla, A. Samoson and E. Lippmaa, Chem. Phys. Lett. **83**, 229 (1981).

(19) M. Goldman, P. J. Grandinetti, A. Llor, Z. Oleniczak, J. R. Sachleben and J. W. Zwanziger, J. Chem. Phys. **97**, 8947-8960 (1992).

(20) V. Vleck, Phys. Rev. **33**, 467 (1929).

(21) M. M. Maricq, Adv. Magn. Reson. **14**, 151 (1990).

(22) J. Jeener, H. Eisendrath and R. V. Steenwinkel, Phys. Rev. **133 A**, 478 (1964).

(23) M. Goldman, *Spin Temperature and Nuclear Magnetic Resonance in Solids*, Oxford University Press, London, 1970.

(24) M. M. Maricq and J. S. Waugh, J. Chem. Phys. **70**, 3300 (1979).

(25) J. H. Shirley, Phys. Rev. **138**, 979 (1965).

(26) M. M. Maricq, Phys. Rev. B **25**, 6622 (1982).

(27) U. Haeberlen, *High Resolution NMR in Solids*, Academic Press, 1976.

(28) R. P. Feynman, F. L. Vernon and R. W. Hellwarth, J. Appl. PHys. **28**, 49 (1957).

(29) M. Mehring, E. K. Wolff and M. E. Stoll, J. Magn. Reson. **37**, 475 (1980).

(30) M. Munowitz, A. Pines and M. Mehring, J. Chem. Phys. **86**, 3172 (1987).

(31) S. Vega and A. Pines, J. Chem. Phys. **66**, 5624 (1977).

(32) S. Vega, J. Chem. Phys. **68**, 5518 (1978).

(33) N. Bloembergen, E. M. Purcell and R. V. Pound, Phys. Rev. **73**, 679-712 (1948).

(34) N. Bloembergen In *Nuclear Magnetic Relaxation*, N. Bloembergen, Ed., W. A. Benjamin, Inc., New York, 1961.

(35) R. Kubo and K. Tomita, Journal of the Physical Society of Japan **9**, 888-919 (1954).

(36) R. Kubo, Journal of the Physical Society of Japan **9**, 935-944 (1954).

(37) A. G. Redfield, Phys. Rev. **98**, 1787-1809 (1955).

(38) A. G. Redfield, IBM Journal of Research and Development **1**, 19-31 (1957).

Chapter 2

(1) V. L. Colvin, A. P. Alivisatos and J. G. Tobin, Phys. Rev. Let. **66**, 2786 (1991).

(2) J. J. Shiang, A. N. Goldstein and A. P. Alivisatos, J. Chem. Phys. **92**, 3232 (1990).

(3) S. Shimitt-Rink, D. A. B. Miller and D. S. Chemla, Phys. Rev. B **35**, 8113 (1987).

(4) D. A. B. Miller, D. S. Chemla and S. Shimitt-Rink, Phys. Rev. B. **33**, 6976 (1986).

(5) M. L. Steigerwald, A. P. Alivisatos, J. M. Gibson, T. D. Harris, R. Kortan, A. M. Thayer, T. M. Duncan, D. C. Douglass and L. E. Brus, J. Am. Chem. Soc. **110**, 3046 (1988).

(6) M. Steigerwald,

(7) D. Craig, I. Dance and R. Barbutt, Angew. Chem. Int. Ed. Engl. **25**, 165 (1986).

(8) W. P. Aue, E. Bartholdi and R. R. J. Ernst, Chem. Phys. **64**, 2229 (1976).

(9) J. Jeener In *Ampere International Summer School*; Basko Polje, Yugoslavia, 1971; pp .

(10) P. E. Lippens and M. Lannoo, Phys. Rev. B **39**, 10935 (1989).

(11) L. Emsley, J. Kowalewski and G. Bodenhausen, Applied Magnetic Resonance **1**, 139-147 (1990).

(12) R. Vold and R. Vold, Prog. NMR Spectrosc. **12**, 79-133 (1978).

(13) C. P. Slichter, *Principles of Magnetic Resonance,* Third ed., Springer-Verlag, Berlin, 1990, Vol. 1.

(14) R. R. Ernst, G. Bodenhausen and A. Wokaun, *Principles of Nuclear Magnetic Resonance in One and Two Dimensions*, Clarendon Press, Oxford, 1990, Vol. 14.

(15) A. Abragam, *Principles of Nuclear Magnetism*, Clarendon Press, Oxford, 1989, Vol. 32.

(16) L. Emsley and G. Bodenhausen, J. Magn. Res. **82**, 211-221 (1989).

(17) L. Emsley and G. Bodenhausen, Chem. Phys. Lett. **165**, 469-476 (1990).

(18) D. A. Vidusek, M. F. Roberts and G. Bodenhausen, J. Am. Chem. Soc. **104**, 5452 (1982).

(19) M. F. Roberts, D. A. Vidusek and G. Bodenhausen, FEBS Lett. **117**, 311 (1980).

(20) A. J. Redfield, Chem. Phys. Lett. **96**, 537 (1983).

(21) G. A. Morris and R. Freeman, J. Am. Chem. Soc. **101**, 760 (1979).

(22) D. P. Burum and R. R. Ernst, J. Mag. Reson. **39**, 163 (1980).

(23) G. Bodenhausen and D. J. Ruben, Chem. Phys. Lett. **69**, 185 (1980).

(24) R. J. Wittebort and A. Szabo, J. Chem. Phys. **69**, 1722-1736 (1978).

(25) N. Herron, J. C. Calabrese, W. E. Farneth and Y. Wang, Science **259**, 1426-28 (1993).

(26) A. P. Alivisatos, A. Harris, N. Levinos, M. L. Steigerwald and L. E. Brus, J. Chem. Phys. **89**, 4001 (1989).

(27) M. G. Bawendi, W. L. Wilson, L. Rothberg, P. J. Carrol, T. M. Jedju, M. L. Steigerwald and L. E. Brus, Phys. Rev. Let. **65**, 1623 (1990).

(28) M. G. Bawendi, P. J. Carrol, W. L. Wilson and L. E. Brus, J. Chem. Phys. **96**, 946 (1992).

(29) P. Peyghambarian, B. Fluefel, D. Hulin, A. migus, M. Joffre, A. Antonetti, S. W. Koch and M. Lindberg, J. Quant. Electron. **25**, 2516 (1989).

Chapter 3

(1) M. Karplus, J. Chem. Physics **30**, 11-15 (1959).

(2) C. Griesinger, O. W. Sørensen and R. R. Ernst, J. Am. Chem. Soc. **107**, 6394-6396 (1985).

(3) H. Oschkinat, A. Patore, P. Pfandler and G. Bodenhausen, J. Magn. Res. **69**, 559-566 (1986).

(4) L. Emsley, T. J. Dwyer, H. P. Spielmann and D. Wemmer, submitted to J. Am. Chem. Soc. (1993).

(5) A. Abragam, *Principles of Nuclear Magnetism*, Clarendon Press, Oxford, 1989, Vol. 32.

(6) L. Emsley, J. Kowalewski and G. Bodenhausen, Applied Magnetic Resonance **1**, 139-147 (1990).

(7) R. L. Lichter and J. D. Roberts, J. Am. Chem. Soc. **93**, 5218-5224 (1971).

(8) R. J. Wittebort and A. Szabo, J. Chem. Phys. **69**, 1722-1736 (1978).

(9) J. Mellema, J. Pieters, G. V. d. Marel, J. v. Boom, C. A. G. Haasnoot and C. Altona, Eur. J. Biochem. **143**, 285 (1984).

(10) V. F. Bystrov, Prog. NMR Spectros. **10**, 41-81 (1976).

(11) K. Wüthrich, *NMR of Proteins and Nucleic Acids*, John Wiley and Sons, New York, 1986.

Chapter 4

(1) A. Abragam, *Principles of Nuclear Magnetism*, Clarendon Press, Oxford, 1989, Vol. 32.

(2) M. Mehring, *Principles of High Resolution NMR in Solids*, Springer-Verlag, 1976.

(3) C. P. Slichter, *Principles of Magnetic Resonance*, Third ed., Springer-Verlag, Berlin, 1990, Vol. 1.

(4) E. R. Andrew, A. Bradbury and R. G. Eades, Nature **182**, 1659 (1958).

(5) D. K. Sodickson, M. H. Levitt, S. Vega and R. G. Griffin, J. Chem. Phys. **98**, 6742 (1993).

(6) R. Tycko, G. Dabbagh and P. A. Mirau, J. Magn. Reson. **85**, 265 (1989).

(7) R. Tycko, J. Magn. Reson. **75**, 193 (1987).

(8) D. Suter and R. R. Ernst, Phys. Rev. B **32**, 5608 (1985).

(9) D. Suter and R. R. Ernst, Phys. Rev. B **25**, 6038 (1982).

(10) P. Robyr, B. H. Meier and R. R. Ernst, Chem. Phys. Lett. **187**, 471 (1991).

(11) P. Robyr, B. H. Meier and R. R. Ernst, Chem. Phys. Lett. **162**, 417 (1989).

(12) D. P. Raleigh, M. H. Levitt and R. G. Griffin, Chem. Phys. Lett. **146** 71 (1988).

(13) J. H. Ok, R. G. S. Spencer, A. E. Bennet and R. G. Griffin, Chem. Phys. Lett. **197**, 389 (1992).

(14) M. H. Levitt, D. P. Raleigh, R. Creuzet and R. G. Griffin, J. Chem. Phys. **92**, 6347 (1990).

(15) M. G. Colombo, B. H. Meier and R. R. Ernst, Chem. Phys. Lett. **146**, 189 (1988).

(16) A. E. Bennett, J. H. Ok, R. G. Griffin and S. Vega, J. Chem. Phys. **96**, 8624 (1992).

(17) F. Creuzet, A. McDermott, R. Gebhard, K. vanderHoef, M. B. Spijker-Assink, J. Herzfeld, J. Lugtenberg, M. H. Levitt and R. G. Griffin, Science **251**, 783 (1991).

(18) L. K. Thompson, A. E. McDermott, J. Raap, C. M. Vandervielen and e. al, Biochemistry **31**, 7931 (1992).

(19) R. R. Ernst, G. Bodenhausen and A. Wokaun, *Principles of Nuclear Magnetic Resonance in One and Two Dimensions*, Clarendon Press, Oxford, 1990, Vol. 14.

(20) A. G. Redfield In *Advances in Magnetic Resonance*, J. Waugh, Ed., , Vol. 1.

(21) R. Vold and R. Vold, Prog. NMR Spectrosc. **12**, 79-133 (1978).

(22) L. G. Werbelow and D. M. Grant,

(23) M. S. Lehmann, T. F. Koetzle and W. C. Hamilton, J. Am. Chem. Soc. **94**, 2657 (1972).

(24) K. Beshah, E. T. Olejniczak and R. G. Griffin, J. Chem. Phys. **86**, 4730 (1987).

(25) S. Macuray and R. R. Ernst, Mol. Phys. **41**, 95 (1980).

(26) J. Jeener, B. H. Meier, P. Bachmann and R. R. Ernst, J. Chem. Phys. **71**, 4546 (1979).

DATE
FILMED
2/24/94
END